



## DIPLOMARBEIT

# Light Soaking of Thin-Film Solar Cells under Colored Light

ausgeführt am  
Atominstitut  
der Technischen Universität Wien

unter der Anleitung von  
**Ao. Univ.-Prof. Dr. Johann Summhammer**

in Kooperation mit dem  
Austrian Institute of Technology  
Energy Department, Photovoltaic Systems

unter der Betreuung von  
**Dr. Marcus Rennhofer**

durch  
**Daniel MENZ BSc.**  
Gloriettegasse 1b, 1130 Wien

October 23, 2015

---

Unterschrift (Student)

---

## Danksagung

Ich möchte mich zuallererst bei meinen Diplomarbeitbetreuern Herr Professor Summhammer und Herr Dr. Rennhofer bedanken, die die finale Phase meines Physikstudiums zu einer wissenschaftlich anspruchsvollen und zugleich angenehmen Zeit gemacht haben. Durch Ihre Unterstützung wurde es mir möglich, das im Studium theoretisch erlernte in der Praxis anzuwenden und somit mein Studium zu einem für mich sehr zufriedenstellenden Abschluss zu bringen.

Weiters möchte ich mich bei meinen Eltern bedanken, die mich im Laufe meines Studiums auf alle nur erdenklichen Arten unterstützt haben. Dies gilt ebenfalls für all meine Freunde, ohne deren moralische Unterstützung mir diese Arbeit nicht möglich gewesen wäre. An dieser Stelle möchte ich mich besonders Bei Elisabeth Renner für das Korrekturlesen der frühen Versionen meiner Diplomarbeit bedanken.

Mein Dank gilt auch all meinen Kollegen vom AIT, die es mit ihrer freundlichen und fröhlichen Art stets verstanden, mich auch in schwierigen Phasen zu motivieren. Ebenfalls möchte ich Herrn Gerhard Domnanovich für seine Unterstützung in der technischen Umsetzung meiner Experimente danken.

## Zusammenfassung

Dünnschichtsolarzellen auf der Basis von Kupfer-Indium-Gallium-Selen Absorbern (auch CIGS oder Chalkogenide genannt) stellen eine vielversprechende Alternative zu konventionellen Solarzellen dar. Effizienzen von über 21% wurden erreicht und die Kosten nähern sich der 1\$/Watt Marke. Obwohl Nachteile wie die Cadmium enthaltende Pufferschicht durch neue Materialien gelöst werden, bleibt ein großer Nachteil bestehen. CIGS Solarzellen weisen metastabiles Verhalten bei der Charakterisierung im Labor auf. Dies äußert sich in Änderungen der Leerlaufspannung, des Kurzschlussstromes, des Füllfaktors und der maximalen Leistung. Dadurch ist es schwierig, die Leistung der Solarzellen vorherzusagen, wodurch auch die Renditeberechnung von Solarkraftwerken mit CIGS Solarzellen erschwert wird. Der Ist-ERtrag kann mitunter stark von der Ertragsprognose abweichen

Obwohl bereits viel Forschung über dieses Thema angestellt wurde und einige vielversprechende Ursachen für die metastabilen Effekte ausgemacht werden konnten, ist es noch nicht gelungen die mikroskopischen Vorgänge im Material eindeutig mit den makroskopischen Veränderungen der Solarzelle in Zusammenhang zu bringen.

Diese Masterarbeit beschäftigt sich mit der Implementierung eines Messaufbaus zur Messung der metastabilen Effekte von CIGS Zellen. Dieser Messaufbau ermöglicht "Light Soaking"-Experimente unter verschiedenfarbigem Licht mit unterschiedlicher Bestrahlungsstärke.

CIGS Solarzellen unterschiedlicher Qualität mit zwei verschiedenen Pufferschichtmaterialien wurden mit der entwickelten Methode vermessen. Die Messungen unter verschiedenfarbigem Licht führen zu einem möglichen Zusammenhang zwischen den bekannten metastabilen Effekten in CIGS und den gemessenen Veränderungen der Leerlaufspannung.

## **Abstract**

Thin film solar cells based on a copper-indium-gallium-selen absorber (also called CIGS or chalcogenides) are a promising alternative to conventional solar cells. CIGS solar cells have reached efficiencies of above 21% and prices close to 1\$/Watt. Disadvantages like the cadmium containing buffer layer are about to be overcome by cadmium-free buffer layers. However, one main disadvantage remains. Metastable effects changing the solar cell's parameters like the open circuit voltage and the fill factor could not be removed and are not fully understood. These metastable effects make it very difficult to characterize CIGS solar cells and to provide reliable power rating. This leads to inaccurate investment return calculations for power generation by CIGS solar cells. Hence, a profound understanding of the metastable effects would be very beneficial. A lot of research has been done on the defects and physical effects in CIGS that could be responsible for the metastabilities and on the performance effects caused by them.

This master thesis deals with the setup of a light soaking experiment able to measure the influence of light of different colors and different irradiances on the open circuit voltage, the short circuit current, the fill factor and the maximum power of CIGS cells. Other influences like changes in the temperature and the instability of the illumination are tried to be kept as small as possible.

Several CIGS cells with various performance qualities and with two different buffer layers have been measured with this method. Their behavior under differently colored light has been compared and led to a possible explanation of how the known metastable defects in CIGS cells lead to the measured changes in the open circuit voltage.

# Contents

<b>1</b>	<b>Introduction</b>	<b>7</b>
1.1	Motivation and Relevance . . . . .	7
1.2	Photovoltaics . . . . .	8
1.2.1	Photovoltaics Potential . . . . .	8
1.2.2	Principles of Photovoltaic Power Generation . . . . .	11
1.2.3	Overview of Photovoltaic Technologies . . . . .	12
1.2.4	Characterization Methods . . . . .	17
1.3	Copper Indium Gallium Selenide (CIGS) . . . . .	19
1.3.1	Cell architecture . . . . .	20
<b>2</b>	<b>Theory</b>	<b>24</b>
2.1	Functional Description of Solar Cells . . . . .	24
2.1.1	Electrons in Semiconductors . . . . .	24
2.1.2	Junctions . . . . .	26
2.1.3	Absorption of Photons . . . . .	26
2.2	Current Voltage curves (IV curves) . . . . .	28
2.2.1	Short Circuit Current and Open Circuit Voltage . . . . .	28
2.2.2	Four-Point probes Method . . . . .	29
2.2.3	Norms for IV-curve Measurements . . . . .	30
2.3	External Quantum Efficiency (EQE) . . . . .	33
2.3.1	Concept of quantum efficiency . . . . .	33
2.3.2	Monochromator . . . . .	35
2.3.3	Calibration by a semiconductor detector . . . . .	36
2.4	Colored Light Soaking of CIGS-cells . . . . .	37
2.4.1	IV-curve Anomalies of CIGS cells . . . . .	37
2.4.2	Dependencies of metastable light soaking effects . . . . .	40
2.4.3	Light spectrum . . . . .	41
<b>3</b>	<b>Methods</b>	<b>44</b>
3.1	IV-Curve Measurements . . . . .	44
3.1.1	IV-curve Setup . . . . .	44
3.1.2	Accuracy of the Keithley Source Meter . . . . .	51
3.2	EQE Measurements . . . . .	52
3.2.1	EQE Setup . . . . .	52
3.2.2	Comparison CIGS . . . . .	54
3.3	Colored Light Soaking Measurements . . . . .	58
3.3.1	Duration and Time Intervals of the Light Soaking Experiments . . . . .	58
3.3.2	Reduced Irradiance . . . . .	59
3.3.3	Color Filters . . . . .	60
3.3.4	Uniformity . . . . .	63

3.3.5	Temporal instability . . . . .	65
3.3.6	Temperature . . . . .	66
3.3.7	Automation by Keithley script . . . . .	67
3.3.8	Data Reliability . . . . .	69
<b>4</b>	<b>Results</b>	<b>72</b>
4.1	Specimen . . . . .	72
4.2	Overview of the Light Soaking Results . . . . .	74
4.2.1	Light Soaking of CdS Buffer Layer Cells . . . . .	75
4.2.2	Light Soaking of ZnO Buffer Layer Cells . . . . .	81
4.3	Discussion . . . . .	83
4.3.1	Open Circuit Voltage of CdS <sub>32</sub> under Red Light . . . . .	83
4.3.2	Effect of Metastable Charge Carriers on Voc . . . . .	84
4.3.3	CdS buffer layer . . . . .	85
4.3.4	ZnO buffer layer . . . . .	87
4.3.5	Comparison of CdS and ZnO buffer layer . . . . .	88
4.3.6	Power Rating . . . . .	89
<b>5</b>	<b>Conclusion and Outlook</b>	<b>90</b>
5.1	Conclusion . . . . .	90
5.2	Outlook . . . . .	90
	<b>Bibliography</b>	<b>92</b>
	<b>List of Figures</b>	<b>95</b>
	<b>List of Tables</b>	<b>97</b>

# 1 Introduction

## 1.1 Motivation and Relevance

Solar cells transform photon energy into electric energy by using semiconductor diodes. They have a great potential on the energy market due to the large amount of solar energy, their already low prices, no moving parts (low maintenance cost) and their long life time (usability of 25 years).

New technologies use chalcogenides (copper indium gallium selenides, abbreviated CIGS) as semiconductive absorber material. Some advantages of chalcogenides over crystalline silicon is a direct band gap and a much higher absorption coefficient. Therefore the absorber can be designed far thinner, thus saving a lot of material costs. The main disadvantage of CIGS solar cells is the usage of rare earths (Indium, Gallium) but this is about to be overcome by new materials like kesterites (copper zinc tin selenides, abbreviated CZTS).

A disadvantage of solar cells based on chalcogenides is a metastable behavior of the electric parameters ( $V_{OC}$ ,  $I_{SC}$ ,  $P_{MPP}$ , ...) especially under illumination. Because of this it is impossible to predict the power output in a reliable way following standard power rating procedures such as IEC 61215-2:2015. In order to be able to predict the power output of such a solar cell one has to know its history of irradiance and bias and how the material reacts to both of them. A lot of effort has been put into research of this effect [1].

Research has shown, that these metastable effects are bias ( $V_{OC}$ ,  $P_{MPP}$ ,  $I_{SC}$ ) and irradiance dependent [2][3] and color dependent [4]. Measurements under colored light have been made for white, red and blue light [5]. The results vary and are not yet fully understood [4].

This work intends to contribute to this field by investigating the light soaking behavior of CIGS solar cells under different light sources (white, blue, green, yellow, red and infrared) with low irradiance (around  $100 \text{ W/m}^2$ ). Low irradiance illumination is chosen because this work is part of the SYNERCIS project with the goal to implement chalcogenide thin film cells as power supply in portable gadgets like bags. There they are mostly illuminated by low irradiance stray light. The measurements are performed under laboratory conditions in order to improve the comparability of metastable thin film solar cells under test conditions. The cells performance and alteration in the fields is not examined.

Therefore the two main goals of this thesis were

- to implement a measurement setup at the Austrian Institute of Technology that enables measuring the IV-curves of thin-film cells and their change under low irradiance light soaking of selectable colors and
- to characterize and compare several thin-film cells with this new method.

This thesis is structured as follows. Chapter 1.2 gives an overview on the current status of photovoltaics in general and chapter 1.3 gives an overview on the CIGS technology.

Chapter 2 explains the theoretical principles of the main methods used in this thesis.

The implementations of these theoretical concepts are described in Chapter 3.

The results of the measurements of this work are presented and interpreted in Chapter 4.

## 1.2 Photovoltaics

“Photovoltaics” (PV) is the name of a method of directly converting solar energy into electric power using semiconducting materials that exhibit the photovoltaic effect” [6].

The history of photovoltaics started in 1839, when Alexandre Edmond Becquerel first observed photovoltaic effect. In 1877 W.G. Adams and R.E. Day observed the photoelectric effect in solidified selenium. Solar cells were first used in larger scale for space activities, because they had a far better ratio of weight to energy produced than other energy devices (e.g. battery, fuel,..). But these solar panels were quite expensive and therefore not fit to compete with other terrestrial power suppliers like fossil-fuel power stations. It took until massive research was set into the production of silicon crystals by the electronics industry that solar cells became cheaper and interesting for power production on earth. The Energy crisis in the late 1970s helped PV put a foot in the energy market leading to an electric energy output of approximately 177 TWh/a. After 2001 the electricity production costs reached grid parity in many countries, e.g. China, Japan, California and Germany.

The efficiencies have increased from a few percent at the beginning of the 1900’ to the newest record of 25.6% (silicon HIT) and 38.8% (five-junction) for non-concentrator solar cells [7]. There are many different materials and technologies used for solar cells, like silicon in crystalline and amorphous state, GaAs in single- and multijunction cells, CdTe and CIGS in thin-film cells, organic cells amongst others. Most of them are used in both concentrated and non-concentrated light. [7]

### 1.2.1 Photovoltaics Potential

Fossil fuels have brought a great productivity increase to humanity especially since the industrial revolution. Coal, oil and gas became the spine of today’s economy by covering 81 % of the world’s primary energy supply. As can be seen in figure 1.1 in 2010 11 % of the world’s primary energy consumption were satisfied by renewables, increasing to 15 % in 2040 whereas liquids, coal and natural gas will decline from a total 83 % in 2000 to 78 % in 2040. The European Union has set the goal to further reduce the usage of fossil fuels in order to reach a reduction of green house gas emissions by 80% below 1990 levels by 2050 [8].

There is a global discussion going on about reducing the use of fossil fuels in order to decrease the recently rising CO<sub>2</sub> concentration in the earth’s atmosphere. Also fossil fuels have limited reserves and therefore will only be available for about the next 85 years as can be calculated from figure 1.2.



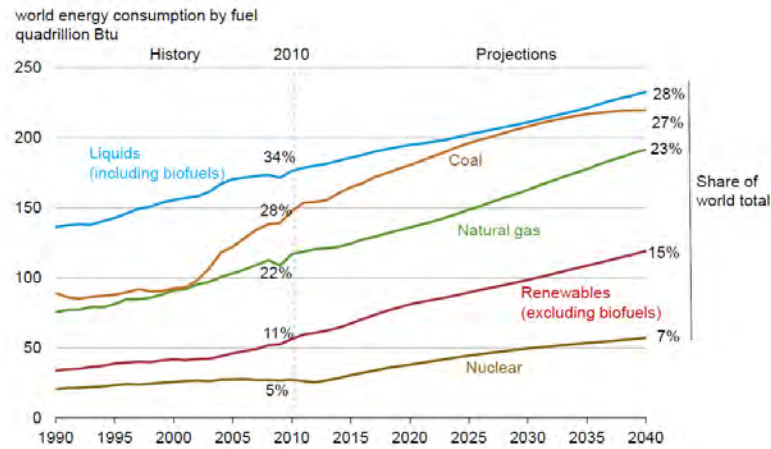


Figure 1.1: Development of world primary energy consumption since 1990 with a projection until 2040 according to “World energy consumption outlook from the International Energy Outlook, published by the U.S. DOE Energy Information Administration”

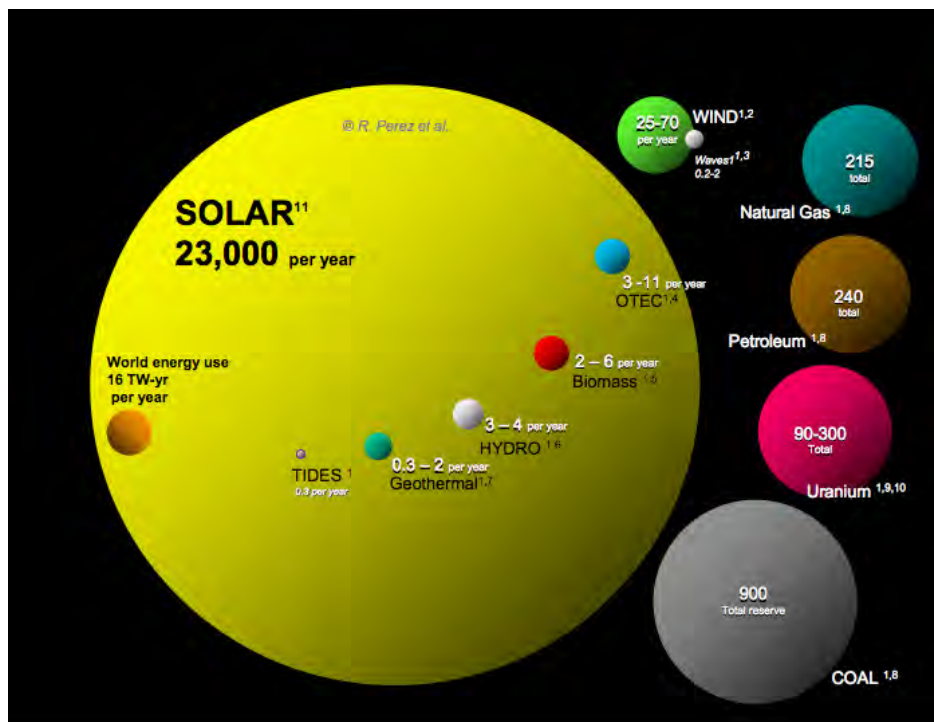


Figure 1.2: Earth's energy reserves

Nuclear energy was thought to be an alternative to fossil fuels until catastrophes like Three Mile Island in 1979 and Chernobyl in 1986 made it clear that nuclear energy is not as safe as had been assumed. Due to further, more recent accidents like the latest in Fukushima in 2011, the acceptance of nuclear power plants stayed low and their contribution to primary energy usage production is below 5% and for electrical power it was 13% in 2008 [9]. Furthermore the problem of final nuclear waste disposal hasn't been solved yet.

Using all non-renewable energy reserves (fossil and nuclear) would allow to supply humanity with energy for less than 105 years, which also makes it clear, that other energy resources have to be used.

An alternative to fossil and nuclear energy are so called renewable energies. some of the most important renewable energy resources are described in the following.

Hydropower is a widely used way to generate electric energy (2.4% of primary energy) like at Hoover Dam in the USA, Three Gorges Dam in China and Itaipu Dam in Brazil/Paraguay. Their biggest disadvantage is the large impact on the environment. In order to build the Three Gorges Dam, 1.3 million people had to be moved and lots of agriculturally used areas have been flooded. However, hydropower is the most effective way of storing electrical power. In so called pumped storage power stations, water is pumped from a lower to a higher reservoir by electrical pumps when there is more electrical power produced than needed. The stored water can then be used to produce electricity in peak hours. Like this, load variations in the power grid can be managed with efficiencies of above 80%.

Converting wind power to electrical power by wind turbines is another renewable energy source with high potential. In 2013 around 318 GW of global cumulative wind power had been installed, doubling since 2009. This upward trend also continued in 2014. 4% of the world's electrical power is generated by wind farms. The main disadvantages of wind energy are the unstable availability and the moving shade causes inconvenience in living areas. Therefore wind farms are often built in rural areas and more and more often off-shore, where also the wind availability is more stable.

The renewable energy source with the highest potential is solar energy. It can be used by thermal solar energy conversion to heat or by photovoltaic conversion to electricity. Photovoltaic conversion has the advantage, that electrical power is easier to transport and distribute. A very important value for photovoltaics is the solar constant, the solar irradiance per unit area onto the earth's atmosphere. It is roughly  $1.361 \text{ kW/m}^2$ . Although only 54.7% reach the earth's surface an area of  $23817 \text{ km}^2$  (around one fourth of Austria's total area) receives as much solar energy per year as is the world's primary energy demand. The area needed to convert as much solar energy into electrical power by photovoltaics is bigger due to summer/winter cycles, day/night cycles, cloudy atmosphere and a conversion efficiency of only around 16% of PV modules. However, the worldwide capacity of photovoltaics installed reached 177 GW in 2014, providing an average energy output of more than 200 GWh per year, presenting 1% of the world electricity demand. Different scenarios suggest that by 2050, over 20% of all electricity could be provided by photovoltaics. As can be seen in figure 1.2 the world energy demand could easily be covered by photovoltaics.

The great rise of photovoltaics over the past decades was mainly due to governmental subsidies, but in some countries (e.g. China, Germany, Spain, Japan, California,...) photovoltaic systems have reached grid parity.

The basis for all photovoltaic installations are solar cells, combined to PV modules, which can be combined to strings, resulting in high energy outputs. Therefore photovoltaic systems can be installed as small systems on houses with energy outputs of kWh but can also be easily upscaled to huge solar power plants of several 100 MW (e.g. Solar Star, Topaz Solar Farm,...).

## 1.2.2 Principles of Photovoltaic Power Generation

The basic principle of photovoltaics is the separation of charge carriers (electrons and electron holes) by incident light and subsequent collection on two different electrodes by separating them spatially via an internal electric field. After an electron-hole pair is created by incident light via the photoelectric effect, it is crucial to separate them by the internal field before they recombine. The realization of this process will be explained later in this section.

A fundamental concept for understanding photovoltaics are electron bands. As explained by quantum physics, electrons are bound to atoms in atomic orbitals at discrete energy levels. In a first approximation these energy levels depend on the number of protons in the atom's core. These energy levels are characteristic for every atom [10, 11]. When more and more atoms are brought together to form a crystal, the atomic orbitals overlap to larger and larger orbitals, providing energy levels slightly above and slightly below the original ones, thus forming so called "energy bands" [12].

Although there usually are many energy bands in a material, the most important ones are the valence band (VB) and the conductive band (CB). The valence band is the energy band with the highest energy that would be (completely) filled with electrons at a temperature of 0 K. The conductive band is the lowest energy band above the valence band (being completely empty at a temperature of 0 K). The VB and the CB can overlap (as in metals), be separated by small energies (some eV, forming so called semiconductors) or by higher energies (as in insulators). The most interesting materials for photovoltaics are semiconductors because electrons can be raised from the VB to the CB by visible light (having an energy of 1.5-3 eV and stay there long enough before recombining to be useful for photovoltaic energy collection).

The energy difference between the VB and the CB is called "band gap (energy)". Silicon for example has a band gap of 1.12 eV [13]. The band gap of silicon is a so called "indirect band gap", meaning that the reciprocal lattice vector of the VB and the CB are not the same [14]. This means that it is less likely for the material to absorb a photon than it is for materials with direct band gaps, thus needing thicker material layers in solar cells in order to absorb all of the light from the sun.

When an electron is raised into the CB by light it doesn't provide any energy usable for electricity purposes. Without further material design the excited electron will sooner or later recombine, and thereby heat the material. In order to directly get electrical power out of the device, an internal electrical field has to be introduced. In silicon solar cells, this is done by doping different parts of the material differently. While one part is doped with atoms with 5 electrons in the valence band (n-doping), the other one is doped with atoms with 3 electrons in the valence band (p-doping) (see figure 1.3 (a)). By this, the energy bands of the crystal are lowered respectively raised as can be seen in figure 1.3(b) (compare p- and n-doped region). The interface between those two regions is called "space charge region" (SCR) or (p-n-) junction. Due to the different concentration of electrons in the n- and the p-doped region, the electrons start diffusing into the p-doped region to equalize the concentration difference, thus creating an electric field, which is reducing the diffusion. An equilibrium is reached, when the diffusion force and the electric force are equal. This leads to the bent energy band structure between the n- and p-doped region.

The energy difference between the p-region and the n-region can not only be achieved

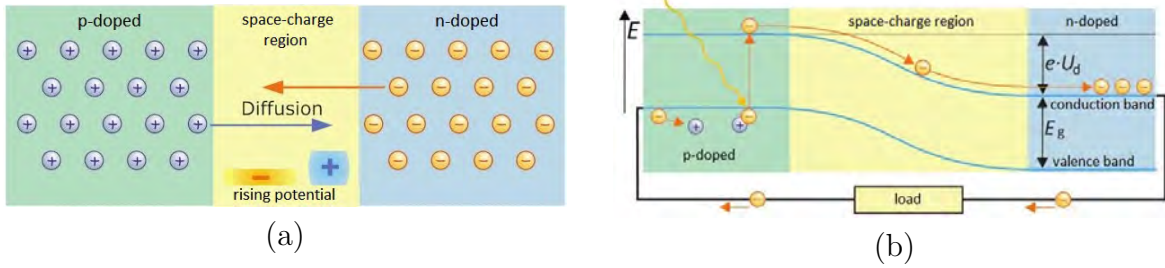


Figure 1.3: Model of the charge carriers in the material (a) and energy band scheme of the p-n junction. Both were taken from [15].

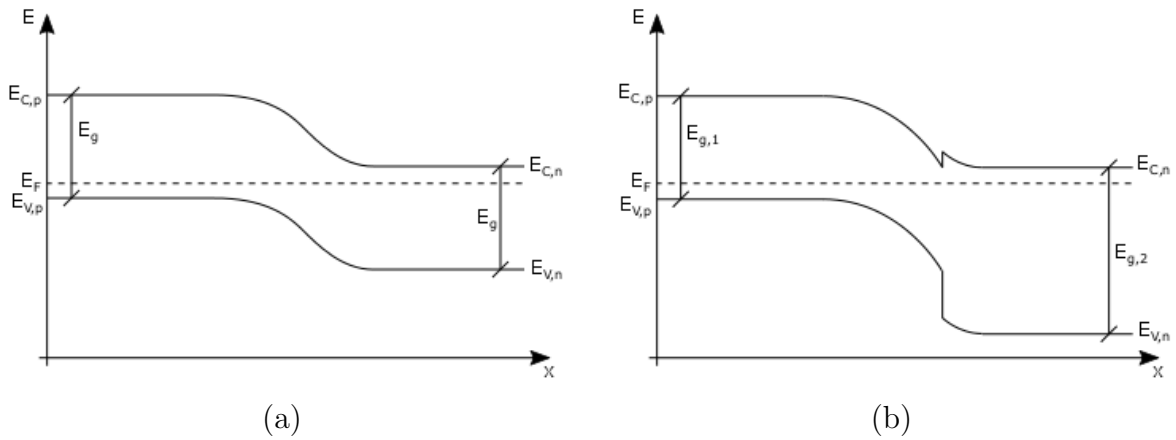


Figure 1.4: Typical energy band structure of a homo- (a) and a heterojunction (b). Redrawn after Ref. [16] and [17]

by differently doping one material (leading to a so called “homojunction”) but also by using different materials like in CIGS cells, thus forming so called “heterojunctions”. A comparison between a typical homojunction and heterojunction can be seen in figure 1.4. In the homojunction, the p- and the n-type semiconductor have the same band gap throughout the whole material and therefore the VB and CB are always equidistant. In a heterojunction, the band gaps are generally not equal, indicated by  $\Delta E_1$  and  $\Delta E_2$ . Therefore the energy bands only are equidistant within each material but at the junction there is a jump in both VB and CB. These jumps can lead to several effects as described later in section 2.4.1.

When an electron is raised to the CB in the p-type material, as indicated in figure 1.3(b) and diffuses to the space charge region without recombining, it is forced to the n-type material side by the electric field and gets collected. It is then available as electric power and can be retransferred to the p-type side via an electrical load, thus completing an electric circuit powered by the incident light.

### 1.2.3 Overview of Photovoltaic Technologies

Since the making of the first photovoltaic device in 1839 by Alexandre Edmond Becquerel out of selenium [18] a lot of different materials have been used to produce solar cells. Today, the most commonly used is Silicon. figure 1.5 shows the development of

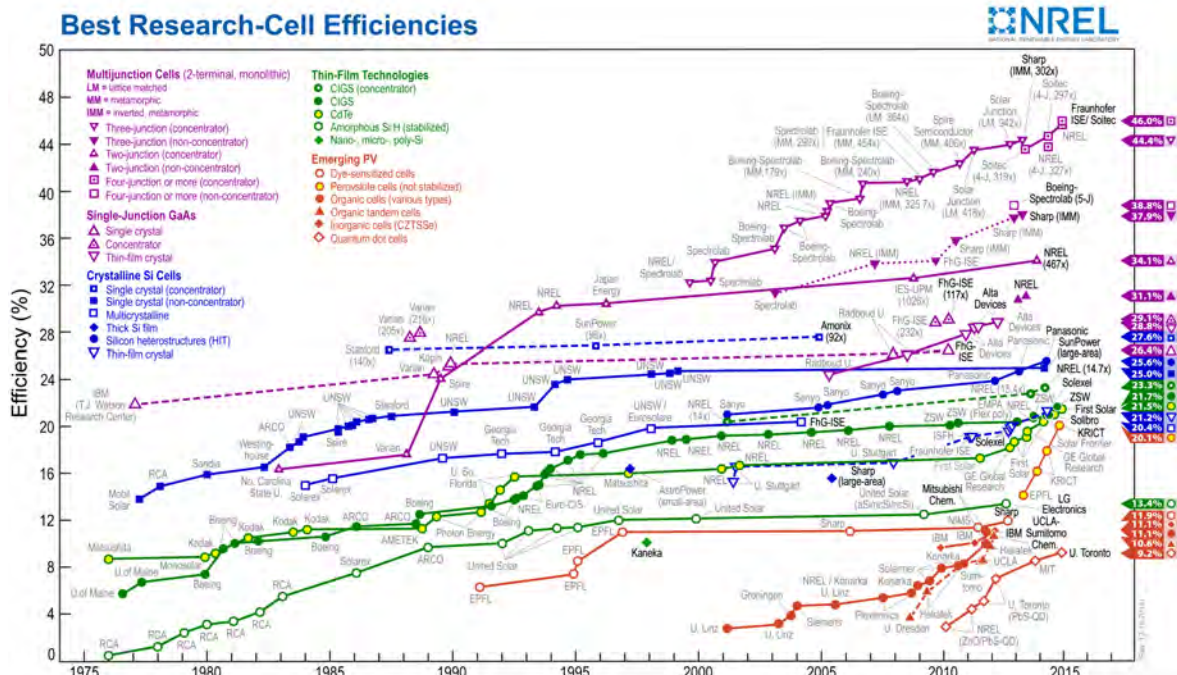


Figure 1.5: Best cell efficiencies of different solar cell techniques. This plot is courtesy of the national renewable Energy Laboratory, Golden, CO

Material	cell-efficiency	module efficiency	costs €/W
c-Si	25.0%	21%	0.74
a-Si	13.4%	11%	0.35
III-V (e.g. GaAs)	46.0%	-	-
CIGS	21.7%	15.0%	0.58
Organic	11.1%	-	-

Table 1.1: Table of material's/technologies' efficiencies. Numbers from 1.5 and [19] and [20]. Prices of September 2013 in Germany and [21]. III-V-modules not commercially sold.

the solar cells efficiency sorted by technology. The most recent records are shown in table 1.1.

### Crystalline Silicon (c-Si)

Most of the produced solar cells are made of either monocrystalline or multicrystalline silicon. Their production has benefited a lot from the knowledge and large-scale production of silicon for microelectronic purposes. 38% of all solar photovoltaic modules sold in 2011 were based on monocrystalline silicon wafers, 51% were based on multicrystalline silicon wafers [19, Chapter 4.2]. Monocrystalline silicon solar cells are most commonly made out of thin wafers cut from monocrystalline ingots prepared by the Czochralski process. An alternative is the floatzone process but is hardly used in commercial production [19]. It is quite expensive to reach the needed purity levels for monocrystalline silicon and the output are circular wafers which are cut to pseu-

dosquares before combining them to modules. This is necessary to cover more of the modules surface with active material but a lot of monocrystalline silicon is wasted. Also the feedstock material for the Czochralski process has to be of good quality.

One way to reduce the material loss and the material costs is to produce multicrystalline silicon. Multicrystalline silicon solar cells have an efficiency 10% lower than cells from monocrystalline silicon which can be almost completely compensated in modules due to their square geometry.

All of these technologies produce silicon ingots that have to be cut into wafers. This cutting process leads to material loss. In order to avoid these losses, there have been investigations on “ribbon silicon”, where sheets of silicon are pulled from molten silicon. Although ribbon silicon wafers were produced on industrial scale and used to produce solar cells, the technology is no longer used up to date.

Boron is used for p-doping and phosphorous for n-doping. The surface is usually structured to decrease light reflectiveness. Due to relatively low absorption coefficients solar cells based on crystalline silicon have bulk thicknesses of 200-500 $\mu m$  [22] Typical efficiencies of commercial crystal silicon modules are 14-20% [19, Chapter 4.2]. The highest reached cell efficiency is 25% for mono- and 20.4% for multicrystalline silicon 1.5.

### Amorphous Silicon (a-Si)

The main advantage of a-Si over c-Si is the higher absorption coefficient which allows a-Si based cells to have much thinner absorber layers (ca 0.2-0.4 $\mu m$  [19] and therefore less silicon is needed, thus reducing the costs of the cell (see table 1.1). The main reason for the higher absorption coefficient is that a-Si is a direct semiconductor.

The main disadvantage of a-Si solar cells is their relatively low efficiency, the record being 13.4%. The main reason for this low value are dangling bonds. To reduce the density of these dangling bonds, protocrystalline and microcrystalline silicon are used. Protocrystalline silicon has no crystal lattice but a higher medium range order than a-Si. Microcrystalline silicon is a mixed phase material consisting of nanosize crystals embedded in amorphous silicon. Because of the different band gaps of a-Si,  $\mu c$ -Si and protocrystalline silicon, they can easily be combined to form tandem cells and reach a higher efficiency.

### III-V Type Solar Cells

III-V solar cells use one element of the third group and one of the fifth group. By combining them in different ratios, p- and n-type semiconductors with various band gaps but similar crystal properties can be created. Therefore III-V materials are used for high efficiency tandem cells with efficiencies up to 46% on cell level (see table 1.2). Typical material compounds are GaAs, InP, InGaP, GaN and GaSb.

Due to their relatively high costs per  $W_p$  but high power output per kg, III-V solar cells are being used in outer space since the 1960s and became standard for satellites in the 1990s.

Number of Junctions	Efficiency in %	
	non-concentrator	concentrator
1	28.8	29.1
2	31.1	34.1
3	37.9	44.4
4	38.8	46.0

Table 1.2: Efficiencies for III-V-compound cells with concentrated and not-concentrated light. Figures from 1.5.

### Copper Indium Gallium Selenium (CIGS) Solar Cells

CIGS is an uprising thin film solar cell technology (see figure 1.6) based on the compound material copper indium gallium selenide, short CIGS. In 1975 Bell Laboratories presented a solar cell with 12% efficiency based on a  $\text{CuInSe}_2$  single crystal. This drew attention to the “new” material and started the development of  $\text{CuInSe}_2$  thin films. In order to avoid the high costs of single crystals an evaporation process was made which led to the first small area CIGS devices with an efficiency of about 5% [17].

Several milestones led to the up to date efficiency of 21.7%. At first the ratio between copper and indium had to be made precisely controllable which was achieved by a triple-source evaporation geometry. This led to the finding that low ratios of copper to indium leads to higher cell efficiencies[17].

The next milestone was the introduction of a CdS buffer layer on top of the CIGS absorber (see figure 1.10). It is around 50nm thick and is attached via a chemical bath. The CdS buffer layer reduces the optical absorption of the CIGS surface which lets more light to the absorber where it leads to a higher efficiency. Furthermore the buffer layer eliminates most of the shunting paths [17]. There are new concepts to replace the poisonous CdS material by Zn based buffer layers [19].

In the 1990s the usage of Na-containing glass substrates was found to improve the cell performance. The indium was partly replaced by gallium and the selenium was partly replaced by sulfur, both leading to a better performance.

Economically seen CIGS technology is very promising with an efficiency of 14.6% for mass production modules and single modules reaching 15.7% [23]. Combined with a projected module costs of  $0.51\$/w_p$  this could lead to 0.06-0.09\$/kWh electricity costs in sunny climates [24]. There are new approaches to completely replace the rare and expensive elements indium and gallium by zinc and tin, leading to the so called CZTS cells [25].

More information on the physical behavior of CIGS solar cells is given in section 1.3.

### Organic Solar Cells

The difficulty with organic solar cells is to find good donor and acceptor materials. The first organic cells were made out of so called (MEH-PPV)/ $C_{60}$  composites, followed by so called PCBM materials. Usage of poly-aryl-thiophenes (P3HT being the best performing of them) led to conversion efficiencies of 7%. The record for stabilized organic solar cells is now 11.1% 1.5. Latest developments are working with so called copolymers as donor materials. Copolymers consist of acceptor and donor polymers



in alternating order. They can be based on different materials like flourene, carbazole, cyclopentadithiophene or metallated conjugated polymers. In 1995 PCBM has first been used as acceptor and although a lot of other materials have been investigated [26], PCBM remains the most used acceptor material [19].

The donor and acceptor material are embedded in a solvent like chlorobenzene, chloroform, xylene, toluene and mixtures of those.

Organic solar cells in general don't produce free charge carriers but instead create excitons (an electron and a hole in an excited state but bound together).

The  $V_{OC}$  of organic cells is largely determined by the difference of the highest molecular orbit (HOMO) of the donor and the lowest molecular orbit (LOMO) of the acceptor.

Organic cells can be well used in tandem cell formations.

A huge advantage of organic cells is that they can be produced at low temperatures from solution and can be scaled largely, thus having the potential to a very good cost/output ratio.

The biggest disadvantage of organic solar cells besides their still relatively low efficiency is their rather low lifetime compared to already established technologies.

### Third Generation Solar Cells

There are a lot of different concepts to exceed the Shockley-Queisser limit for single junction solar cells (which is a conversion efficiency of around 31%). They are summarized as "Third Generation Solar Cells". Some of the most prominent of them are intermediate bands, down- and upconversion and hot carrier cells. Tandem cell concepts are also considered third generation but have already been mentioned with materials where applied.

The principle idea of intermediate bands is to insert an additional energy level in the area close to the junction (not throughout the whole cell). Like this, photons with energies below the band gap energy can lift an electron to the conduction band in two steps. Time plays a big role because electrons in the intermediate band have to absorb a photon before recombining to the valence band. The more photons per time the more likely it is for this concept to achieve an efficiency increase. The photon per time rate can be increased by concentrated light.

Upconversion tries to combine two photons of low energy to one photon with higher energy. To achieve this, a long-lived energy state is necessary where the excited electrons can be stored until the next low energy photon is absorbed. This effect has to be higher than the losses due to the increased recombination rate caused by additional recombination paths over the intermediate band.

Downconversion converts one high energy photon into low energy photons. In order to be beneficial, the quantum efficiency of the downconverting device times the used cell's QE for the outcoming photon wavelength has to be higher than the cell's QE for the high energy photons absorbed by the downconverter:

$$QE_{DC}^{high \rightarrow low} \cdot QE_{cell}^{low} > QE_{cell}^{high} \quad (1.1)$$

There are plenty of further concepts for which the reader is referred to [19, page 283ff].



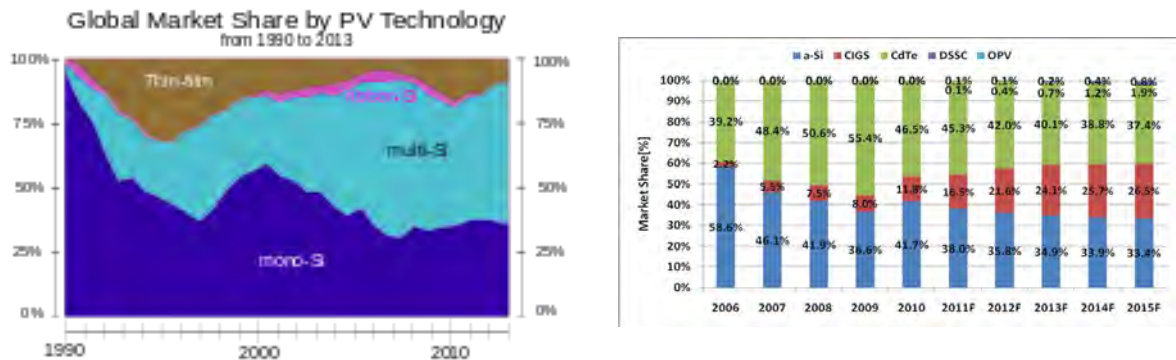


Figure 1.6: Global market share of Photovoltaics by mono, multi and thin film (left hand side) and by thin-film technologies (right hand side)

### 1.2.4 Characterization Methods

There are a lot of different measurement methods to gain information on electrical properties and material characteristics of solar cells. For information on the material structure commonly used measurement methods are several X-Ray techniques, such as X-Ray-diffraction, X-Ray Reflectivity and Grazing-Incidence X-Ray Diffraction and spectroscopy techniques, such as Transmission Electron Spectroscopy, Rutherford Backscattering Spectrometry and Raman Spectroscopy [19, chapter 3]. They can be used to gain information on crystal properties, absorption coefficients and so forth and so on. They help to get a deep and profound understanding of the physical processes going on inside the cell.

The measuring techniques on electrical properties help to find the efficiency and performance of a cell under light. These techniques are among others Photoluminescence (PL), Electroluminescence (EL) Thermography, Quantum efficiency (QE) and voltage-current measurements (IV-curves).

#### Electroluminescence (EL)

When a solar cell is driven by an external forward bias, it emits light. This is because the electrons driven through the solar cell, which is basically a diode, recombine via radiative recombination (also via Auger recombination, but there no detectable radiation is emitted), thus emitting a photon [27]. The energy of these emitted photons is in the range of the band gap. Photons are only emitted from regions of the cell, that are connected to the biased contacts, making EL a very good measuring method for broken cells. An example of a silicon module measured with EL can be seen in figure 1.7 with a broken cell in the center.

With EL damages like broken cells, microcracks and efficiency losses due to production insufficiencies (print problem, bad contacts, ...) can be detected.

The emitted photons are detected with CCD arrays like the ones in digital cameras but optimized for wavelengths of around 1000 nm. To get a better response, InGaAs detectors can be used, which enable faster data acquisition but are far more expensive.

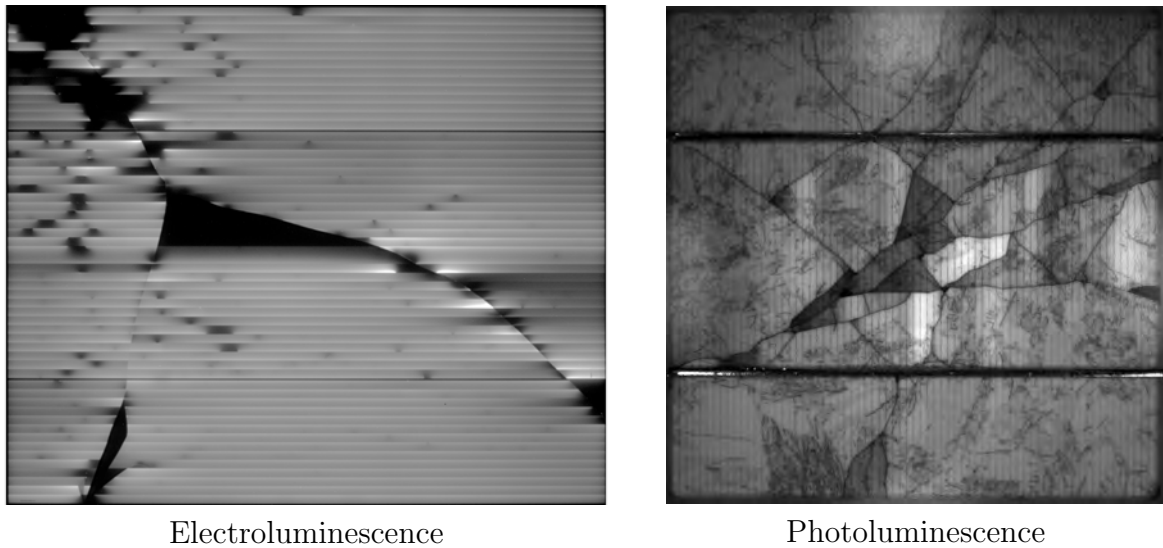


Figure 1.7: Electroluminescence of a a-Si module and Photoluminescence of a polycrystalline silicon cell. In EL, some spots are completely dark, whereas in PL even the parts without electrical connection show details.

### Photoluminescence (PL)

One main disadvantage of EL is that it gives no information concerning the photo-generation on the broken parts of a solar device because the electrons of unconnected parts are not excited by the external bias. PL solves this problem by exciting the electrons via light illumination. Although solar cells usually absorb most incident light and therefore the picture taken by the camera doesn't see a lot of reflections, it is better to excite the cell by light of much higher energies than the band gap energy and putting a filter in front of the camera, that only transmits light close to the band gap energy. Like this, the incident light (e.g. green light from LEDs) excites the electrons in the solar cell, that then relax thermally to the lower edge of the conductive band and then recombine like in EL, thus emitting higher wavelength light to the camera.

Like this, unconnected parts of broken cells can be examined as can be seen in figure 1.7

### Thermography

Like in EL thermography uses a camera to make pictures from a solar device under bias, but in thermography light of a different wavelength range is collected (typically long infrared from 9000-14000 nm [28]). This means that it collects thermal irradiance giving information on the temperature of the measured surface. By this defects like hot spots can be detected. Thermography can not only be used in the lab, but also directly on the field without having to disturb the photovoltaic energy collection.

To improve the resolution of thermography, *lock-in thermography* can be used. It analyzes a periodically heated PV device via Fourier analysis. The improved resolution can be seen in figure 1.8.

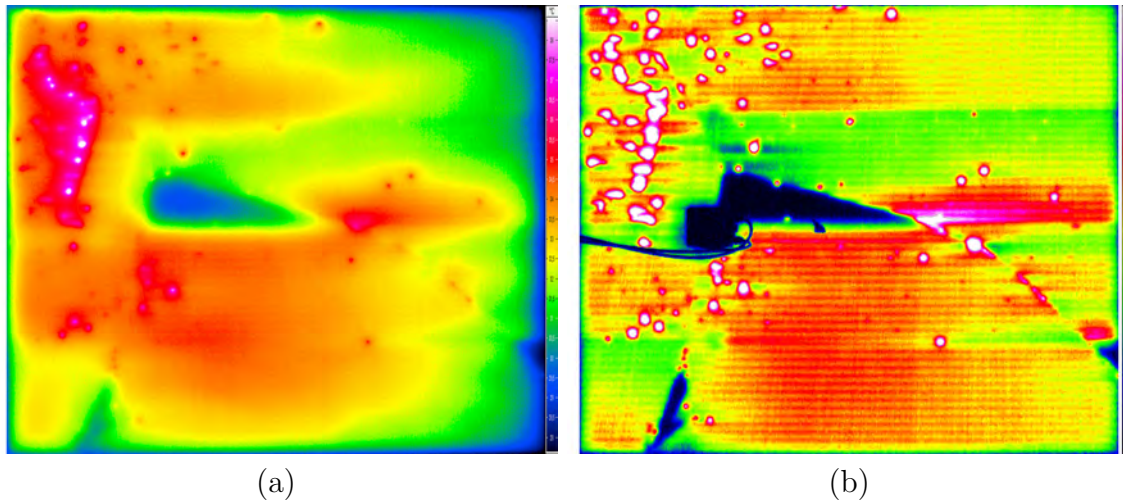


Figure 1.8: Results of thermography (a) and lock-in thermography (b) of a a-Si cell. Lock-in thermography has a higher resolution.

### Quantum Efficiency (QE)

Quantum efficiency measurements are used to gather information on the wavelength dependent performance of a PV device. To achieve this, a light beam of a narrow wavelength band is pointed on the device and the resulting current is measured. This gives information on how efficiently the device converts light of a certain wavelength into electric power. A closer look at this method is given in chapter 2.3.

### Voltage-Current-Curve (IV-curve)

The IV curve is the diode characteristics of the solar device in the dark or under illumination. The usual illumination is an AM1.5 spectrum at  $1000 \text{ W/m}^2$  and at  $25^\circ\text{C}$  (standard testing conditions (STC)). By changing the bias on the cell by external electronics, data pairs of voltage and current are collected which can then be plotted to obtain a curve like the blue one in figure 1.9.

To get the cell's efficiency, one simply multiplies the current and voltage value of each data point (leading to the red curve in figure 1.9. The maximum of this curve is the maximal power the cell can generate ( $P_{MPP}$ ). Dividing it by the illumination power leads to the cell's efficiency  $\eta$ . The point of the IV-curve, where the power is maximal, is called maximum power point.

Further information on IV-curves is given in chapter 2.2.

## 1.3 Copper Indium Gallium Selenide (CIGS)

As mentioned in section 1.2.3 CIGS-technology is an uprising technology on the PV market. It has reached an efficiency of 21.7% for a cell and above 16% for modules [29]. CIGS is a semiconductor material composed of copper, indium, gallium and selenium with a chalcopyrite ( $\text{CuFeS}_2$ ) crystal structure. Its chemical formula is  $\text{CuIn}_x\text{Ga}_{(1-x)}\text{Se}_2$  where  $x$  can vary from 1 to 0. It has a band gap between 1.7eV (when  $x=0 \Rightarrow$  copper gallium selenide (CGS)) and 1.0eV (when  $x=1 \Rightarrow$  copper indium

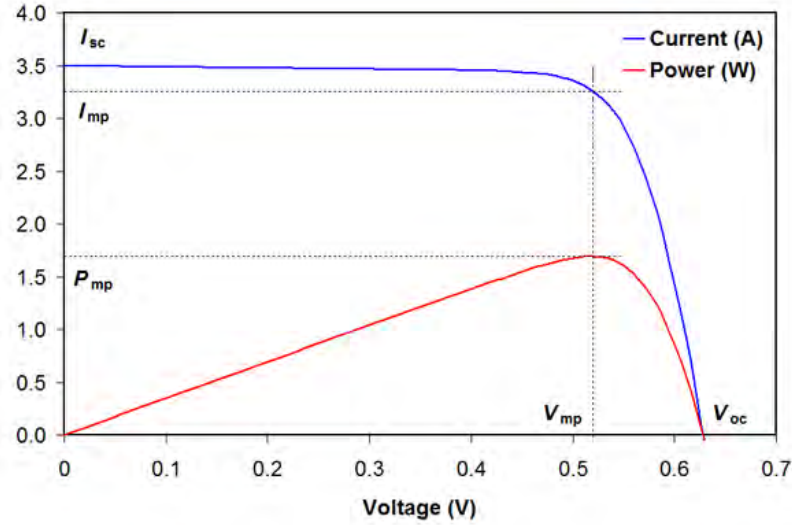


Figure 1.9: Current (blue) and power (red) versus voltage measured from c-Si solar cell.

Defect type	Energies [eV]		
Vacancy <sub>Cu</sub>	0.024		
Vacancy <sub>In</sub>	0.165	0.400	0.659
Cu <sub>In</sub>	0.282	0.565	
In <sub>Cu</sub>		0.694	0.776
Cu <sub>i</sub>			0.824
In <sub>Cu</sub> + V <sub>Cu</sub>			0.824

Table 1.3: Defect transition energy for CuInSe<sub>2</sub>. Valence band at 0 eV, conduction band at 1.05 eV. Data taken from [19, figure 7.9]

selenide (CIS)). The first chalcogenide cells were made from CIS, gallium was added later to increase the  $V_{OC}$ [17]. CIGS has a high absorption coefficient of around  $10^5 \text{ cm}^{-1}$  for visible light which rapidly decreases at a photon wavelength of around 1080nm (still  $2 \cdot 10^4 \text{ cm}^{-1}$ ) [19]. The position of the decrease mainly depends on the bandgap, 1080nm correspond to a band gap of 1.15eV. Therefore it can be used for thin film solar cells. A typical architecture with the thicknesses of the different layers of a CIGS-cell is shown in figure 1.10. It also shows a buffer layer made of CdS, which is nowadays often replaced by cadmium free buffer materials like Zn(O,S) to avoid the usage of poisonous cadmium.

### 1.3.1 Cell architecture

CIGS cells consist of several layers that are successively deposited onto the substrate. The structure of a final device can be seen in figure 1.10 and is explained in more detail below.

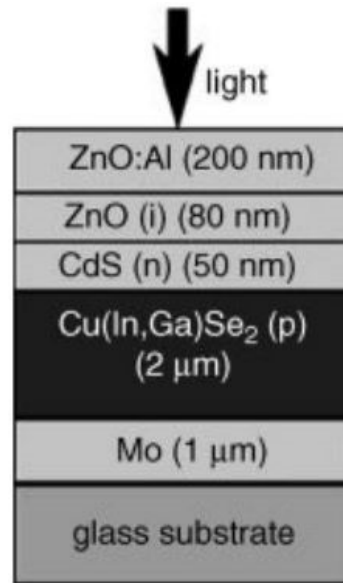


Figure 1.10: CIGS cell architecture: Glass substrate, Molybdenum back contact, CIGS layer (not to scale), buffer layer, front contact (TCO window)

### Substrate

CIGS-cells are usually produced in the substrate configuration (unlike most CdTe solar cells, which are produced on superstrates) on soda lime glass because it has approximately the same thermal expansion coefficient as CIGS. The soda lime glass also acts as sodium source for the absorber. In order to avoid Na oversupply sometimes diffusion barriers like  $\text{SiN}_x$  or  $\text{SiO}_x$  are used. The typical thickness of the soda lime glass substrate is 2-3mm. Due to the high weight there have also been attempts to use thinner glass of around 1mm. To obtain flexible CIGS modules, alternative substrates such as polymers and metals can be used. When using polymers as substrate, the production temperature is limited to  $420^\circ\text{C}$  because of the higher temperature expansion coefficient of polymers. Metal substrates need additional layers for electrical barrier and diffusion barrier. Both polymer and metal substrates have been used and proven to reach acceptable cell performances [17].

### Back Contact

Most CIGS cells have a Molybdenum (Mo) back contact. Mo has a high melting point of around  $2700^\circ\text{C}$  and can be sputtered onto the substrate at  $300\text{-}400^\circ\text{C}$ . Its costs are relatively low and its diffusivity is expected to be low. The typical resistivity of Mo back contact layers in CIGS cells is  $10\mu\Omega\text{cm}$  and the sheet resistance is  $200\text{m}\Omega$  [17, p254].

Although Mo has a very low reactivity with selenium (Se) or sulfur (S), a 100nm thick film of  $\text{MoX}_2$  ( $\text{X}=\text{Se}$  or  $\text{S}$ ) forms when higher temperatures than  $500^\circ\text{C}$  are reached during the production process. The thickness of this intermediate layer mainly depends on the processing temperature, the Na concentration and the gallium (Ga) content of the CIGS material.  $\text{MoS}_2$  and  $\text{MoSe}_2$  are semiconductive materials with indirect band gaps of 1.06-1.16eV ( $\text{MoSe}_2$ ) and 1.17-1.35eV ( $\text{MoS}_2$ ). They form another junction in

the cell but with very low barrier height and can therefore be considered as ohmic.

The optical reflectivity of Mo is rather poor in the visible spectrum (around 60%) and therefore new materials are being tested, for example Ta, Nb and W [17, p255].

Often the Mo-film is deposited in two stages: under high and under low gas pressure. This is because high pressure leads to a better adhesion to the substrate and low gas pressure leads to a film with lower electrical resistivity [19].

### Absorber Layer

The absorber layer consists of  $\text{Cu}(\text{In,Ga})(\text{S,Se})_2$ . The  $\text{Cu}/(\text{In}+\text{Ga})$  ratio is smaller than 1 (Cu-poor composition), contrary to what the formula is suggesting. The ratio between In and Ga is usually chosen according to  $\text{Ga}/(\text{In} + \text{Ga}) = 0.2 - 0.3$ , because this leads to the highest efficiency of the cell [17] with an energy band gap of around 1.14eV. The CIGS material is also sodium doped, most commonly by diffusion from the soda lime glass. It turned out that Cu rich growth of CIGS leads to bigger grains and less grain boundaries and therefore more efficient cells. To use this advantage even though the end material has to be poor in Cu, the growth process is always designed to contain Cu rich stages.

The CIGS absorber material is usually designed as the p-type material. The main acceptors are defects, that are caused by the non-stoichiometric growth of the CIGS layer [17].

There are several different ways to grow the CIGS absorber layer upon the Mo back contact, one of them being co-evaporation. In this method elemental fluxes are directed onto the Mo back contact and crystallize directly from the gas phase. In order to obtain Cu rich growth phases, the elements are evaporated at time variable rates, which is then called staged co-evaporation process (2 and 3 stages are used). The main disadvantages of co-evaporation processes are the need to permanently measure and control the evaporation fluxes of every element and the need for a relatively expensive vacuum chamber.

Deposition reaction processes solve the two main problems of co-evaporation by using two steps. In the first step, several precursor layers are deposited onto the Mo back contact. Those materials are chosen in a composition so that they form a CIGS layer with the desired element ratios when heated. The amount of elements in the precursor layers can easily be determined by measuring the layers thicknesses via X-Ray spectroscopy. The main disadvantage of the deposition reaction process is that it is impossible to have Cu rich growth phases.

As mentioned before, the elements Ga and Na are added to the basic chalcogenide (CIS) to obtain solar cells with higher efficiencies. The improvement by Ga is mainly due to an increase in  $V_{OC}$  and FF which is largely due to an increase of the band gap. A locally increased Ga content compared to the rest of the material at the back contact acts as a back surface field and thus further improves the cells efficiency.

As mentioned before, Na diffused in the absorber layer increases the cells performance. There are two possible ways to obtain a Na doped absorber layer: By using soda lime glass, as described before, or by a Na containing precursor layer. In the final absorber the Na is located at the grain boundaries rather than inside the CIGS grains. The preferential concentration is about 0.1at% or  $2 \cdot 10^{19} \text{cm}^{-3}$ .

Another interesting aspect is the S/(Se+S) ratio. When added to pure CuInS<sub>2</sub>, S increases the  $V_{OC}$  and the carrier lifetime, but too high concentrations reduce the carrier concentration. Therefore the optimal S concentration is around  $10^{17} \text{cm}^{-3}$ .

Thanks to the high light absorption coefficient of CIGS ( $\alpha \approx 10^5 \text{cm}^{-1}$  [19] in the visible spectrum) the absorber layer only needs to be around  $2 \mu\text{m}$  thick, while c-Si solar cells have thicknesses of 100-200  $\mu\text{m}$ .

#### Buffer Layer

A buffer layer in CIGS solar cells has first been used in 1987 [30]. It was made of CdS, a material that is still used as buffer layer material. Because of the toxicity of Cd, new buffer layer materials are tested based on materials like ZnS, ZnSe, ZnO and InS. The best performing is Zn(OH,O,S) which is already used in production [31].

The buffer layer increases the cell's performance by preventing shunts, modifying the absorbers surface and protecting the absorber from damage during the TCO attachment process.

Possible processes for buffer layer deposition are chemical bath deposition (CBD), atomic layer deposition (ALD), metal organic chemical vapour deposition (MOCVD), ion layer gas reaction (ILGAR), sputtering, thermal evaporation and electrodeposition (ED) [32].

CdS buffers are produced by chemical bath deposition. The growth rate is around  $0.3 \text{nm s}^{-1}$  and the grain size of the end product is approximately 20-30nm. Typical thicknesses of the buffer layer are 50nm.

#### Window Layers

The window of CIGS cells consists of two layers: a high resistance layer made out of ZnO and a low resistance layer out of ZnO:Al and represents the n-type layer of the CIGS solar cell. The main donors are the Al dopants.

The high resistance ZnO layer is rather expensive to produce but has several advantages. The performance of the cells is more reproducible when a high resistance ZnO layer is used, stable under damp-heat conditions and diffusion of the low resistance window layer dopant is prevented. ZnO window layers are attached by sputtering, spray deposition or MOCVD [17] and have a thickness of 50-100nm.

The low resistance window layer provides high electrical conductivity while absorbing as little light as possible. The doping must be held low in order to not absorb low energy light, which can still be converted by the small band gap absorber ( $\sim 1.15 \text{eV}$ ). Therefore the dopant concentration should be below 2%. The low resistance ZnO:Al window layers are deposited by sputtering.

The reflectivity of a ZnO:Al/ZnO/CdS/CIGS cell is small and even without antireflection coating quantum efficiencies of over 90% can be reached.

## 2 Theory

This chapter outlines the most important theoretical concepts used for the measurements of this thesis. i.e.: QE, correlation between  $V_{OC}$ ,  $I_{SC}$ , FF,  $P_{MPP}$  and physical parameters like material properties, irradiance and temperature.

### 2.1 Functional Description of Solar Cells

#### 2.1.1 Electrons in Semiconductors

As mentioned in section 1.2.2, semiconductors have a valence band (VB), which contains the valence electrons and a conductive band, the lowest energy band with unoccupied states. Typical energy band gaps for semiconductors are between 0.5 eV and 3 eV. At a (theoretical) temperature of 0 K, all the electrons are found in the VB and none in the CB and no electric current can be transported because there is no space to move. When the temperature is increased, some electrons are excited to the CB, thus making electrical transport possible. Every electron excited to the CB leaves behind a hole, which can be filled by surrounding electrons, leaving behind new holes. This shows that in the VB, it is more effective to describe the movement of a hole instead of all the electrons involved in a charge transport.

A very useful parameter to describe the behavior of electrons and holes in a semiconductor is the *effective mass*  $m^*$ :

$$\frac{1}{m_c^*} = \frac{1}{\hbar^2} \frac{\partial^2 E_c(k)}{\partial k^2} \quad (2.1)$$

for the electrons in the conductive band and

$$\frac{1}{m_v^*} = \frac{1}{\hbar^2} \frac{\partial^2 E_v(k)}{\partial k^2} \quad (2.2)$$

for the holes in the valence band.

Another important parameter is the *Fermi energy*  $E_F$ . It is the energy to which electron states are filled at a temperature of 0 K. At higher temperatures, states above  $E_F$  are also filled. This leads to the *electron density*  $n$  and *hole density*  $p$ . With the Boltzmann approximation, they become

$$n = N_c \exp\left(\frac{E_F - E_c}{k_B T}\right) \quad (2.3)$$

and

$$p = N_v \exp\left(\frac{E_v - E_F}{k_B T}\right) \quad (2.4)$$



with  $k_B$  being the Boltzmann constant,  $N_c$  the effective conduction band density of states and  $N_v$  the effective valence band density of states:

$$N_c = 2 \left( \frac{m_c^* k_B T}{2\pi \hbar^2} \right)^{3/2} \quad (2.5)$$

$$N_v = 2 \left( \frac{m_v^* k_B T}{2\pi \hbar^2} \right)^{3/2} \quad (2.6)$$

These equations show, that the product  $np$  is a constant for any given material at a given temperature,

$$np = N_c N_v e^{-E_g/k_B T}. \quad (2.7)$$

with  $E_g$  being the band gap energy.

This leads to the definition of the so called *intrinsic carrier density*  $n_i$

$$n_i^2 = np = N_c N_v e^{-E_g/k_B T}. \quad (2.8)$$

A gradient in the charge carrier density leads to diffusion of the charge carriers due to a difference in density and to a drift due to the electric field resulting from a charge carrier gradient. These two effects lead to the charge carrier current densities

$$J_n = q D_n \nabla n + q n \mu_n F \quad (2.9)$$

$$J_p = -q D_p \nabla p + q p \mu_p F \quad (2.10)$$

with  $q$  being the electron charge,  $F$  being the electric field and by using the *Einstein relations*

$$\mu_n = \frac{q D_n}{k_B T}, \quad \mu_p = \frac{q D_p}{k_B T}, \quad (2.11)$$

relating the charge carrier mobility  $\mu$  to the diffusion constant  $D$ .

The charge carrier current densities can also be related to the Fermi Energy gradients  $\nabla E_{F_n}$  and  $\nabla E_{F_p}$

$$J_n = \mu_n n \nabla E_{F_n} \quad (2.12)$$

$$J_p = \mu_p p \nabla E_{F_p} \quad (2.13)$$

This means that a local difference in  $E_F$  leads to a charge carrier transport until the force caused by resulting electric field and the force by charge carrier density are in equilibrium. This is especially interesting when having different materials with different Fermi energies next to each other, leading to so called *p-n junctions*.

## 2.1.2 Junctions

When putting two different materials together, one obtains a junction at the interface. The characteristics of the junction depend on the properties of the materials relatively to each other. By matching a material with a Fermi energy close to the valence band (p-type) with one with a Fermi energy close to the conductive band (n-type), an internal electrical field is established. With the use of this field incident photons can be transformed to electric power.

In crystalline silicon solar cells, the most commonly used technique, the p- and n-type material are both based on highly pure crystalline silicon. To change the Fermi energy, the crystal is doped with atoms with either less valence electrons (acceptors, p-type) or with more valence electrons (donors, n-type). A typical element for p-doping is Boron. Doping with boron leads to a higher concentration of holes in the VB, while the electron concentration in the CB decreases. However, the intrinsic carrier density stays the same. Because  $p > n$ , the holes in p-type semiconductors are called *majority charge carriers* and the electrons are called *minority charge carriers*. An element typically used for n-doping is Phosphorus. Here,  $n > p$ , therefore the electrons are called *majority charge carriers* and the holes are called *minority charge carriers*. Silicon is usually doped in concentrations of parts per million to avoid defects in the crystal which would lead to unwanted recombination of charge carriers. At such low doping concentration, the energy band gap remains the same as for pure silicon. The resulting junction is therefore called *homojunction*.

Another way of creating p-n junctions is to use completely different materials instead of similar materials with different doping, like CIGS cells for example. Then, the energy band gaps of the p-type material and the n-type material are generally no longer equal and *heterojunctions* are formed. This leads to sudden changes in the band energies (vertical lines in the band energy diagram) as can be seen in figure 1.4 (b).

These sudden changes are called band offsets and can cause electron barriers leading to anomalies in the cell's behavior as explained in section 2.4.1. A band offset is called positive, if a charge carrier has to spend energy when passing it from the material with small to the material with large energy band gap and negative if the charge carrier gains energy when passing it. Another way to classify the offsets are the expressions spike (positive barrier) and cliff (negative barrier).

## 2.1.3 Absorption of Photons

Another important mechanism for the performance of a solar cell is the absorption of photons. As described above, every material has electrons at states of certain energies. An incident photon can interact with the electron, giving it its energy and momentum and exciting it to another state. This process is called photon absorption. The probability of a photon being absorbed depends on the density of electrons and the energy states the electron can be excited to. The more possible states there are, the more likely it is for the photon to get absorbed. The electron's transition from one state to another can either be direct or indirect, depending on the momentum of the initial and the final state. For indirect band gaps, a phonon from the material is needed to change the electrons momentum. Such a three particle interaction (electron, photon,

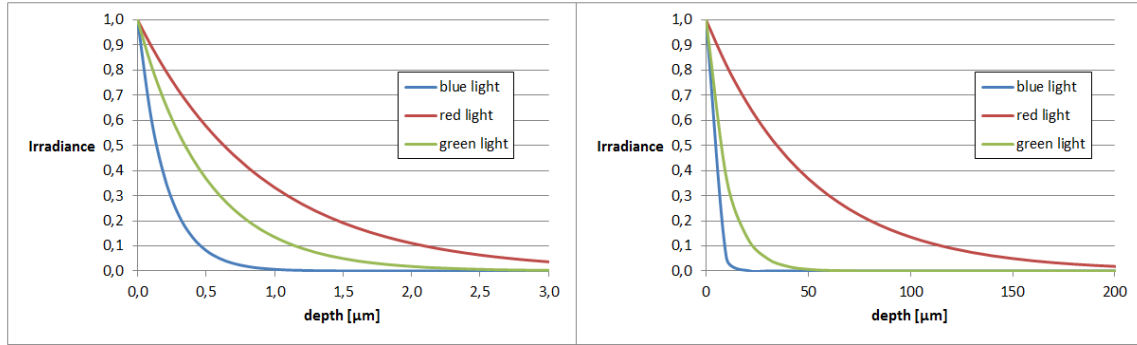


Figure 2.1: Absorption of light beam of different wavelengths according to Lambert's Law for CIGS (left) and c-Si (right).

phonon) is far less probable than a two particle interaction (electron, photon) of a direct transition. This is the reason why indirect semiconductors like crystalline silicon need to have thicker absorbers (several hundred  $\mu\text{m}$ ) than direct semiconductors as CIGS (around 2  $\mu\text{m}$ ) to absorb most of the incident light.

This behavior can also be described by the absorption coefficient  $\alpha$ , which is the imaginary part of the index of refraction. The absorption coefficient (also called attenuation coefficient) is a measure for how quickly a beam (of photons, electrons, neutrons, ...) is weakened to  $1/e$  of the initial intensity in a material, its unit being  $\text{m}^{-1}$ . In case of photons, the absorption coefficient is wavelength dependent. The absorption coefficient of CIGS is around  $10^2$  times as high as the one of silicon in the visible light.

The absorption coefficient is part of the exponent in the Lambert's Law

$$I(l) = I_0 e^{-\alpha l}. \quad (2.14)$$

It describes the decrease of intensity of a radiance beam traveling through a material, where  $\alpha$  is the absorption coefficient of the material,  $l$  the path length the beam has traveled through the material.  $I_0$  is the initial irradiance when entering the material and  $I(l)$  is the irradiance after a path length of  $l$ .

With Lambert's law and knowledge of a solar cell's architecture and the absorption coefficients of its materials, it can be calculated where photons of a certain wavelength are most likely to be absorbed by the solar cell. As can be seen in figure 2.1(left), in CIGS around one third of the blue light is absorbed in the buffer layer (first 0.05  $\mu\text{m}$ ), acting as the n-type semiconductor of the junction, while red light mostly passes the window and buffer layer and is absorbed in the CIGS absorber layer. In c-Si modules, the red light is not fully absorbed before 300  $\mu\text{m}$ .

## 2.2 Current Voltage curves (IV curves)

As mentioned in chapter 1.2.4, IV-curve measurement is a characterization method for photovoltaic devices that gives information on a lot of cell parameters like  $I_{SC}$ ,  $V_{OC}$ , fill factor (FF) and  $P_{MPP}$ . This information can be used to discuss the processes taking place inside the cell, which is one main goal of this thesis.

$V_{OC}$ ,  $I_{SC}$  and FF give a lot of information on the amount, the type and the position of defects in the cell as has been described in section 1.2.2. A more detailed description is given in section 2.2.1.

### 2.2.1 Short Circuit Current and Open Circuit Voltage

When measuring IV-curves, it is important to know the external parameters that can influence the measured outcome. The two most important external parameters influencing the IV-curve are the incident irradiance and the temperature of the measured device as is shown by the equations

$$V_{OC} = \frac{kT}{q} \cdot \ln\left(\frac{I_{SC}}{I_0} + 1\right) [16] \quad (2.15)$$

$$I_{SC} = -I_L = -q \cdot G \cdot (L_n + L_p + W) \quad (2.16)$$

, where

$$I_0 = q \cdot \left( \frac{D_n}{L_n} n_p + \frac{D_p}{L_p} p_n \right) \quad (2.17)$$

where  $L_n$  and  $L_p$  are the diffusion lengths of electrons and holes respectively and  $G$  is the generation rate.  $W$  is the width of the space charge region.  $D_n$  and  $D_p$  are the diffusion coefficients of electrons and holes respectively.  $n_p$  is the electron density in the p-type region and  $p_n$  is the hole density in the n-type region. The diffusion lengths are widely independent of the irradiation and therefore the short circuit current is widely linear with the generation rate and therefore the irradiance. This means, that for comparable measurements, the irradiation has to be kept constant because changes in the irradiance directly affect the  $I_{SC}$ . This behavior led to the IEC Norm 60904, discussed in section 2.2.3. The  $I_{SC}$  is also temperature dependent but the effect is very small.

$L_n$ ,  $L_p$  and  $W$  are material dependent and do not change significantly under illumination or temperature changes. Their effects due to such changes can therefore be neglected.

Equation (2.15) shows, that  $V_{OC}$  is also irradiance dependent because it depends on  $I_{SC}$  which depends on the irradiance. From equation (2.15) the temperature dependence of  $V_{OC}$  can be derived.

$$\frac{dV_{OC}}{dT} \approx \frac{k}{q} \ln\left(\frac{I_{SC}}{B}\right) = \frac{1}{T} \cdot \left(V_{OC} - \frac{E_g}{q}\right) \quad (2.18)$$

with  $B$  being a temperature independent constant. The change is always negative, because  $q \cdot U_{OC} < E_g$ . Typical values for different solar cell materials and technologies are given in table 2.1.

Material	$P_{MPP}$ $\gamma_{rel}$ (%/°C)	$V_{OC}$ $\beta_{rel}$ (%/°C)	$I_{SC}$ $\alpha_{rel}$ (%/°C)	FF $\kappa_{rel}$ (%/°C)
c-Si	-0.45	-0.33	+0.06	-0.19
a-Si	-0.13	-0.33	+0.12	+0.10
CdTe	-0.21	-0.24	+0.04	-0.04
CIGS	-0.36	-0.31	+0.02	-0.08

Table 2.1: Table of technologies' temperature coefficients. Numbers from [33][Table 1]

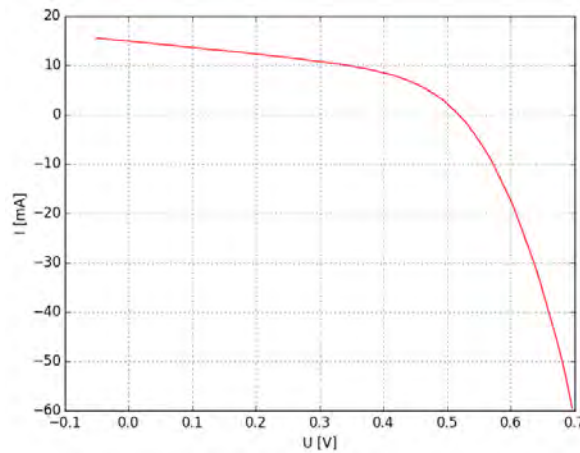


Figure 2.2: IV-curve of a CIGS cell under standard testing conditions.

CIGS devices have a temperature coefficient of  $-0.31\%/^{\circ}\text{C}$  for  $V_{OC}$ . This means that in order to limit the temperature induced changes in  $V_{OC}$  to less than 1%, the temperature has to be kept within a range of  $\pm 1.61^{\circ}\text{C}$ . As explained in section 3.3, the temperature difference could be kept below  $\pm 0.5\%/^{\circ}\text{C}$ . For precise measurements of  $P_{MPP}$  the range must be less than  $\pm 1.39^{\circ}\text{C}$ .  $I_{SC}$  and FF are far less sensitive to changes in temperature.

### 2.2.2 Four-Point probes Method

According to Ohm's Law, the electrical characteristics of an electric circuit (under direct current (DC)) are connected by

$$V = R \cdot I, \quad (2.19)$$

where  $V$  is the voltage,  $R$  the ohmic resistance and  $I$  the current. The voltage can be measured by a voltmeter (which has high internal resistance), the current by an ammeter (having low internal resistance). Simultaneously measuring the voltage and current of a photovoltaic device leads to the IV-curve of the device, containing very interesting information on the device's performance. The easiest way to do so is by contacting the device with two metallic contacts and sending a current through them while measuring the voltage difference. However, there always is a contact resistance, that is not known. Especially in low-resistance measurement, this contact resistance

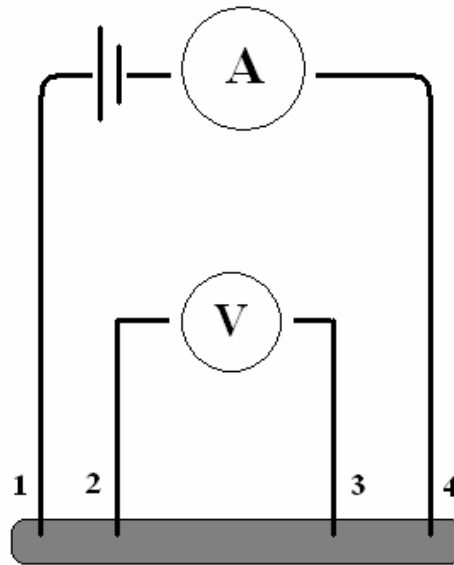


Figure 2.3: Principle of the four-point measuring method.

can lead to significant errors of the measurement, because according to Ohm's Law, it causes a voltage drop of

$$\Delta V = R_c \cdot I$$

at every contact.

One way to highly reduce this error is by using the four-point method [34]. The four-point method uses four contacts, two for the current (force connections) and two for the voltage (voltage connections) (see figure 2.3). The contact resistances of the force connection circuit don't affect the current flowing through the measured device due to Kirchhoff's Current Law. Because of the high (ideally infinite) internal resistance of the voltmeter, the current passing the contacts of the voltage connection circuit is very small (ideally zero). Therefore the voltage drop at the voltage connection contacts is small (ideally non-existent) compared to the voltage drop through the measured device.

When measuring IV-curves of solar cells, it is highly recommended to use the four-point method.

### 2.2.3 Norms for IV-curve Measurements

As shown in section 2.2.1 the performance of a cell in an IV-curve measurement depends on the irradiation and temperature of the cell during the measurement. As shown in chapter 2.3 the performance of a cell also depends on the spectrum of the incident light. To obtain repeatable results, all these parameters have to be held stable. The IEC has defined international norms for IV-curve measurements so the data can be compared easily. There are three major classes for sun simulators, depending on their performance (see table 2.3). The requirements for sun simulators are given in the IEC norm 60904 and are summarized in the following.

	Wavelength range nm	Percent of total irradiance in the wavelength range 400 - 1100 nm
1	400-500	18.4%
2	500-600	19.9%
3	600-700	18.4%
4	700-800	14.9%
5	800-900	12.5%
6	900-1100	15.9%

Table 2.2: Ranges of the solar spectrum according to IEC norm 60904 to determine the spectral match classification of a solar simulator.

### Uniformity

The incident light has to have a uniform irradiance over the designated test area, i.e. where the cell is going to be measured. In case a reference cell is used, the test area also includes the reference cell. To measure the (non-) uniformity, the irradiance on the test area has to be measured at several points with a detector, for example a pyranometer, a reference cell or a spectrometer. The non-uniformity is defined as

$$Non - uniformity(\%) = \left[ \frac{maxirradiance - minirradiance}{maxirradiance + minirradiance} \right] \times 100\% \quad (2.20)$$

For an A class sun simulator, the non-uniformity has to be below 2% over the whole test area.

### Spectral Match

The spectrum of the incident light has to be as close as possible to the spectrum of an AM1.5 irradiance, that is the incident light spectrum coming from the sun through 1.5 atmospheres with no clouds in the sky. The AM1.5 spectrum can be seen in figure 2.9.

To measure the spectral match, the spectrum is split into 6 ranges as can be seen in table 2.2. For each range, the percentage of the total irradiance of the solar simulator's spectrum is compared to the percentage of the AM1.5 spectrum. The largest deviation in percent determines the overall spectral match classification according to table 2.3.

### Time Stability

The irradiance doesn't only change over space, as considered in non-uniformity (see equation (2.20)), but also over time. It is important to consider two different time scales. Short term changes are changes in the irradiation within the data sampling time of one IV-curve measurement. Long term changes means changes over the whole experiment. When the experiment consists of only one IV-curve measurement, the short term and long term instability are the same. For experiments like light soaking, the long term instability is the instability over the duration of the whole light soaking process.

Classification	Spectral match	Non-uniformity	Short term instability	Long term instability
A	0.75 - 1.25	2%	0.5%	2%
B	0.6 - 1.4	5%	2%	5%
C	0.4 - 2.0	10%	10%	10%

Table 2.3: Definition of solar simulator classifications according to IEC norm 60904.

The temporal instability (short and long term equally) is defined as

$$\text{temporal instability (\%)} = \left[ \frac{\text{maxirradiance} - \text{minirradiance}}{\text{maxirradiance} + \text{minirradiance}} \right] \times 100\% \quad (2.21)$$

meaning the maximum and minimum irradiances of the time to be considered (different for short and long term). When multiple IV-curves are measured, the worst short term instability has to be used. The temporal instability classification can be seen in table 2.3.

### Temperature

For temperature effects a different norm applies, because the temperature is not determined by the solar simulator but rather the measurement setup, which might also include cooling systems. The applicable IEC norm is norm number 60891. It holds information on the necessary temperature corrections when the temperature can't be held stable at 25°C. As mentioned in section 2.2.1 the characteristic properties of a solar cell can be corrected (see also table 2.1).



## 2.3 External Quantum Efficiency (EQE)

[35]

As mentioned in section 1.2.4, quantum efficiency (QE) measurement is a characterization method for photovoltaic devices that gives information on its wavelength dependent performance. Such information is highly relevant when experimenting with solar cells under colored light, like is done in this thesis. To perform QE measurements, a monochromatic light beam of known irradiance is needed.

Section 2.3.1 discusses the definition and principles of QE, section 2.3.2 explains how monochromatic light can be produced by using a monochromator and section 2.3.3 contains information on how light beam irradiation can be determined by using a silicon detector.

### 2.3.1 Concept of quantum efficiency

The number of charge carriers separated by a solar cell is not only dependent on the irradiation intensity, but also on the wavelength of the incident light. This means that a solar cell generates a different amount of electrons per photon depending on the photons wavelength which corresponds to the photons energy according to  $E = \frac{hc}{\lambda}$ . To quantify this behavior, a cell's quantum efficiency is defined as the ratio of the number of charge carriers produced by the solar cell to the number of photons of a given energy incident on the solar cell [35] which leads to the following formula:

$$QE(\lambda) := \frac{\frac{\text{electrons}}{\text{sec}}}{\frac{\text{photons}}{\text{sec}}(\lambda)} \quad (2.22)$$

There are two different quantum efficiency:

**internal QE (IQE)** is the ratio between separated electrons and photons absorbed by the cell.

**external QE (EQE)** is the ratio between separated electrons and photons that hit the solar cell

This means that the EQE also includes optical losses such as transmission and reflection whereas the IQE only considers internal losses like recombination.

An ideal solar cell would transform every incoming photon into one electron and therefore would have a rectangular shape in a QE- $\lambda$ -diagram like 2.4.

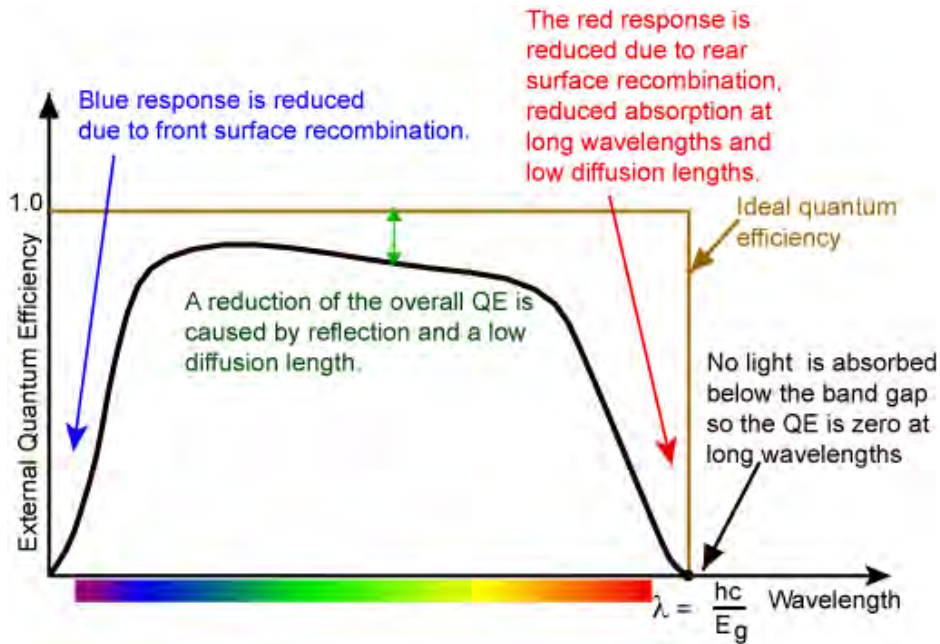


Figure 2.4: The quantum efficiency of a solar cell. The green arrow indicates the difference from ideal and real QE. Taken from [35]

The QE is highly material dependent. The main difference is the band gap cut-off as can be seen in figure 2.5. c-Si cells have a very broad response due to a band gap of around 1.1 eV corresponding to light of 1100 nm. GaAs has a band gap of around 1.42 eV. While mc-Si has the lowest QE, a-Si and DSSC (Dye sensitized solar cells) have quite similar QE-curves. An example of a CIGS cells QE can be seen in figure 3.12.

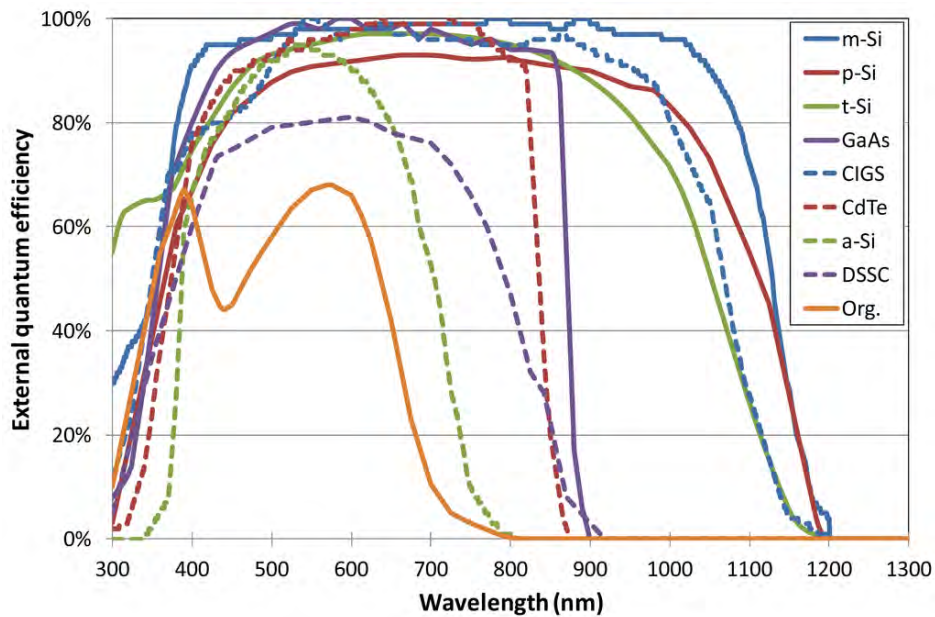


Figure 2.5: Comparison of typical QE-curves of solar cells of different materials.

The  $I_{SC}$  can be derived from the EQE data as follows:

$$I_{SC} = \int E(\lambda) SR(\lambda) d\lambda = \int E(\lambda) \frac{q\lambda}{hc} QE(\lambda) d\lambda \quad (2.23)$$

where  $E(\lambda)$  is the spectral irradiance distribution,  $S$  is the spectral response corresponding to QE according to  $SR = \frac{q\lambda}{hc} QE(\lambda)$ .

### 2.3.2 Monochromator

“A monochromator is an optical device that transmits a mechanically selectable narrow band of wavelengths of light or other radiation chosen from a wider range of wavelengths available at the input.” [36]

A monochromator can either be realized by using the optical phenomenon of optical dispersion in a prism, or by using a diffraction grating, making use of optical interference. A diffraction grating can be either transmissive or reflective, however, in monochromators the reflective type is more common, due to space issues. A grating is made of several slits, ideally with the same width and the same spacing  $d$ . Due to additive and destructive interference of the light after interaction with the grating, the light of every wavelength is diffracted to different, wavelength dependent directions (having several maxima and minima). The wavelength maxima can be calculated by

$$\theta_m = \arcsin\left(\frac{m\lambda}{d} - \sin \theta_i\right). \quad (2.24)$$

In this equation  $\theta_i$  is the angle between the diffracted ray and the grating's normal vector,  $\lambda$  is the wavelength of the exiting light,  $m$  is the number of the maximum of the wavelength  $\lambda$  and  $\theta_m$  the angle at which the  $m^{th}$  maximum of the wavelength  $\lambda$  is found.  $\theta_i$  is the arbitrary angle of the incident light beam from the grating's normal vector.

In order to get the wavelength dependent beams focused on a measuring spot, a Czerny-Turner monochromator can be used. It focuses the incident light beam (A) onto the diffraction grating (D) with a curved mirror (C), from where the light is diffracted onto another mirror (D), that focuses the beam on the exit slit (F). The diffraction grating can be turned as indicated to focus beams of different wavelength on the exit slit (see figure 2.6).

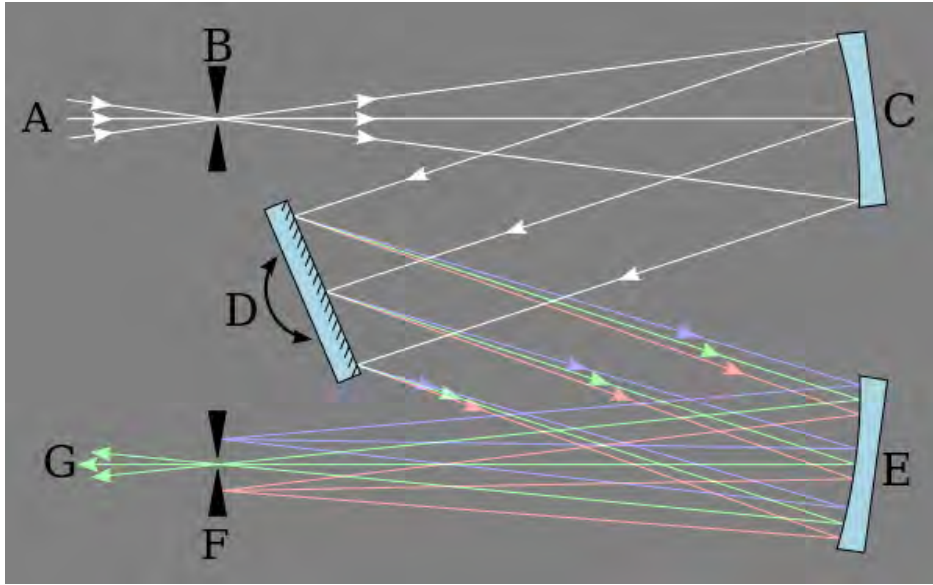


Figure 2.6: Scheme of a Czerny-Turner Monochromator. See text for closer description.  
Picture taken from [37]

### 2.3.3 Calibration by a semiconductor detector

In order to calculate the EQE by equation (2.22) the number of incident photons has to be known. Instead of calculating it from the emittance spectrum of the lamp and the transmittance of the monochromator it is easier and also more precise to detect the number of incident photons at the measuring position by placing a photon detector there. By running through all wavelengths with the monochromator and detecting the number of photons with a photon detector. For this purpose a semiconductor detector can be used.

The semiconductor detector consists of a semiconductive bulk placed between two electrodes. Incident radiation creates electron hole pairs in the semiconductor, as it does in solar cells. By an external electric field, these charge carriers are drawn from the semiconductor to the electrodes where they are collected and then measured by an Ammeter or Voltmeter.

The number of charge carrier pairs does not depend on the energy of the incident photons, except when they have lower energies than the band gap of the semiconductive detection material, leading to no detection. Above the band gap energy, every incident photon creates only one electron (the surplus energy is absorbed by the material by thermal relaxation). This means that the intensity of the incident radiation can be determined from the number of charge carriers.

For EQE, the wavelength dependent irradiance of the setup measured by the semiconductor detector is saved and later combined with the measurement of charge carriers collected by the sample cell to calculate the EQE.

## 2.4 Colored Light Soaking of CIGS-cells

Light soaking is the illumination of a photovoltaic device over a certain time. The IV-curves of most light soaked thin film devices show significant changes over time as can be seen in figure 2.7(a). To get an overview over these changes over time, the characteristics as  $V_{OC}$ ,  $I_{SC}$ ,  $P_{MPP}$  and FF indicators are followed over time. Plotting each of them over the time they have been measured leads to diagrams as in figure 2.7(b). Please note, that the time axis in figure 2.7(b) is logarithmic.

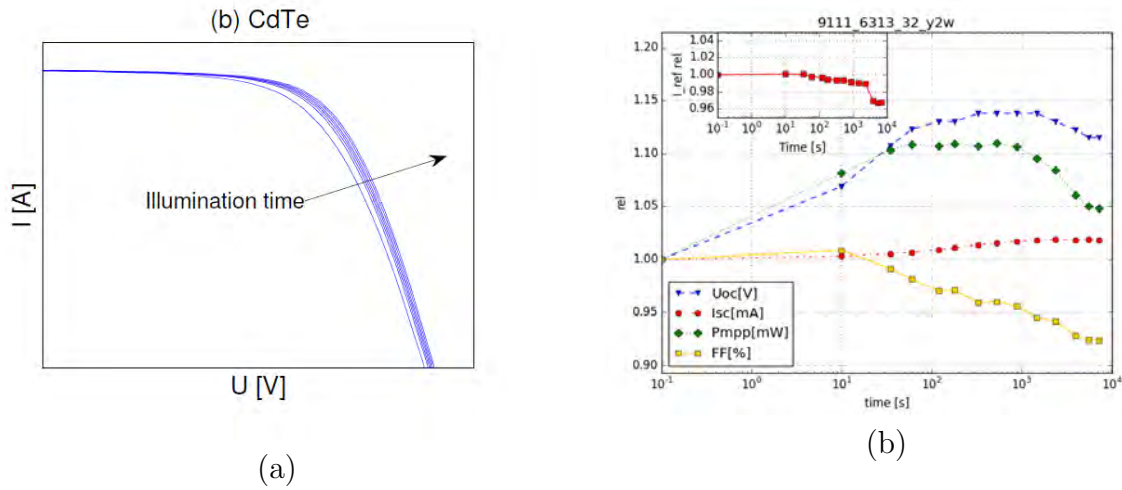


Figure 2.7: Development of the IV-curves of a CdTe/CIGS cell under light soaking (a) and change in  $V_{OC}$ ,  $I_{SC}$ ,  $P_{MPP}$  and FF as a function of time (b).

### 2.4.1 IV-curve Anomalies of CIGS cells

When making IV-curve measurements of crystalline cells, the results look similar to figure 3.8. CIGS cells however, often show very different IV-curves, due to internal properties as will be explained in this chapter. There are anomalies from the IV-curve shown in figure 3.8 that occur at simple IV-curve measurements and anomalies that occur only under longer illumination (metastable light soaking effects). Sometimes, the initial anomalies disappear in the light soaked state.

#### Initial anomalies

All initial anomalies described here are described in more detail in [17].

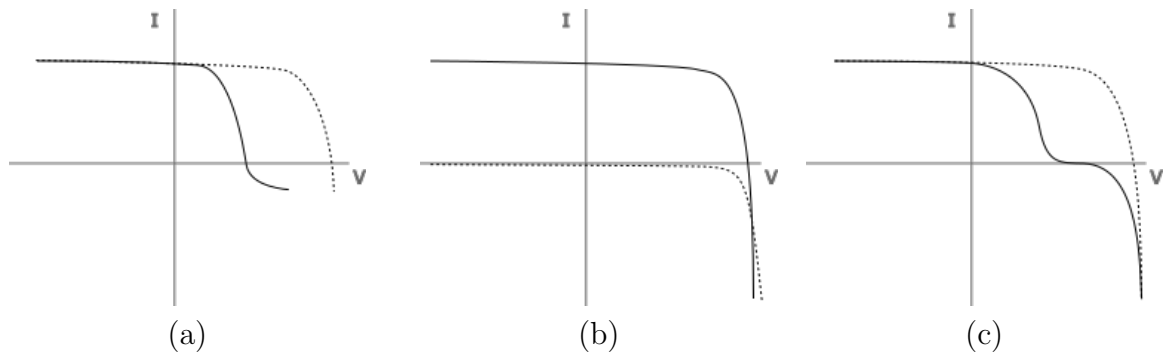


Figure 2.8: Initial anomalies of IV-curves of CIGS solar cells. Roll over (a), Cross over (b) and kink (c). See text for descriptions.

### Roll over effect

The IV-curve shows a saturation of the current at an electric forward bias. Possible reasons for this are a barrier at the back contact, acceptor states at the buffer/window interface, blocking the diode current or a positive conduction band offset at the buffer/window interface.

### Cross over effect

The dark and light IV-curve cross each other at forward bias. This can be caused by electron barriers in the conduction band, which is reduced when photodoped, thus increasing the diode current. The electron barrier can also be caused by a high density of acceptors in the absorber close to the interface leading to a high negative charge in this area. Under illumination, the acceptors are filled with holes, thus reducing the electron barrier. The cross over can also be caused by a minority carrier recombination at the back contact junction.

### Kink in light IV-curve

Kinks in IV-curves look similar to roll overs, but have a current plateau at 0 A instead of reverse current. Such kinks are caused by positive conduction band offset at the absorber/buffer interface. This can occur jointly with low  $I_{SC}$  compared to EQE as discussed below. Another explanation for kinks is a thin p+ layer at the absorber front surface which can also lead to a low red response in QE.

### Discrepancies in $I_{SC}$ and EQE

As explained in more detail in section 2.3.1, the  $I_{SC}$  of a c-Si solar cell can be calculated from its EQE. However, in CIGS cells this formula doesn't apply. The  $I_{SC}$  measured under STC can be either higher or lower than the  $I_{SC}$  calculated via equation (2.23).

Higher  $I_{SC}$  under STC can be caused by a large number of micro shunts: As the cell is not completely illuminated at an EQE measurement, the non-illuminated parts act as a shunting load. When this shunting load is small due to a large number of micro shunts, the generated current is drained through the non-illuminated area, thus leading to a systematical error in the EQE measurement.

Lower  $I_{SC}$  is caused by a photo current barrier, increasing with the photo current. The low currents at EQE measurements can pass but higher currents at STC can not.

## Metastabilities in CIGS Solar Cells

Unlike silicon and III-V-type solar cells, most thin film solar cells show a light dependent change of  $V_{OC}$  and other characteristics. As first described by Ruberto and Rothwarf in 1987, the  $V_{OC}$  of CIS cells changes when illuminated with white light [38]. Since then lots of further measurements on this topic have been performed [4, 39, 40, 41] but still no satisfying understanding of all effects has been found.

In order to obtain reliable measurement data of metastable effects it is important to relax the measured device to a known state. This is done by storing the device in complete darkness at temperatures around 300K for around a day or at least over night [17, page 292]. It is difficult to test whether or not the device has reached it's relaxed state, because an IV-curve measurement would require illumination of the device what would change its status. Also a capacitance-voltage measurement would change the device's status because the metastabilities also respond to bias. The best practice to find whether or not a device is in the relaxed state is by measuring the device's IV-curve with a  $1000 \text{ W/m}^2$  flashed light with a duration of about 20 ms. There are light-dependent and bias-dependent effects [17].

### Light-dependent metastable effects

Red light is almost completely transmitted through the window and the buffer layer and absorbed in the absorber layer. This means that under red light illumination, the absorber layer is the active layer and therefore the occurring effects are absorber driven. One effect is an increase in lateral conductivity of the CIGS film over a time of hours. After illumination a persistent photoconductivity remains [41]. It has been found, that this is due to an increase of the hole density in the absorber [42]. The impact of this microscopic effect on macroscopic characteristics like the  $V_{OC}$  depends on the limiting effect of the cell: When limited by recombination in the space charge region (SCR) or the quasi neutral region (QNR), the  $V_{OC}$  increases with increasing hole density. If the limit is recombination at the absorber/buffer interface, cells with fermi level pinning show a decreasing  $V_{OC}$  with increasing hole density, in cells without fermi pinning  $V_{OC}$  remains constant. Increasing  $V_{OC}$  under red light illumination is explained by reduced recombination in the absorber [43].

Blue light is absorbed mainly in the window and the buffer layer and leads to an increased fill factor [44]. The effect is reduced at low temperatures. Blue light illumination reduces kinks in IV-curves, an anomaly often occurring in CIGS IV-curve measurements (see section 2.4.1). The blue photon flux in a AM1.5 spectrum is sufficient to cause the blue light effect. Therefore illumination under white light leads to combinations of the red light and the blue light effect.

The blue light effect can also be resembled by electron irradiance.

### Bias-dependent metastable effects

Metastable effects can also be observed when stressing a CIGS solar cell with bias. When applying forward bias similar effects to the red light effects are observed. The hole density in the absorber increases leading to a change in  $V_{OC}$  as described in the red light effect. Like the red light effect the forward bias effect can also be annealed at temperatures around 300K.

The reverse bias effect occurs, when a cell is put under -1V bias for at least one

hour and leads to a decrease in the fill factor [45]. This can be a problem for partially shaded cells and modules.

### Causes for metastable effects

All these metastable effects are caused by defects in the material. Either defects are created by the illumination or existing defects create trap states, binding electrons and holes for some time. The red light, the blue light and the reverse bias effect can be explained by assuming metastable  $(V_{Se} - V_{Cu})$  complexes [5].

Deep in the absorber these complexes are mostly in a  $(V_{Se} - V_{Cu})^+$  configuration. When free electrons are brought to this area, as is done by red light illumination and forward bias, the  $(V_{Se} - V_{Cu})^+$  complexes transform to  $(V_{Se} - V_{Cu})^-$ , releasing holes and thereby changing the cell's characteristics as described above. In the absorber, the  $(V_{Se} - V_{Cu})^-$  configuration is not stable and therefore relaxes to the  $(V_{Se} - V_{Cu})^+$  configuration when the illumination or the external bias stop.

The same complexes exist close to the heterointerface, but there they are stable in the  $(V_{Se} - V_{Cu})^-$  configuration. This is due to the different position of the fermi level than deep in the absorber, caused by the electrons from the emitter. Reverse bias increases the negative charge of this region and  $(V_{Se} - V_{Cu})^{2-}$  complexes are formed. Blue light on the opposite provides holes, leading to  $(V_{Se} - V_{Cu})^+$  complexes, that are metastable in this region.

Positively charged  $(V_{Se} - V_{Cu})$  vacancy complexes act as donors and negatively charged  $(V_{Se} - V_{Cu})$  vacancy complexes act as acceptors. This leads to a change in the charge carrier densities  $n$  and  $p$ . Depending on the position of these metastable donors and acceptors, they change the equilibrium of electrons and holes in the p-type and n-type material and thereby change  $V_{OC}$  according to equations (2.15) and (2.17). An overview of the qualitative effects of changes in  $n$  and  $p$  in the different material types is given in table 2.4.

		$\Delta$		
$n_p$	$p_n$	$n_n$	$p_p$	$V_{OC}$
+	0	0	-	-
-	0	0	+	+
0	+	-	0	-
0	-	+	0	+

Table 2.4: Qualitative change in  $V_{OC}$  when  $n_p$  or  $p_n$  are increased or decreased according to equations (2.15) and (2.17).  $n_p$  and  $n_n$  are the electron densities in the p-type and n-type material respectively,  $p_n$  and  $p_p$  are the hole densities in the n-type and p-type material respectively.

### 2.4.2 Dependencies of metastable light soaking effects

The metastable effects described above are not only color and bias dependent. For example they also depend on the temperature, as the red light effect is annealed at temperatures above 50 °C. Therefore it is important to keep the temperature stable and below 50 °C.



The metastable effects are furthermore depending on the bias applied during the light soaking process, as is described in [2]. Holding the cell at open circuit causes the highest metastable light soaking effect, whereas holding it at  $P_{MPP}$  leads to smaller effects and holding it at short circuit to the smallest effects.

As light soaking effects depend upon photons and electrons brought into the device from outside, the magnitude and the speed of the light soaking effects also depend on the irradiance and the magnitude of bias applied respectively. This shows again, that stability of irradiance and bias is important.

One further important parameter for the light soaking effects is the device's material itself. Light soaking effects are caused by  $(V_{Se} - V_{Cu})$  complexes and other material defects, making it clear that different defects cause different effects. Therefore the material should be as similar as possible when different cells are compared regarding other parameters. Not only the absorber layer affects the light soaking measurements but also the buffer layer (and window layer). Some buffer layers have shown no light soaking effects [17, page 271], also depending on the deposition method.

### 2.4.3 Light spectrum

Light is electromagnetic radiation within a certain interval of wavelengths. The visible light is the electromagnetic radiation with wavelengths from 390 to 780 (750) nm. Often the term light also includes parts of the UV and the infrared radiation. In this thesis light refers to electromagnetic radiation with wavelengths from 350 (near UV) to 1100 nm (near infrared) because the quantum efficiency of CIGS cells has significant values within this range. Therefore the filters used for the light soaking experiments performed in this work have transmission peaks within this range and were called after the wavelength-regime at which they are located.

Light consists of elementary particles, called photons. The wavelength and the energy of a photon correlate according to

$$E = h\nu = \frac{hc}{\lambda} \quad (2.25)$$

where  $h$  is the Planck constant and  $c$  the speed of light. Thus, the photon's energy can be calculated from their wavelength (see table 2.5).

Color	wavelength [nm]	energy [eV]
(UV)	350	3.54
Blue	450	2.76
Green	550	2.25
Red	750	1.65
(infrared)	1100	1.13

Table 2.5: Some wavelengths of light and the corresponding energy.

### Solar Spectrum

The irradiation from the sun reaching the earth's surface depends on several parameters, mainly the sun's position in the sky and the weather. It has great impact on the

performance of photovoltaic devices. In order to get comparable measuring results, the “AM1.5”-spectrum has been defined (see figure 2.9).

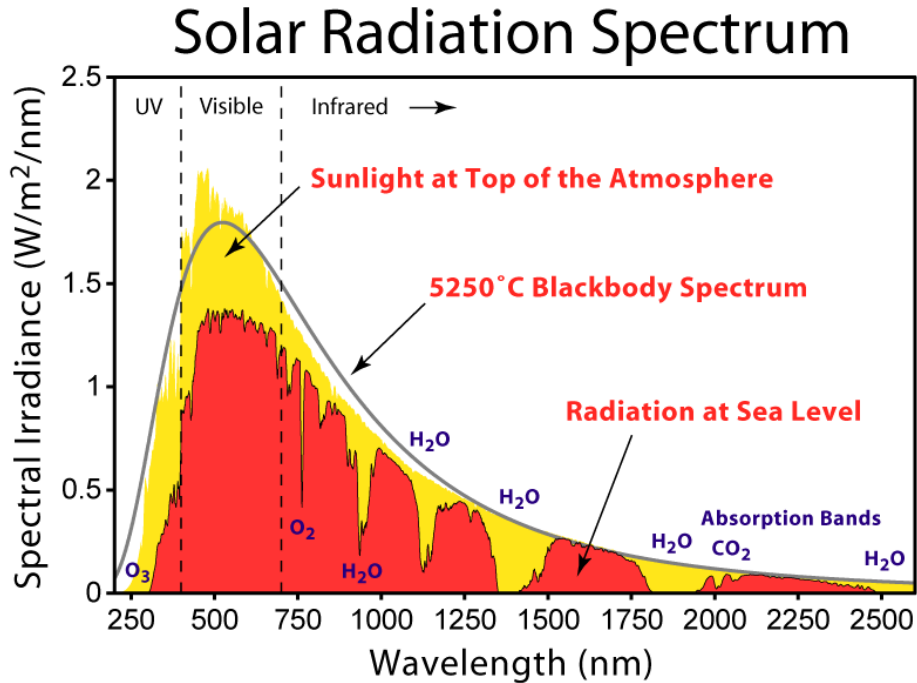


Figure 2.9: Solar Spectrum AM1.5

### Colored Light

As mentioned above, light consists of photons of different wavelengths. The human eye and brain interpret the different wavelengths of the visible light as colors as can be seen in figure 2.10.

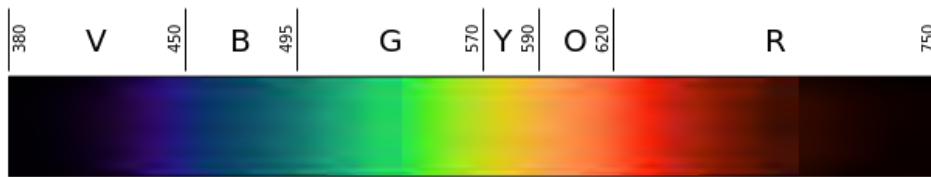


Figure 2.10: Colors and wavelengths of the visible light.

One can easily create colored light by filtering wavelengths from the sun’s spectrum or any other white light. An example of a spectrum of colored light is given in figure 2.11. Such spectra can be achieved by filters that only transmit certain wavelengths of incoming light. For example a green filter only transmits light with wavelengths of around 540 nm (green light). Depending on the purpose of the filter the maximum transmission and the band width can be varied. One very important characteristic of the spectrum of such filters is their quality factor (Q factor). It is a measure for the steepness of the spectra distribution at the cut-off wavelength. The cut-off wavelength is the wavelength at which the filters transmission factor is only  $\frac{1}{e}$  times the one from

the maximally transmitted wavelength (Instead of  $\frac{1}{e}$  also different factors like  $\frac{1}{2}$  or  $\frac{1}{\sqrt{2}}$  are used).

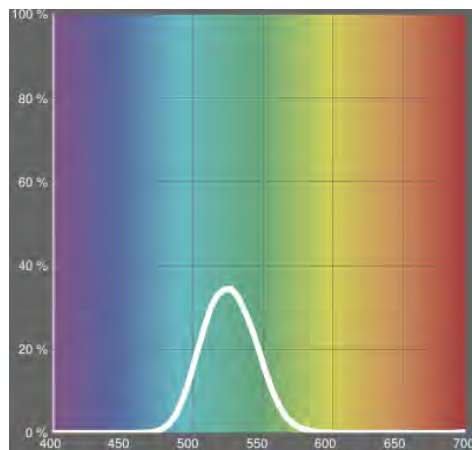


Figure 2.11: Transmittance of a green filter in the visible light range.

## 3 Methods

To obtain reliable and reproducible data on the light soaking of CIGS cells with different quality a lot of different measurements have to be performed. First the CIGS cells have to be characterized in order to find cells with good and poor quality. This was done by current-voltage (IV) measurements which have to be conducted under standard testing conditions (25 °C, 1000 W/m<sup>2</sup> irradiance, AM1.5 spectrum) as explained in section 2.2.3 and measuring the external quantum efficiency (EQE). The measurement setup is explained in section 3.1 for IV-curves and in section 3.2.1 for EQE measurements. The realization of the light soaking experiments is summed up in section 3.3.

### 3.1 IV-Curve Measurements

As explained in chapter 2.2, IV-curves give a lot of information on a solar cell's quality and performance. All the most important electrical properties like  $V_{OC}$ ,  $I_{SC}$ , FF,  $P_{MPP}$  and  $\eta$  can be determined from an IV-curve. For this thesis, IV curve measurements have been used to classify the solar cells at hand according to their quality and to thereby chose the specimen described in section 4.1 from the large number of solar cells available.

This chapter describes the setup of the IV-curve measurements, the results and the error analysis of these characterization measurements.

#### 3.1.1 IV-curve Setup

The IV-curve measurements have been performed with a sun sulfur lamp built by a company called Solaronix (see figure 3.1). In order to keep the cells at a temperature close to 25 °, the cells are water cooled by a water pump. To monitor the temperature changes on the cells surface and the reference cell, several temperature sensors of the type PT100 have been installed (see figure 3.2). The cells are contacted by four pins to achieve four point measurement. The IV-curve itself is measured by a Keithley 2602A SYSTEM Sourcemeter driven by Keithley TSP Express Software. The Keithley also tracks the reference cells  $I_{SC}$  in order to correct fluctuations of the lamp due to power grid frequency and power grid disturbances.

#### Sun Simulator Lamp

The sun simulator lamp is a sulfur lamp focused by a mirror. The focus is not very good and therefore a lot of diffuse light is produced which is reflected by the diffuse reflecting walls of the container (grey box in figure 3.1) to reach the required 1000 W/m<sup>2</sup>.

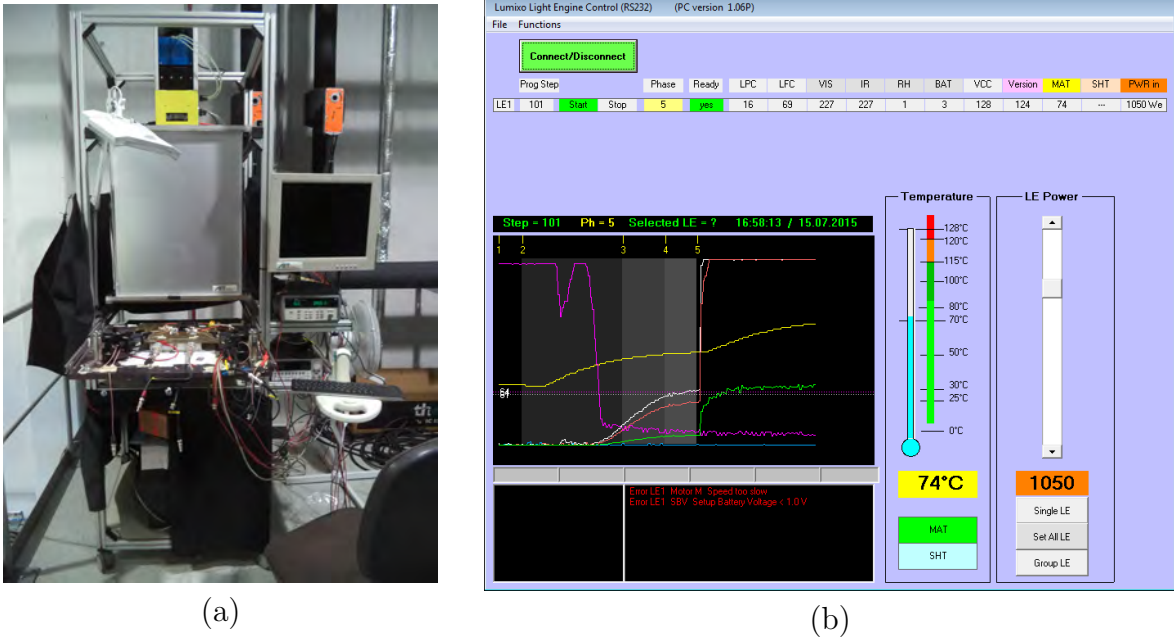


Figure 3.1: Sun simulator lamp: (a) Picture of the used sun simulator lamp (yellow box at top) with focusing device and a screen shot of the Solaronix lamp control Software (b)

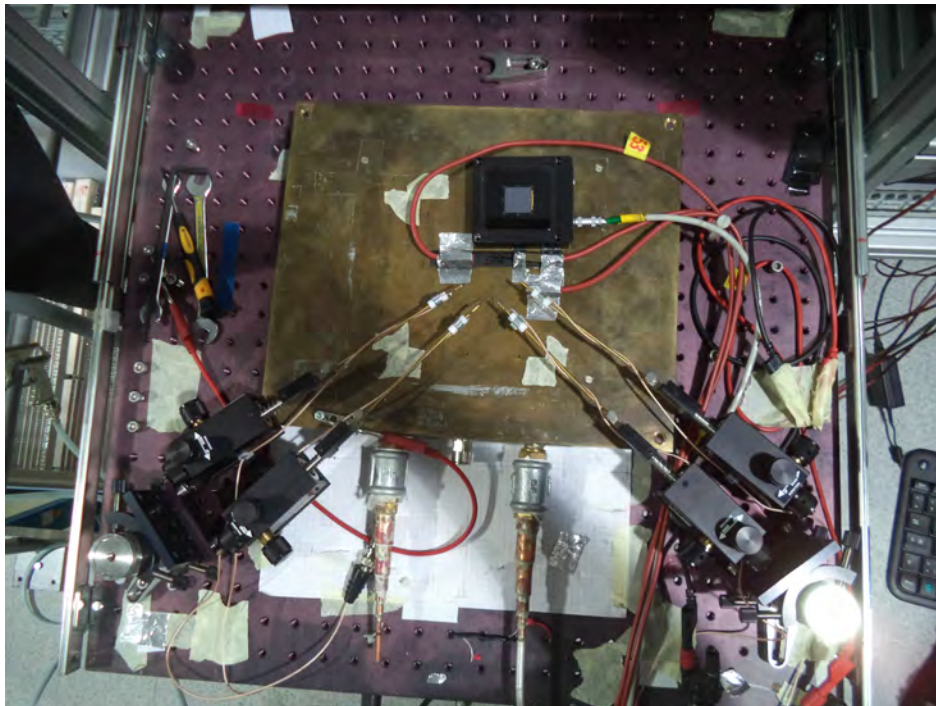


Figure 3.2: Setup of the IV-curve measurement

device	opening angle	irradiance [W/m <sup>2</sup> ]	relative irradiance [%]
Pyranometer	90°	1064.3	106.0
c-Si reference cell	90°	1004.5	100.0
	48°	465.3	46.3
	32°	217.5	21.7
	6°	11.1	10.2

Table 3.1: The proportion of diffuse light of the sun simulators incident beam has been measured with a pyranometer and a crystalline silicon reference cell. Tubes of different height and width were put in front of the reference cell in order to obtain different opening angles (measured from the reference cell’s surface’s normal vector). The resulting irradiances are given.

The irradiance has been measured with both a reference solar cell and a pyranometer. The latter has an almost angle-independent absorption for all light coming from above, whereas the reference cell reflects a lot of the diffuse light coming from the sides. Therefore the comparison of their measured irradiance also gives an idea of the diffuse light distribution (see table 3.1). The reference solar cell reflects approximately 6% of the incident light.

Also, the reference cell was shaded to measure the proportion of light absorbed by the cell from different opening angles. table 3.1 sums up the results, giving an idea of the diffuse light distribution.

This relatively high proportion of diffuse light leads to several problems. First of all, for real STC-conditions the incident beam has to be parallel light. Non-parallel irradiance brings up the problem, that solar cells have an angle-dependent absorption coefficient. This could be corrected by adjusting the lamp power until the reference cell gives the same  $I_{SC}$  output as it would give under STC illumination. When the measured cell and the reference cell have a similar angle-dependent absorption coefficient, the measured cell would then also give output according to STC illumination. The cells measured in this thesis are not encapsulated and have no anti-reflective layer, so they can’t be compared to the glass encapsulated reference cell with anti-reflective layer.

Another way to get conditions close to STC is by measuring the EQE of a cell and the spectral irradiance of the lamp. By combining them via the formula (2.23), one can find the cell’s  $I_{SC}$  at STC. By then adjusting the lamp power until an IV-curve measurement reaches the calculated  $I_{SC}$ , one can find an irradiance that is similar to STC, although having diffuse light.

This method works fine with crystalline silicon solar cells, but in CIGS cells, there are effects, that lead to discrepancies between  $I_{SC}$  at STC and the  $I_{SC}$  calculated via EQE and the lamp’s spectral irradiance. As described in [17] there are several possibilities: this can be due to photo current barriers for relatively high currents close to  $I_{SC}$ , leading to a decreased  $I_{SC}$ , because there are only currents far lower than  $I_{SC}$  at the EQE-measurement.

These effects mean, that no conclusion over the cell’s absolute  $I_{SC}$  could be drawn. But for this thesis it is enough to compare the cells when measured under the same conditions, which can be provided by the measurement setup.

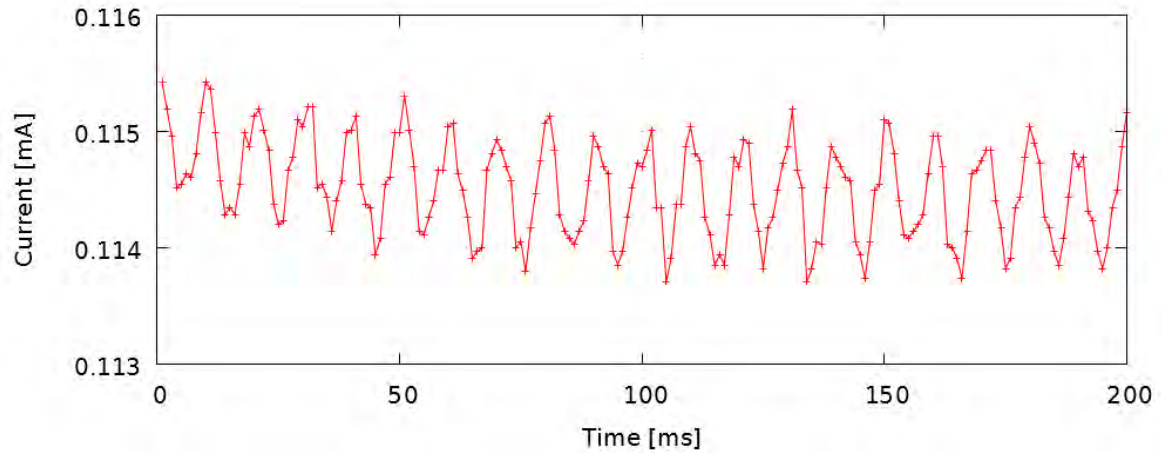


Figure 3.3:  $I_{SC}$  from the reference cell during one IV-curve measurement

### Reference Cell

The lamp used for the illumination of the cells has fluctuations caused by non perfect conversion from the AC power from the grid to DC power that the lamp needs. To measure these instabilities, a reference cell is mounted onto the chuck and connected to the Keithley measuring instrument, which tracks the  $I_{SC}$  of the reference cell parallel to each IV-curve measurement. A plot of the reference cell's  $I_{SC}$  output can be seen in figure 3.3. Equation (2.16) shows that the  $I_{SC}$  of a cell linearly corresponds to the irradiance  $G$ . Thus, the  $I_{SC}$  of the reference cell is a measure for the relative change of the irradiance and can be used to correct the IV-curve of the CIGS cell. This correction has been done for every IV-curve by a Python script and the effect of the correction can be seen in figure 3.4.

The short term temporal instability can be calculated from the reference cell's  $I_{SC}$  according to equation (2.21), leading to values below 1%. Because of the correction via the reference cell the setup can still be considered an A class solar simulator.

It is interesting that the irradiance fluctuations have a frequency of 100 Hz, which is twice the power grid frequency. This is caused by an integrated rectifier which converts both polarities to one polarity, thus doubling the frequency of maxima and minima.

The reference cell can also be used to correct long term shifts in the lamps power output during light soaking experiments, but then the temperature change has to be considered as explained in section 3.3.

### Temperature Control

As described in section 2.2 it is important to control the temperature in order to get reproducible measurement results. The temperature should be held at 25 °C (standard testing condition). To achieve this, a cooling platform (“chuck”) has been installed (yellowish metallic rectangle in figure 3.2). Inside is a pipe system through which water can be pumped to control the temperature of the chuck and the mounted cells. When measuring solar cell's with electric contacts at the back, it has to be considered that the chuck is out of metal and has to be insulated from the cell's contacts. For the measurements of this thesis a water pump has been used. The temperatures of the

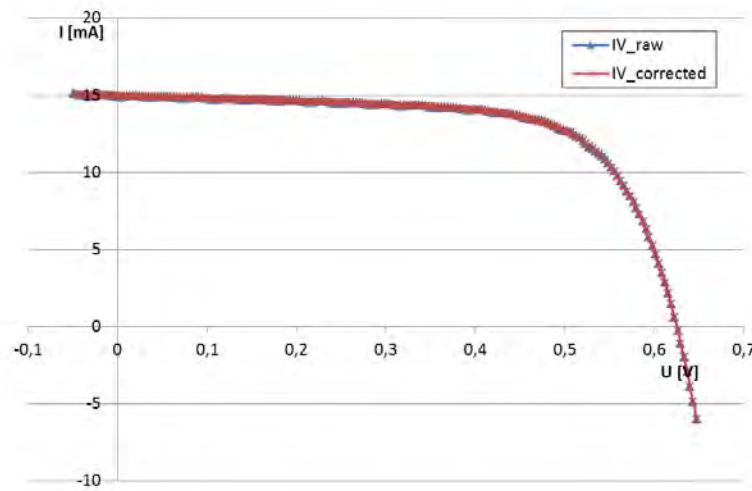


Figure 3.4: Correction of fluctuations in the IV-curve caused by instabilities of the lamp by considering the current measured by the reference cell.

water can be chosen in steps of  $1^\circ\text{C}$ .

In order to monitor the temperature of a mounted solar cell, several temperature sensors have been installed and monitored by an Agilent data logger. Due to the fact, that the temperature sensors can't be installed on the measured cell's surface, where it would deliver the most accurate data, temperature sensors have been placed at several spots. One directly on the chuck's surface which would show quite different temperatures than there would be on the cell's surface. Therefore a piece of glass, left over from the manufacturing process of the solar cells, was mounted onto the chuck just like the measured cell. The glass, having the same layers on top like the measured solar cells, has temperatures on its surface similar to that of the cell. Another problem with the temperature sensors used is that they shade the surface they are measuring (they couldn't be attached to the cell's back, because that would have a bad impact on the cooling behavior), thus influencing the glass's surface temperature. In order to be able to estimate this error, two sensors have been mounted onto the glass. One facing downwards and one facing upwards, directly into the incident light. Though this still gives no absolute values or reliable upper and lower limits to the cell's surface temperature, the combined sensors give a good idea, whether or not a thermal equilibrium is reached. In this way the measured data can be corrected relatively to each other, thus giving a much better comparison of the relative cell quality, which is the main purpose of the IV-curve measurements for this work. Furthermore the reference cell's temperature and the room temperature around the measurement setup have been tracked.

How the temperature changes with sudden changes in illumination can be seen in figure 3.5 and in figure 3.21. figure 3.5 shows some interesting facts about the temperature development. First, the sensor facing up measures lower temperatures than the one facing down. This means, that the glass with photovoltaic layers absorbs the incident light much better than the sensors surface and then quickly transfers the heat to the sensor. This transfer takes less than two seconds, as can be seen when comparing the starting and ending time of the steep inclines. This indicates, that the sensor



facing down measures the solar cell's surface temperature very well.

#### Characterization of Low Light Behavior of CIGS Cells

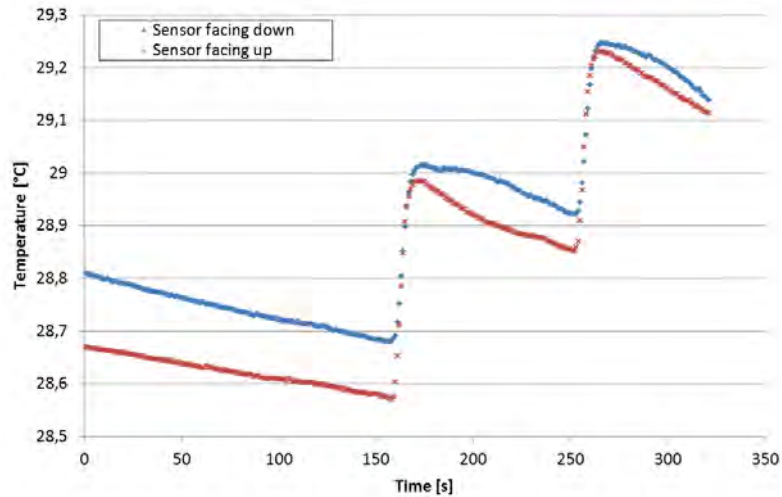


Figure 3.5: Temperature development from two sensors placed upon a glass, under illumination of  $1000 \text{ W/m}^2$  (first plateau),  $1050 \text{ W/m}^2$  (second plateau) and  $1100 \text{ W/m}^2$  (third plateau). One can see, that a change in illumination causes quick changes in temperature, thus making it important to measure the IV-curves right after setting the irradiance. After the initial incline, the temperature relaxes again towards a thermal equilibrium (never reached in this measurement) indicated by decreasing temperature after the temporal peaks.

Another interesting conclusion drawn from figure 3.5 is that a change in illumination has a very quick impact on the cell's temperature (steep incline within 15 seconds) but that the temperature is then decreasing again due to the water cooling, which needs much more time to reach equilibrium. The impact of these two effects with different time constants can also be seen very well in figure 3.21.

#### Contacting the Cell

The structure of the measured cells can be seen in figure 3.6. During the production process, the cells have been separated by removing all layers except the back contact, thus leaving dark lines around each cell. Each sample consists of a  $4 \times 8$  array of single cells. The back contacts are brought to the front around the array (thick metallic band on left and lower side in figure 3.6). On each cell there is a metallic structure. These are metal fingers to improve the collection of charge carriers at the front contact. The small rectangle can be used to easily connect to the front contact of the cell.

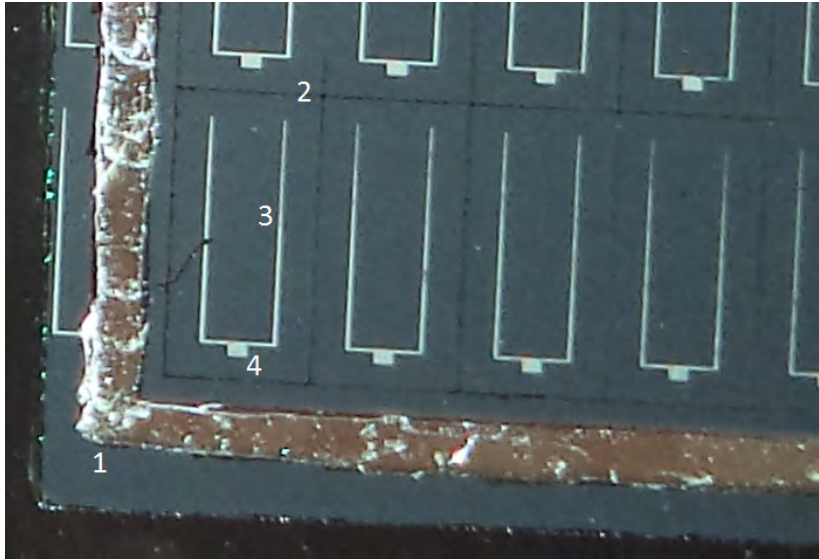


Figure 3.6: Structure of the measured CIGS cells. The broad metallic back contact can be seen on the left and lower side (1). Each rectangle surrounded by darker lines (2) is one cell. Along the dark lines all layers except the back contact have been removed to create the separated cells. The bright structures within each cell are the metal fingers (3) to collect the current and a little rectangle (4) to simplify front contacting.

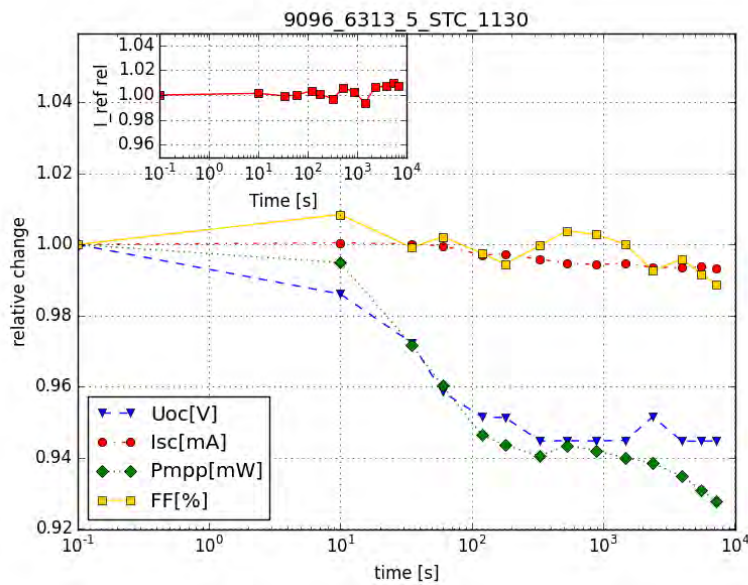


Figure 3.7: Light Soaking measurement under STC.

The cells have been contacted by pressing metal pins onto the contact surfaces with pin holders that could be moved along three axes. As described in section 2.2.2, it is important to use four-terminal sensing to obtain reliable IV-curve data. This has been realized by four separate pins, as can be seen in figure 3.2. Because of the heating of the pin holders by the 1000 W/m<sup>2</sup> irradiance and the resulting thermal expansion,

the pins sometimes lose contact and move over the cell with the danger of damaging it. To limit this effect to a minimum, an arch made of white paper was mounted over the pin holders to keep irradiation off them. With this method even light soaking measurements under STC were performed (see figure 3.7).

### 3.1.2 Accuracy of the Keithley Source Meter

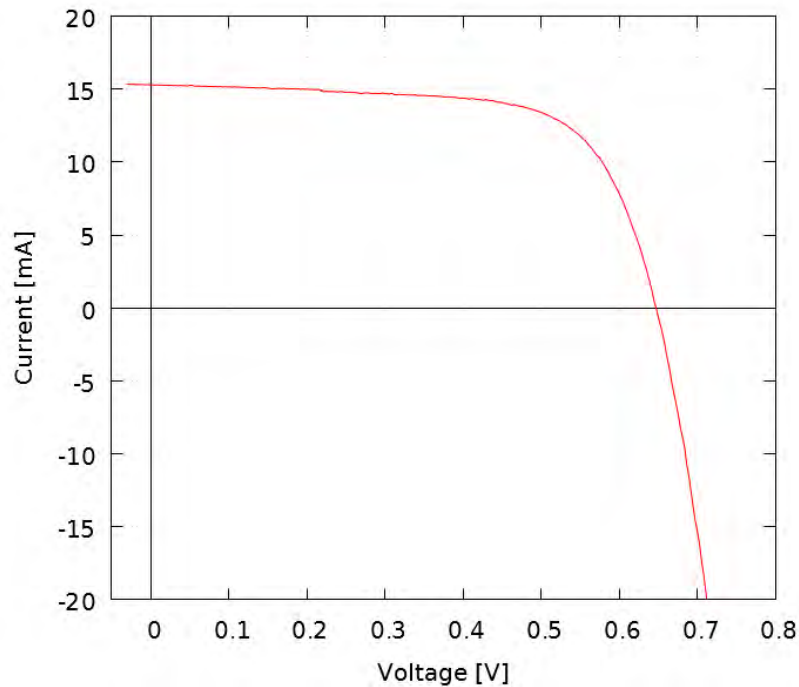


Figure 3.8: An example of the measured IV-curves.

Errors in measurement results can also be caused by the measuring device itself. Therefore it is important to know the device's specifications. There is an official specification sheet for the 2602A Source Meter from Keithley Instruments Inc. reporting an accuracy of 0.015 % for the voltage at the range of 1 V). The Accuracy for the used current ranges of 10 mA and 100 mA of 0.02 %. Due to higher currents at STC, two different ranges have been used for the current.

In figure 3.8 a measured IV-curve can be seen. It shows a slight kink and has lower  $I_{SC}$  than its EQE-measurement would suggest.

## 3.2 EQE Measurements

As explained in chapter 2.3, quantum efficiency measurements give information on a solar cell's wavelength dependent and overall performance. Furthermore the theoretical  $I_{SC}$  at standard testing conditions can be calculated from the EQE data. When this doesn't match the actual  $I_{SC}$  as it can happen for CIGS cells, there can still be conclusions drawn about the cell's characteristics as explained in section 2.4.1. Therefore EQE measurements are a good extension to IV-curve measurements for CIGS solar cell characterization.

Section 3.2.1 explains the setup used to measure the CIGS cells quantum efficiency and section 3.2.2 compares the EQE-curves measured from all cells and discusses the differences from calculated  $I_{SC}$  to the  $I_{SC}$  measured in the IV-curve measurements.

### 3.2.1 EQE Setup

For the EQE measurements the following components have been used (see figure 3.9):

- Newport 6332 quartz tungsten halogen lamp
- Newport 74010 filter wheel
- Newport 74125 monochromator
- Newport 70356\_70326 NS silicon detector
- Newport 70714 Light Bias Amplifier
- Newport 70104 Merlin radiometry system
- Newport TracQ software

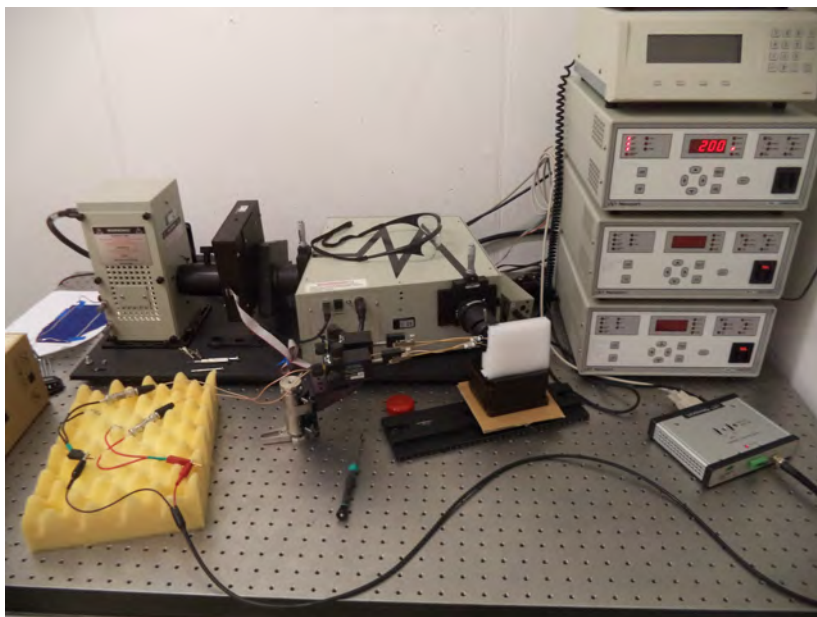


Figure 3.9: Setup of the EQE measurement.

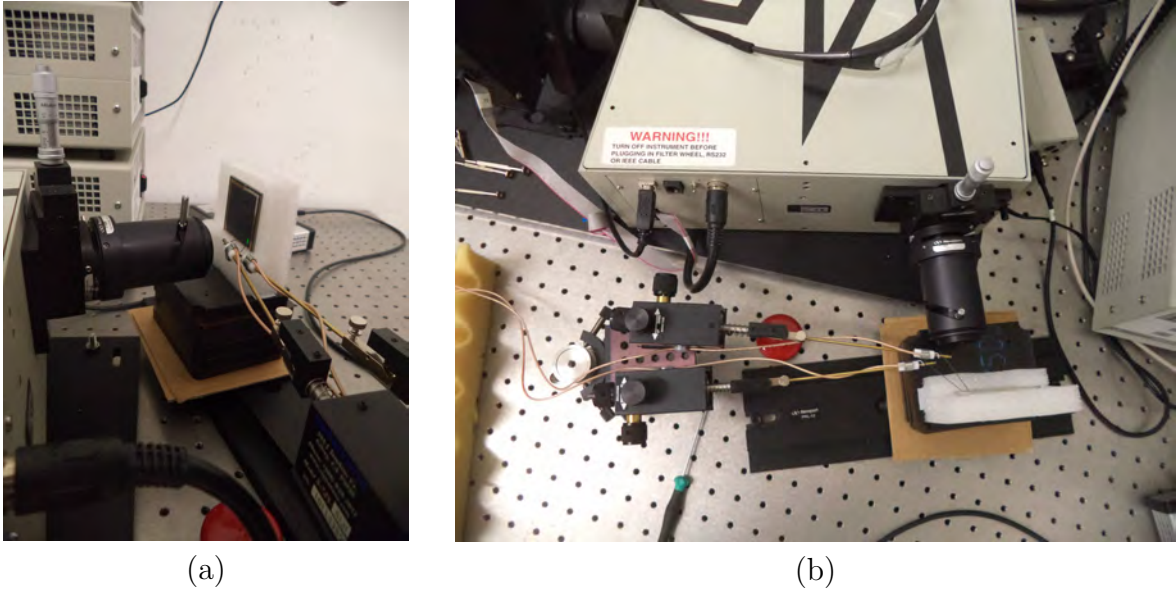


Figure 3.10: The two-point contacting of the cell for an EQE measurement from side (a) and top (b)

The light is emitted from a quartz tungsten halogen lamp. It then passes a filter wheel containing different filters. These filters help avoid higher order interferences in the monochromator, which is the next device. In the monochromator the photon's wavelength is chosen. In front of the output port of the monochromator either a silicon detector for calibration or a cell for measurement is mounted. While the silicon detector is directly connected to the digital lock-in radiometry system, the cell has to be contacted with two pins (see figure 3.10). In this case a two point measurement is sufficient because only short circuit measurements are done, therefore the voltage is known to be 0V. The current taken from the cell by the two pins is amplified by a light bias amplifier by a factor of  $10^5$  before it is measured by the digital lock-in radiometry system. The result is displayed on a computer with a software called TracQ. This software also enables the user to start automated EQE and calibration measurements.

In order to get information upon the reproducibility of this setup, a cell has been measured several times while removing and recontacting the pins every time. Between the first and the second measurement the cell has also been taken out of the holder completely and remounted. The results can be seen in figure 3.11 and in table 3.2.

	contact number		
	3	2	1
relative deviation of integrated EQE from contact 4	0.06%	0.63%	2.34%
relative deviation of maximum from contact 4	0.06%	0.59%	2.36%

Table 3.2: Differences in QE measurements after recontacting the cell. The graphs of the measurements can be seen in figure 3.11.

This means that the quality of the contacts is reproducible (changes of less than 0.65%). Measurement 1 on the other hand shows a difference of over 2%. This is probably due to a different orientation of the cell towards the light beam. Most likely the



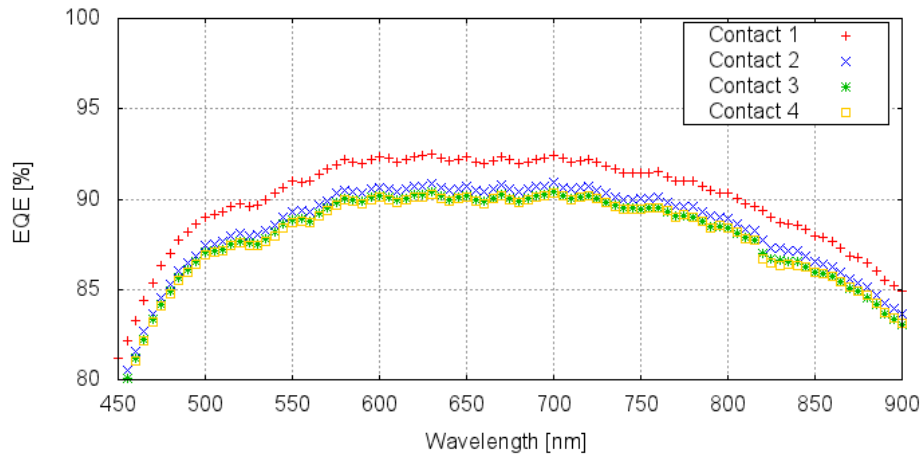


Figure 3.11: Repetition of the EQE measurement. After each measurement, the pins were recontacted. Additionally, the cell was taken out of the cell holder and mounted again after the first measurement.

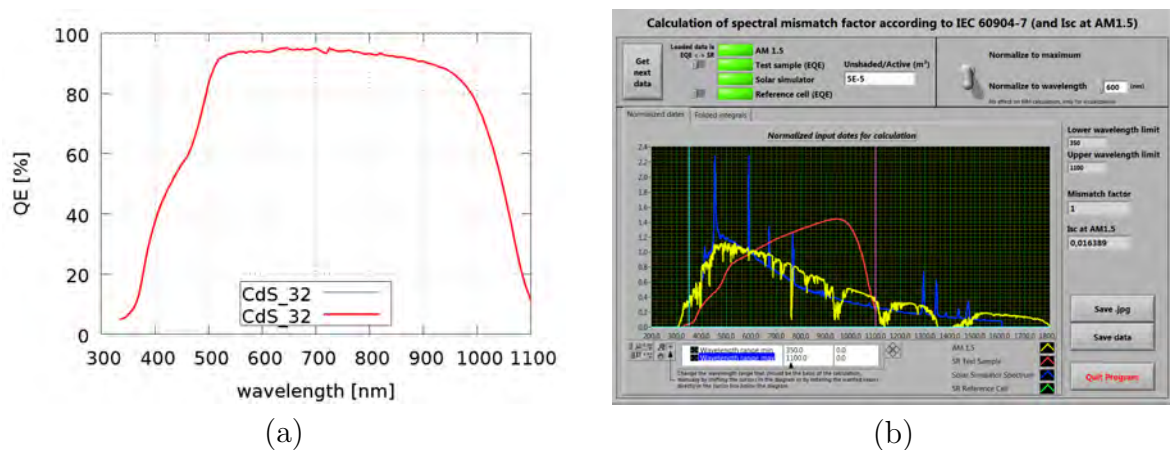


Figure 3.12: QE example and the GUI of the used spectral correction program

cell was not exactly orthogonal to the light beam after remounting it after measurement 1, causing a decrease in the current output.

The conclusion can be drawn, that the contacts with the pins are very reproducible and it is very important to take precise care of the cell's orientation in order to obtain comparable results. This also applies for the four point measurements of IV-curves.

### 3.2.2 Comparison CIGS

The EQE of the selected cells of the two samples of CIGS solar cells from Uppsala University with different buffer layers has been measured. The goal of these measurements was to gain information on the wavelength dependent performance of the cells, especially to compare the different buffer layers and to crosscheck the  $I_{SC}$  results from the IV-curve measurements.

### $I_{SC}$ comparison

With equation 2.23 the theoretical  $I_{SC}$  can be calculated from the EQE data. To do so, the EQE of the cell and the spectral distribution of the solar simulator have to be known. The EQE has been measured as described above, one example of the results is shown in figure 3.12(a) The spectral distribution of the solar simulator has been measured with an Ocean Optics spectrometer (*USB 2000+* (250-900nm) and *NIR Quest* (900-1700nm) combined by a Y fiber and a cosine corrector entrance optic). The calculations have been made with a non-commercial software called “spectral\_correction” (for screenshot see figure 3.12(b)).

As described in section 2.4.1 the  $I_{SC}$  calculated from the EQE measurement isn't always the same as the  $I_{SC}$  measured under STC conditions, especially not for CIGS cells. In table 3.3 these discrepancies can be seen.

Buffer Layer	Cell Number	$I_{SC}$		
		from IV [mA]	from EQE [mA]	$\frac{I_{SC(IV)}}{I_{SC(EQE)}} [\%]$
CdS	4	14.68	17.48	84.0
	8	14.66	16.07	91.2
	28	15.53	17.06	91.0
	32	15.67	17.49	89.6
Zn(O,S)	5	14.50	16.63	87.2
	17	15.67	16.47	95.1

Table 3.3: Comparison of the cell's  $I_{SC}$  measured by EQE and by an IV-curve measurement at STC.

### QE comparison

The plots of the cells' EQE can be seen in figure 3.13 and figure 3.14.

#### Cells with CdS buffer layer

The best cell according to the IV-curve measurement also has the highest EQE (cell number 32). Interesting enough, the worst cell (cell number 4) from IV-curve measurements also has a high EQE (as also reflected by the high  $I_{SC}$  calculated from EQE as can be seen in table 3.3). Cell number 8 has a lower EQE than cell number 28, but both below number 32 and 4. Although the results from the EQE are not the same as the values from the IV-curve measurements, the EQE measurements support the findings from the IV-curve measurements, as the relative results are similar. The reduced  $I_{SC}$  from the IV-curve measurements can be explained by photo current barriers as discussed in section 2.4.1, causing an  $I_{SC}$  reduction of roughly 10%. The cell number 4 has the highest difference between calculated and measured  $I_{SC}$  at STC. This matches the finding, that it has a poor over-all quality.

Nonetheless all CdS cells have quite high EQE values with maximums at 90-95%. They also have a wide plateau ranging from 500 nm to 950 nm.

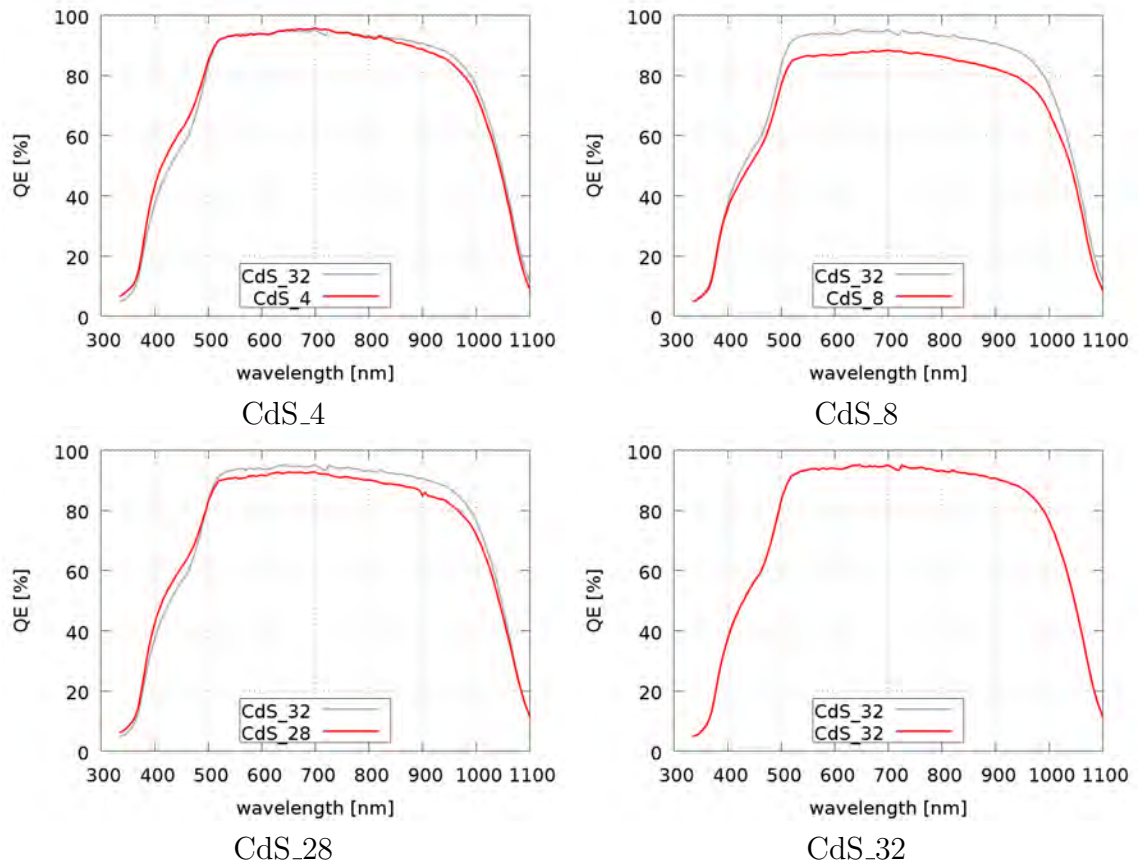


Figure 3.13: EQE-measurement curves of the CIGS solar cells with CdS buffer layer. The gray line indicates the EQE of the reference cell, in this case cell number 32.

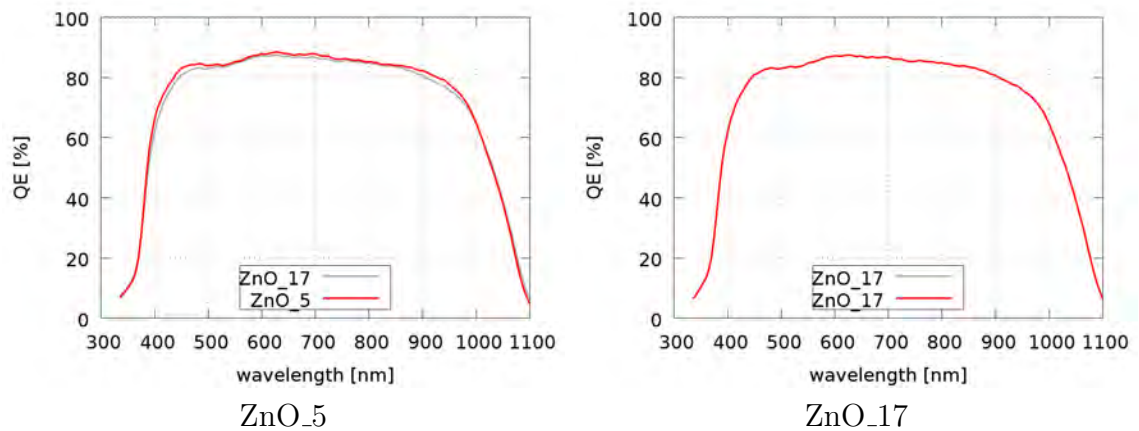


Figure 3.14: EQE-measurement curves of the CIGS solar cells with ZnO buffer layer. The gray line is the EQE of the referenced cell, in this case cell number 17.



### Cells with ZnO buffer layer

The cells with a ZnO buffer layer show similar results. They have a wide plateau of high EQE from 450 nm to 950 nm and their calculated  $I_{SC}$  from EQE is higher than  $I_{SC}$  measured at STC. Again this is most likely because of a photo current barrier and again the cell with lower quality (cell number 5) has a bigger difference than the higher quality cell.

### Comparison

When comparing the external quantum efficiencies of the cells with CdS buffer and the ones with ZnO buffer, the most obvious difference is the overall lower EQE of the ZnO cells. This is quite typical as production of CIGS cells with ZnO buffer layer is not as advanced and as well understood as CIGS cells with CdS buffer layer. The lower EQE corresponds with the lower  $I_{SC}$  at STC and the lower overall efficiency.

Another interesting aspect of the EQE measurements is that from around 400 to 500 nm the CIGS cells with ZnO buffer layer have a higher EQE than the cells with CdS buffer layer. This can be easily explained by the wavelength dependent absorption coefficient of the buffer layer materials. Whereas ZnO has an absorption coefficient of below 20 % from wavelengths of 350nm upwards [46], the absorption coefficient of CdS is above 20 % below wavelengths of 500nm [47]. This means that in cells with CdS buffer layer, less blue light is transmitted to the absorption layer, where it would have the highest contribution to the cell's performance.

### 3.3 Colored Light Soaking Measurements

In order to perform light soaking experiments on CIGS cells, the IV-curve measurement setup explained in section 3.1 was slightly modified. The irradiance was reduced and modified to approximately  $100 \text{ W/m}^2$  of different colors and a script for the Keithley source meter was written to automatically take IV-curve measurements in reasonable time intervals and keep the cell in open circuit bias in between.

#### 3.3.1 Duration and Time Intervals of the Light Soaking Experiments

Light soaking curves of CIGS cells have been found to follow a logarithmic development over time [40]. This means that the greatest part of changes in the parameters takes place in the early stages of the light soaking processes. The measured CIGS devices stabilize after around two hours of light soaking [40], thus being a reasonable duration for light soaking experiments. The parameter's development is logarithmically. This is because of the logarithmic development of the parameters, more measurements should be taken in the early stage of the light soaking process rather than in later stages. The waiting intervals between the IV-curve measurements were chosen to be approximately equidistant on a logarithmic time scale and to sum up to two hours total time. They are listed in table 3.4.

Figure 3.15 shows the same light soaking measurement plotted with linear and logarithmic time scale, showing that most of the change in the parameters occurs in the first part of the experiment.

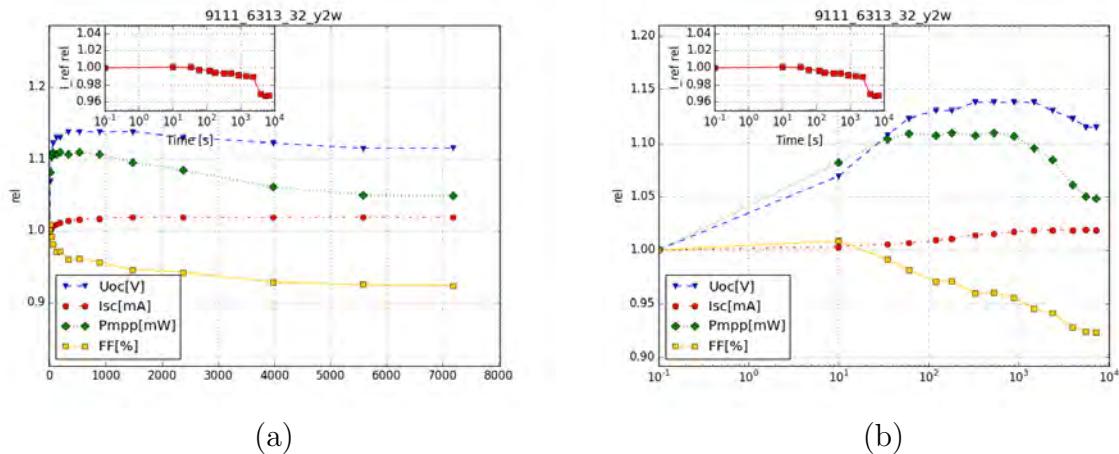


Figure 3.15: Two diagrams of the parameter curves from the same light soaking experiment, one with linear time scale (a) and one with logarithmic time scale (b). The linear curve shows that after two hours of light soaking saturation in all parameters is reached.

Intervals [s]												
10	25	25	60	60	150	220	350	600	900	1600	1600	1600

Table 3.4: Waiting intervals between consecutive IV-curve measurements during one light soaking experiment.

### 3.3.2 Reduced Irradiance

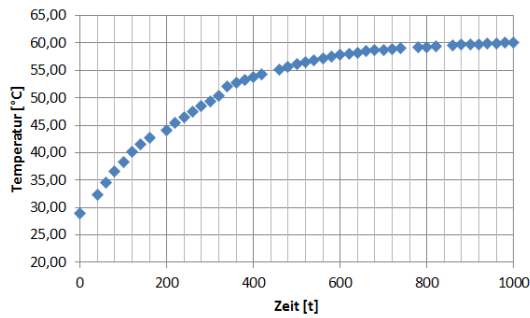
As explained in the introduction, the goal of this thesis is to measure light soaking processes under low irradiance light (around  $100 \text{ W/m}^2$ ). The lamp mounted on the IV-curve measurement setup delivers illumination irradiances in the range from 1000 to  $1300 \text{ W/m}^2$ . In order to reduce this irradiance to around  $100 \text{ W/m}^2$ , filters were placed between the lamp and the measuring plane. Tests have been made with different types and numbers of white printing paper filters while the transmitted irradiance was measured with a pyranometer. The results are shown in table 3.5 and suggest to use three sheets of paper and then slightly adapt the lamps power output.

type of paper	number of sheets	irradiance [ $\text{W/m}^2$ ]
$90 \text{ g/m}^2$	1	250.4
	2	135.0
	3	85.2
$80 \text{ g/m}^2$	1	338.3
	2	171.8
	3	103.6

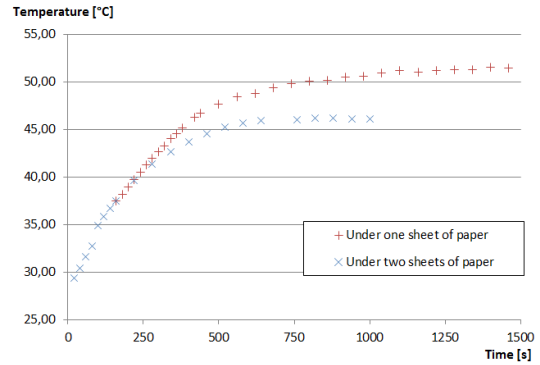
Table 3.5: Irradiance measured by a pyranometer under different types and numbers of paper sheets. The paper type is given in  $\text{g/m}^2$ , a typical measure for paper thickness. The lamp power was set to 1100, which would result in a  $1150 \text{ W/m}^2$  without paper filters.

Both types of paper (different thicknesses, given in  $\text{g/m}^2$ ) lead to acceptable results. The thinner paper has been chosen for the realization of the filter setup because it is larger (DINA3 format), thus providing a bigger measuring area fulfilling the uniformity classification “A” (see section 3.3.4). A filter holder was built to keep the filters in place during the measurements and to enable easy filter changes.

In order to avoid overheating of the filters and risk of autoignition, temperature measurements have been performed, showing that the temperature never exceeds the critical value of  $218 \text{ }^\circ\text{C}$  [48]. The temperature development is shown in figure 3.16 alongside that of a colored plastic filter, used to create colored light, under one and two sheets of paper. The temperatures stay far underneath critical values when reaching the thermal stable niveau ( $60.7 \text{ }^\circ\text{C}$  respectively  $51.5 \text{ }^\circ\text{C}$ ).



paper



plastic foil

Figure 3.16: Temperature development of paper and plastic foil under  $1000 \text{ W/m}^2$  illumination

The filter holder holds filters on top and additional filters mounted on a cardboard can be quickly inserted and removed, thus making it easy to prepare light soaking measurements with different colors and also different irradiances. Due to reasons explained in section 3.3.3, two sheets of white paper with  $80 \text{ g/m}^2$  were chosen as basic filter for the measurements performed for this thesis (at irradiances of  $100 \text{ W/m}^2$ ).

### 3.3.3 Color Filters

To create colored light out of the white light of the sulfur lamp used for STC IV-curve measurements, four colored transmittance filters from the company “LEE Filters” were used, covering the whole visible light spectrum. The colors were blue, green, yellow and red. Additionally, the red and blue filter were combined to obtain a filter only transmitting infrared light. Together with the white filter, six colors have been measured. The color codes of the used filters are “120 Deep Blue”, “139 Primary Green”, “643 Quarter Mustard Yellow” and “026 Bright Red”.

First, the transmitted irradiance of every filter combined with one and two white filters was measured with a pyranometer. The lamp power was adapted until the pyranometer measured an irradiance closest to  $100 \text{ W/m}^2$ . It turned out that all filters can reach the demanded  $100 \text{ W/m}^2$  when combined with two white filters but some stay well above  $100 \text{ W/m}^2$  when combined with one white filter only because the lamp can’t be dimmed low enough without losing its spectral class. Therefore it is more convenient to use two white filters for all light soaking measurements so the basic filters don’t have to be changed. The results of colored filters combined with two white filters can be seen in table 3.6.

Filter	Lamp power	Irradiance [W/m <sup>2</sup> ]
white	1050	101.2
blue	1140	99.5
green	1260	99.4
yellow	1050	99.9
red	1030	100.4
red and blue	1240	100.3

Table 3.6: Measured irradiance [W/m<sup>2</sup>] of color filters combined with two white sheets of paper.

For information on the actual spectrum transmitted through the filter combinations the transmitted light of the filters with the lamp settings from table 3.6 has been measured with a spectrometer. The result of every filter is shown in figure 3.17.

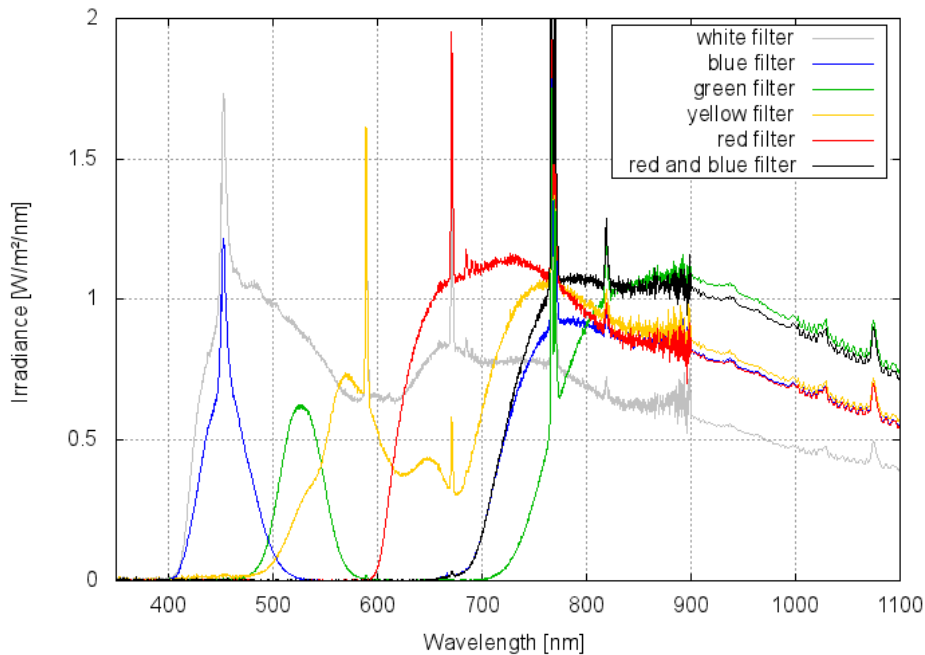


Figure 3.17: Spectral Irradiance of the colored illumination configurations used for the colored light soaking experiments. The data was measured with a spectrometer.

All color filters transmit parts of the visible light (depending on their color) and most of the infrared light. This makes it very important to measure the infrared light too, because for correct interpretation the effect of the infrared part of the transmitted light needs to be known. Figure 3.17 also shows that the whole visible spectrum is covered by the four chosen filters, which are partly overlapping.

The color specific bandwidths (without the infrared) are listed in table 3.7

Furthermore, the filters have been measured without additional white filters with a transmission measurement method. The results are shown in figure 3.18. When dividing the values measured by the spectrometer through the values of the spectrum of two

---

Filter	bandwidth [nm]
Blue	424-501
Green	504-551
Yellow	540-665
Red	620-726
Infrared	>723

Table 3.7: Bandwidths of the color filters. The lower and upper wavelength of the bandwidth are those, where the irradiance is half of the maximum irradiance.

white filters, one should get the same values as from the transmittance measurement. In fact the values are very similar in the visible spectrum as can be seen in figure 3.18. The spectrometer measurement has a lot of noise below 400 nm and between 800 and 900 nm. The transmission measurement shows a wavelike behavior for wavelengths above 800 nm. This is caused by multiple partial reflections and resulting interferences in the transmitted light due to the small thickness of the color filters. Although the curves fit rather well, the transmittance values of low wavelength light are generally higher than those calculated from the spectrometer measurements, whereas for long wavelength light it is the other way around. One possible explanation for this are calibration problems from the spectrometer.

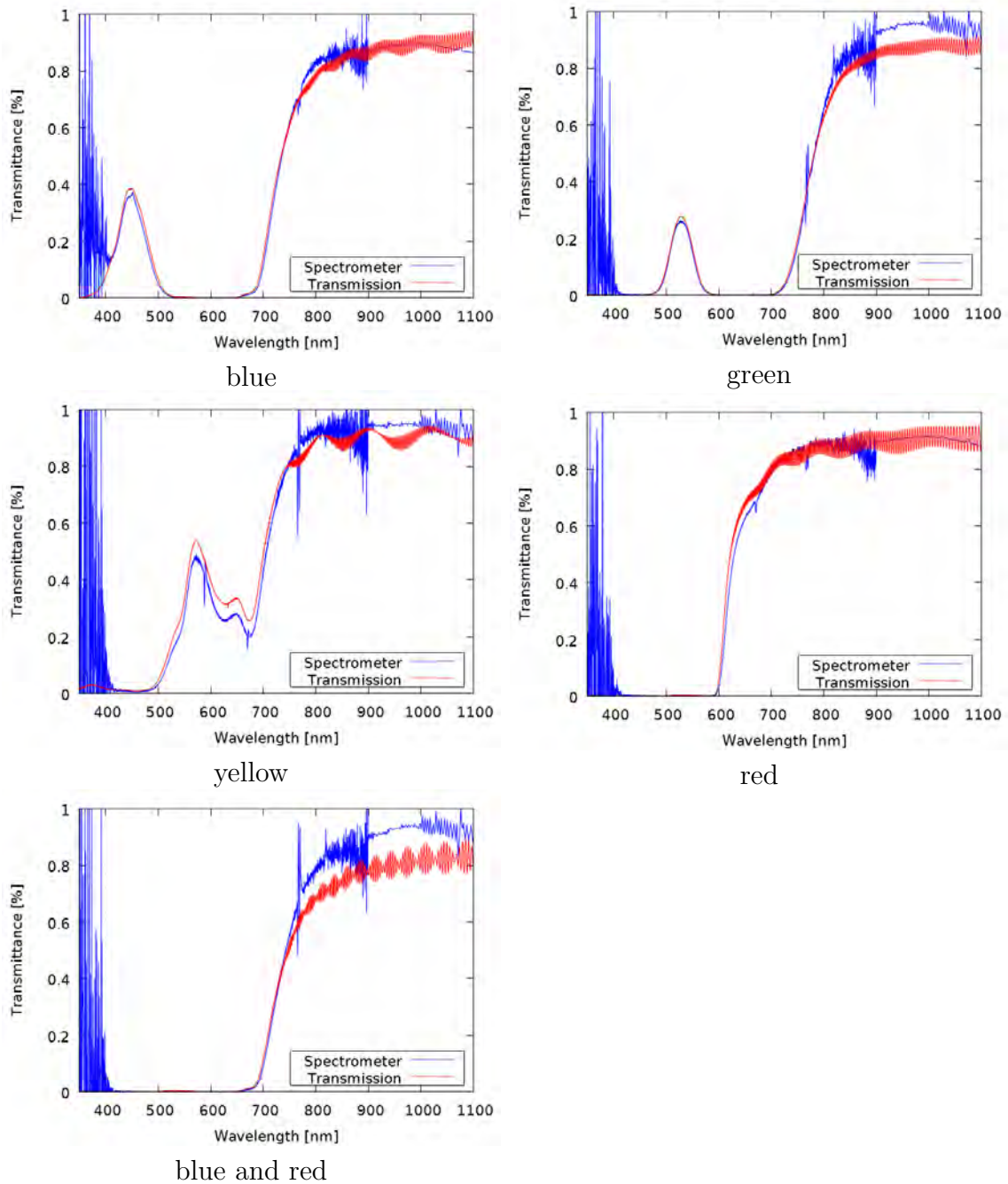


Figure 3.18: Comparison of the transmittance of the colored filters measured directly (red) and calculated from spectroscopy measurements (blue). To calculate the transmittance from spectrometer measurements, the spectra measured from the light soaking configurations were divided by a spectrum of two white papers of the same lamp power.

### 3.3.4 Uniformity

Another important setup characteristic is the uniformity of the incident light on the measuring plane. As suggested in the IEC norm 60904-9, the irradiance at the measuring plane was measured with a pyranometer over a  $24 \times 24 \text{ cm}^2$  grid with a measuring

point every 2 cm. This was realized under filtered light at  $100 \text{ W/m}^2$ .

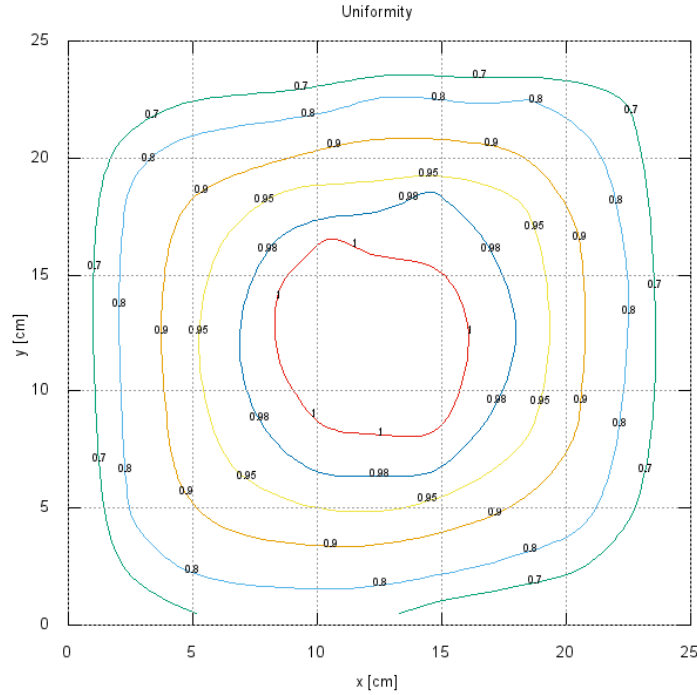


Figure 3.19: Uniformity of the measuring plane with installed filters. The maximum is normalized to 1.02, thus the line of 0.98 shows the border of class “A” uniformity. Class “A” is reached within a circle of around 12 cm in diameter in the center of the measuring plane. With samples of less than  $5 \times 5 \text{ cm}^2$  and a reference cell of  $2.5 \times 2.5 \text{ cm}^2$  there is still enough room for the temperature sensors as can be seen in figure 3.2.

During the first measurements, the output of the pyranometer increased over time which lead to a sloped uniformity. Further investigation showed, that this was due to an increase in temperature of the pyranometer over the time of a uniformity measurement. To perform the uniformity measurements, the pyranometer was positioned on a drawer within a coordinate system (see figure 3.20) and was then slid under the light. After reaching an equilibrium after a few seconds, the voltage output of the pyranometer was recorded and the pyranometer was slid out again. When investigating the shift in voltage output, the output at the start and the end of each such procedure were also recorded and compared. It turned out, that right after sliding the pyranometer out, it showed a 10% higher output than before sliding it in. The output would then decrease again to the initial value within seconds. However, when the pyranometer was left under illumination a few seconds longer than needed to reach equilibrium to measure the irradiance, the voltage output would not relax to the initial value but instead increase a few percent. Over a series of 169 measurements as it was performed for the uniformity measurement, this lead to an increase in voltage output of around 40mV



while the highest measured output was 851 mV, thus being a systematic error of 4.7%. The most likely explanation for this increase is a heating of the pyranometer by the irradiance and the heated air from the sulfur lamp. The uniformity measurement was repeated with recording of the voltage before sliding the pyranometer in. By simply subtracting the increase from the measured value, the uniformity measurements could be corrected and the result can be seen in figure 3.19.

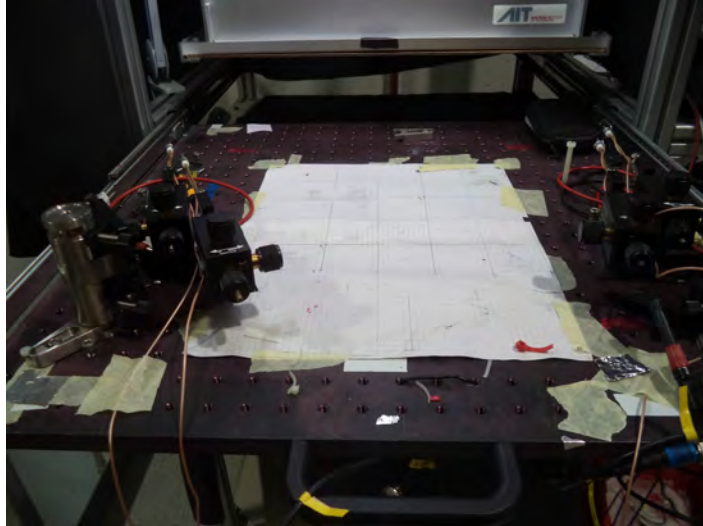


Figure 3.20: Coordinate system on the drawer to measure the uniformity.

When normalizing all the values to 1.02 times the maximum, every value between 0.98 and 1.02 satisfies class “A” uniformity. The area of less than 2% difference is approximately a circle of 12 cm in diameter. This is enough to fit any cell of the samples which are  $5 \times 5 \text{ cm}^2$ , the reference cell which is a  $2.5 \times 2.5 \text{ cm}^2$  square in the middle of a  $5 \times 7 \text{ cm}^2$  block and the temperature sensors on the glass. The arrangement can be seen in figure 3.2.

### 3.3.5 Temporal instability

#### Short term temporal instability

The IV-curve measurements during the light soaking experiments are the same as for the STC measurements described in section 3.1.1. Therefore the short term temporal instability is the same.

#### Long term temporal instability

The long term temporal instability from the light soaking experiments is different to that of the STC IV-curve measurements because the whole experiment lasts around two hours. The easiest way to measure the long term temporal instability is to use the data collected from the reference cell. The average  $I_{SC}$  of each IV-curve measurement can be calculated and compared to the first measurement. In this manner, the stability of the lamp can be determined.

In the measurements performed, the long term temporal instability was below 2% for most of the experiments. Only a few had long term temporal instabilities of above 2% but always below 5%. The long term temporal instability of each light soaking experiment is indicated in the boxes in the upper left corners of each experiment's diagram of figure 4.3 and figure 4.5.

Because of non-linear irradiance dependent effects in CIGS cells (explained in section 2.4.1) it is difficult to make precise corrections of CIGS IV-curves according to the IEC norm 60981. Therefore only the  $I_{SC}$  has been corrected, also because the absolute values of each IV-curve measurement are not as important as the general trend, for which a long term temporal stability of below 5% is enough.

### 3.3.6 Temperature

As explained in section 2.2.1, the temperature of the cell has to be kept stable to perform reliable measurements. To achieve this, the same cooling mechanism as for the IV-curve measurements was used. While for single IV-curve measurements at STC the cooling system is only important for bringing the cell to the required temperature, in light soaking measurements the development of the temperature becomes important. This development is influenced by the cooling pump's pumping capacity, the cooling medium's (water) temperature, the time dependent temperature transfer mechanisms (from cooling medium to chuck to glass substrate to cell surface), the irradiance and the air temperature around the cell. Some tests have been run to gain information on the temperature development under  $100 \text{ W/m}^2$  irradiation, leading to the following procedure of cooling. While the cell was still stored in the dark, it was tempered to around  $25 \text{ }^\circ\text{C}$ . Before uncovering it and starting the light soaking process, the cooling pump was set down by  $2 \text{ }^\circ\text{C}$ . Then the cell's surface temperature was observed and as soon as it dropped by  $0.1 \text{ }^\circ\text{C}$ , the light soaking experiment was started. By this method temperature curves like the ones in figure 3.21 were reproducibly achieved with an average temperature difference of  $\pm 0.3 \text{ }^\circ\text{C}$  and a maximum difference of  $\pm 0.5 \text{ }^\circ\text{C}$ .

According to table 2.1 this leads to errors of  $\pm 0.16\%$  ( $V_{OC}$ ),  $\pm 0.01\%$  ( $I_{SC}$ ),  $\pm 0.18\%$  ( $P_{MPP}$ ) and  $\pm 0.04\%$  (FF). Therefore no further temperature correction was applied to the data.

This only applies for light soaking experiments with  $100 \text{ W/m}^2$  irradiation. Light soaking experiments have also been performed at STC, where the maximum temperature difference was  $\pm 0.97 \text{ }^\circ\text{C}$ , leading to errors of  $\pm 0.60\%$  ( $V_{OC}$ ),  $\pm 0.04\%$  ( $I_{SC}$ ),  $\pm 0.70\%$  ( $P_{MPP}$ ) and  $\pm 0.16\%$  (FF). These errors are quite high but the results are still significant, especially when considering that these maximal errors occur only during the first 15 minutes of the light soaking measurements, while the temperature difference between the initial and the final measurements, which are most important for the finding of trends in the cell's light soaking behavior, are lower ( $\pm 0.58 \text{ }^\circ\text{C}$ , leading to errors of  $\pm 0.18\%$  ( $V_{OC}$ ),  $\pm 0.01\%$  ( $I_{SC}$ ),  $\pm 0.21\%$  ( $P_{MPP}$ ) and  $\pm 0.05\%$  (FF)). As described in section 3.1, the pin holders had to be covered with paper arches in order to prevent excessive heating of the pin holders leading to loss of contact and risk of damaging the cell.

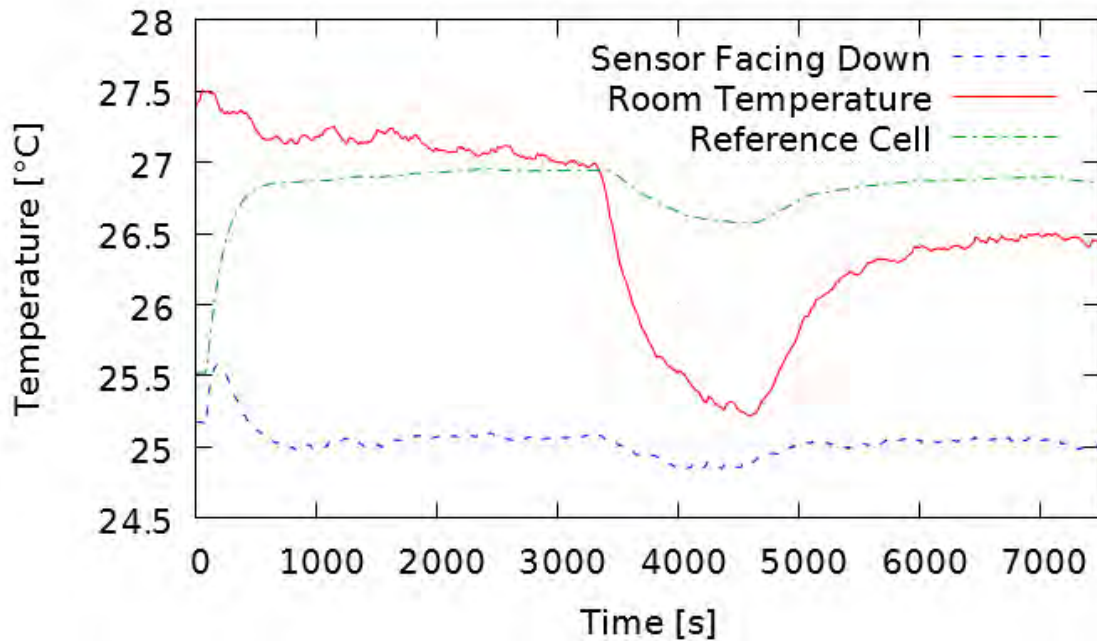


Figure 3.21: Development of temperature during a light soaking experiment. The temperature of the down facing sensor (closest to cell's surface temperature), the surroundings temperature and the reference cell's temperature are displayed.

Figure 3.21 shows all characteristic effects of the temperature development of the light soaking measurements performed during this work. The curve starting lowest (blue) is the temperature curve of the cell's surface, the one starting in the middle (green) leveling at around 27 °C is the reference cell's temperature and the one starting on top (red) with a steep drop below 25.5 °C after 3000s is the room temperature. The cell's temperature is stable for a minute at the beginning (while it is still stored in the dark) and then decreases a little, as the temperature of the cooling pump is decreased. The quick increase is caused by the sudden illumination when the light soaking process is started. This is the same for the reference cell. While the sample cell stops heating up after around two minutes at 25.5 °C, the reference cell's temperature keeps strongly increasing for almost ten minutes because it is encapsulated in a solid block and it can't be cooled as efficiently as the sample cell. The temperature of the sample cell decreases again after it has reached its maximum after two minutes of light soaking. It usually reaches its minimum after around 15 minutes (which is below the initial value), except during this measurement where the surrounding room temperature decreased almost 2 °C after one hour, causing the temperature of the sample and the reference cell to decrease too. This caused a bigger error in the measurement data, but still remaining below the  $\pm 0.5$  °C discussed above.

### 3.3.7 Automation by Keithley script

As mentioned before, a light soaking experiment consists of several successive IV-curve measurements after known time intervals. In between the IV-curve measurements the

cell is to be held in a stable bias state. This means, that most of the time the experimenter does not have to control the experiment. This process is a perfect example of beneficial implementation of an automated software routine in order to avoid long stand-by phases for the experimenter. Therefore a script has been written for the Keithley Software “TSP Express”. The script starts an IV-curve measurement after waiting intervals according to a list. Each IV-curve measurement consists of 200 measuring points, which are defined by incremented values of the voltage. The starting and the final value of the voltage range can be manually defined, thus also defining whether the measurement starts at the minimum or maximum voltage. Each IV-curve measurement takes 200ms.

As described in section 2.4, the bias on the sample cell is important for the light soaking process. For this thesis, open circuit bias was chosen, meaning that the script had to be programmed to set the sample cell under open circuit bias in between the IV-curve measurements. After every, individually selectable time interval, the script performs an IV-curve measurement, adding the data to a text file, from where later on the light soaking relevant values could be taken by another program. Because the cells have different  $V_{OC}$ , a single IV-curve measurement had to be performed (manually) for every cell to find the  $I_{SC}$  and  $V_{OC}$  under colored low light illumination so the measuring range (start voltage and end voltage as well as current limitation) can be set to reasonable values. After these initial measurements, the sample cell has to be dark soaked again. Therefore these measurements have been performed at once for all sample cells and all colors before the light soaking experiments. This means that at the initial measurements the sample cells are not under exactly known states (somewhere in between dark soaked and fully light soaked) and the data from these measurements should therefore not be compared. They only provide an overview of the sample cells performance (varying in  $V_{OC}$  from 0.3V to 0.5V) to optimize the measuring range.

With the script written for the low irradiance light soaking measurements of this thesis, also light soaking experiments at  $1000 \text{ W/m}^2$  or any other irradiance can be performed. It is also possible to prolong the light soaking experiment by simply adding further time intervals or to obtain more detailed time resolution by splitting the time intervals. It is also possible to apply different bias to the sample cell during the light soaking phases between the IV-curve measurements, e.g. short circuit bias.

The program developed for analyzing the text file produced by the “Keithely TSP Express” script automatically plots every IV-curve corrects the values by the reference cell output, as described in section 3.1.1, finds the  $V_{OC}$ ,  $I_{SC}$ ,  $P_{MPP}$  and FF of every IV-curve and plots these values as can be seen in figure 4.3.

#### **Dark Soaking /Relaxation**

It is very important for light soaking experiments, that the sample cell is in a known state before starting the light soaking experiment. The best state to start from is the completely relaxed, dark soaked state. To reach this state, CIGS cells have to be stored at room temperature in complete darkness for several hours, preferably overnight. To achieve this, the sample cells were covered with a cardboard box and a black cloth, shielding off any light. After they have been contacted with the four pins. The box’s main purpose is to protect the pins from being moved by the black cloth, which could cause a loss of contact or even worse damage the sample cell. Because never needed

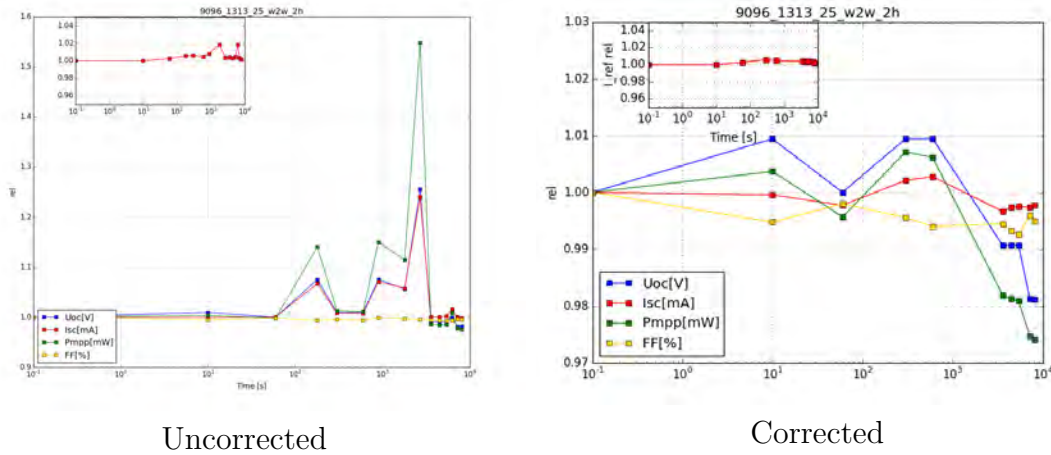


Figure 3.22: Light soaking curve of a sample cell with ZnO buffer layer (left) and the same curve with unlikely measurements removed (right). Measurements number four and seven to nine from the initial diagram have largely increased values in  $V_{OC}$ ,  $I_{SC}$  and  $P_{MPP}$ .

separately, the cloth is fixed on the box and can be quickly removed, which is very important right before the start of the light soaking sequence. In this way, the time needed to remove the dark soaking protection, move the cell under the selected illumination and starting the first IV-curve measurement could be reduced to under one second, thus minimizing the chance of unwanted changes of the cell's state due to stray light.

### 3.3.8 Data Reliability

Aside from statistical errors in the light soaking experiments, some other errors occurred, that are discussed in this chapter.

#### Spikes in Keithley Measurement

As can be seen in figure 3.22, some IV-curves of one light soaking experiment have significantly higher values in  $V_{OC}$ ,  $I_{SC}$  and  $P_{MPP}$  than the rest. These effects are not light soaking effects, but rather systematic errors. One possible explanation are external electric signals picked up by the Keithley measuring system because the pin holders and the pins contacting the sample cell are not electrically shielded and can therefore act as an antenna. External electric signals might have been caused by a next door high voltage, high power electric laboratory.

A comparison of two IV-curves, one with and one without pick-up signal can be seen in figure 3.23. It can be seen that the IV-curve with pick-up signal is simply shifted upwards, but no changes in the curve or steepness can be found, as is also reflected by a relatively constant fill factor. The removing of the spikes is also justified because for the light soaking effects the general trend is more important than a single measurement.

### Contact loss

One of the biggest problems in the presented setup is the contacting of the cells. As described before, the cells have been contacted by four pins that are pressed onto the cell's contacts by springs in pin holders. The electric contact is established by the pressure of the pin onto the cell's contact surfaces. Irradiance on the pin holders can cause them to thermally extend and move the pins until the contact is interrupted. Heating of the springs can cause the pins to move upwards, also interrupting the electric contact when not enough pressure has been applied initially. However, when applying too much pressure, the cell can be damaged.

An example of an IV-curve measured with a bad electric contact is shown in figure 3.23. When this happens, the measurement has to be repeated and the pressure applied to the pin has to be adapted. Errors like this happen less and less with increase of experience on the setup.

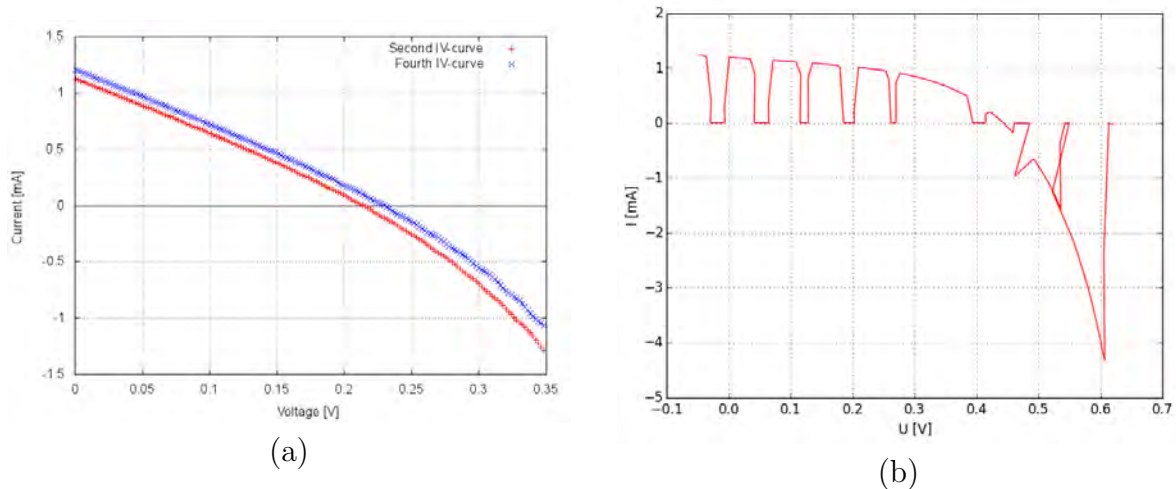


Figure 3.23: In (a) the IV-curve with pick-up signals caused by the lamp (red) is compared to the IV-curve corrected with the reference cell's measurement (blue). In (b) the form of the IV curve can still be guessed, but it is impossible to determine the cell's characteristics. The periodic sections of failures in measuring the IV curve correctly can either be caused by vibrations of the pin or by the internal procedure of the measuring device.

### Discrete values of $V_{OC}$

As can be seen in figure 3.24, the  $V_{OC}$  data seem to only have discrete values, jumping from one to the next. This is no physical characteristic of the cell but a systematic error in the measuring and analysis process. The Keithley measuring device measures IV-curves by forcing the cell to voltage outputs predefined by the minimum and maximum voltage and the number of steps of the IV-curve. At these predefined values the Keithley Sourcemeter measures the current output of the cell. Then the voltage is changed by one step and the current output is measured again. This means, that within one light soaking experiment, where the voltage range as well as the number of steps are equal for every IV-curve measurement, every IV-curve has data points at the same voltage values, except for statistical measuring errors that are very little compared to



the voltage steps. These statistical errors are around 0.2 mV considering a range of 1 V and an error of 0.02 % from the Keithley Sourcemeter. For a range of 1 V with 200 steps, each step is about 5 mV. Considering  $V_{OC}$ s of around 0.4 V leads to relative errors of around 1.25 %. This value is very close to the voltage steps in figure 3.24 of about 1.6 %.

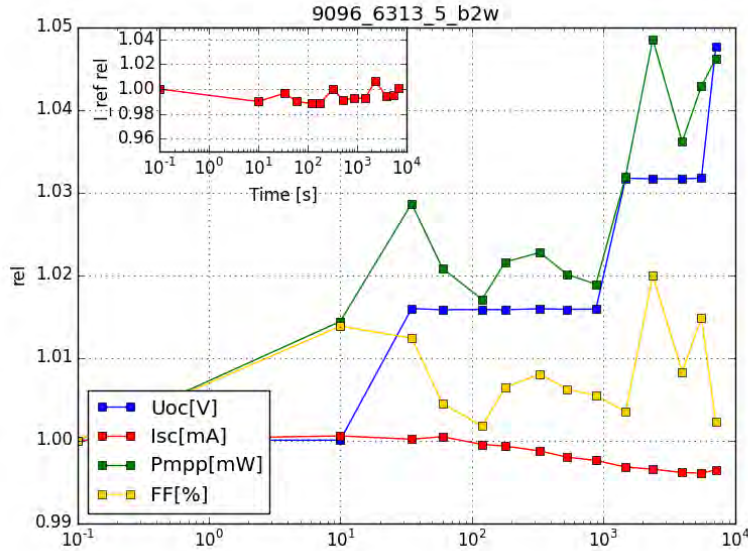


Figure 3.24: Light soaking measurement of a sample cell with ZnO buffer layer showing the discrete values of  $V_{OC}$

The program that reads the cell's characteristics from the IV curve chooses the voltage value from the IV data point, where the current is closest to zero (definition of open circuit). However, no interpolation is done. This means that only the values, measured by the Keithley are found in the light soaking curve. Because they are the same for every measurement, the  $V_{OC}$  in the light soaking curves seems to have discrete values only. As the errors produced by this are smaller than  $pm0.6$  %-points which is exact enough for the purpose of this thesis. If more exact results were needed, one can simply add a linear interpolation to the calculation function of the program used to analyze the Keithley output data.

# 4 Results

## 4.1 Specimen

For this thesis, CIGS cells produced at the Uppsala University were measured with the light soaking procedure explained in section 3.3. Two different cell types have been used, one with a CdS buffer layer and the other with a ZnO buffer layer. The recipes for the two cell types were exactly the same except for the buffer layer. The names of the sample batches of the measured cells are 9111\_6313 (CdS buffer layer) and 9096\_6313 (ZnO buffer layer).

The IV-curves have been measured for several cells of a batch of CIGS cells with both a CdS buffer layer and a cadmium-free buffer layer (ZnO). From the data,  $V_{OC}$ ,  $I_{SC}$ , FF and  $P_{MPP}$  have been extracted. Then for both buffer types one cell with relatively high and one with low  $V_{OC}$  have been chosen.

The  $V_{OC}$  is a indicator for the cell's quality as can be seen in equation (2.15). A high  $V_{OC}$  can only be reached by high  $I_{SC}$  and low dark saturation current  $I_0$ .  $I_0$  is highly dependent on the defect density of the crystal, as defects increase the recombination rate (Shockley-Read-Hall recombination) and thereby increase  $I_0$ . The  $V_{OC}$  also increases with the doping density, as can be seen in equation (2.17). However, this increase is limited as at very high doping densities the Auger-recombination becomes dominant, thus decreasing  $V_{OC}$ . The  $V_{OC}$  is thereby closely connected to the quality of the cell, which is determined by low defect density and optimum doping density.

From the CdS buffer layer cell's two further cell's have been chosen, both with similar  $V_{OC}$  between the first two and highly different  $I_{SC}$ . These have been chosen to show differences in the light soaking behavior that corresponds to different  $I_{SC}$ s. All the chosen cell's and their characteristics are listed in table 4.1 and their IV curves at STC can be seen in figure 4.1 and figure 4.2.

Buffer Layer	Cell Number	$V_{OC}$ [V]	FF [%]	$I_{SC}$ [mA]	$P_{MPP}$ [mW]	Quality
CdS	4	0.626	67.05	14.86	6.24	poor
	8	0.639	71.52	14.66	6.70	medium
	28	0.594	65.80	15.53	6.07	poor
	32	0.645	68.11	15.29	6.72	good
ZnO	5	0.558	58.32	14.50	4.72	poor
	17	0.565	63.53	15.67	5.62	good

Table 4.1: The  $V_{OC}$ ,  $I_{SC}$ , FF and  $P_{MPP}$  of the CIGS cells used for light soaking measurements. Their relative quality according to their values in  $V_{OC}$  and FF is given. The Cell CdS.28 was chosen due to its poor quality in  $V_{OC}$  and FF but high  $I_{SC}$ . The size of every cell is  $1.0 \times 0.5 \text{ cm}^2$ .



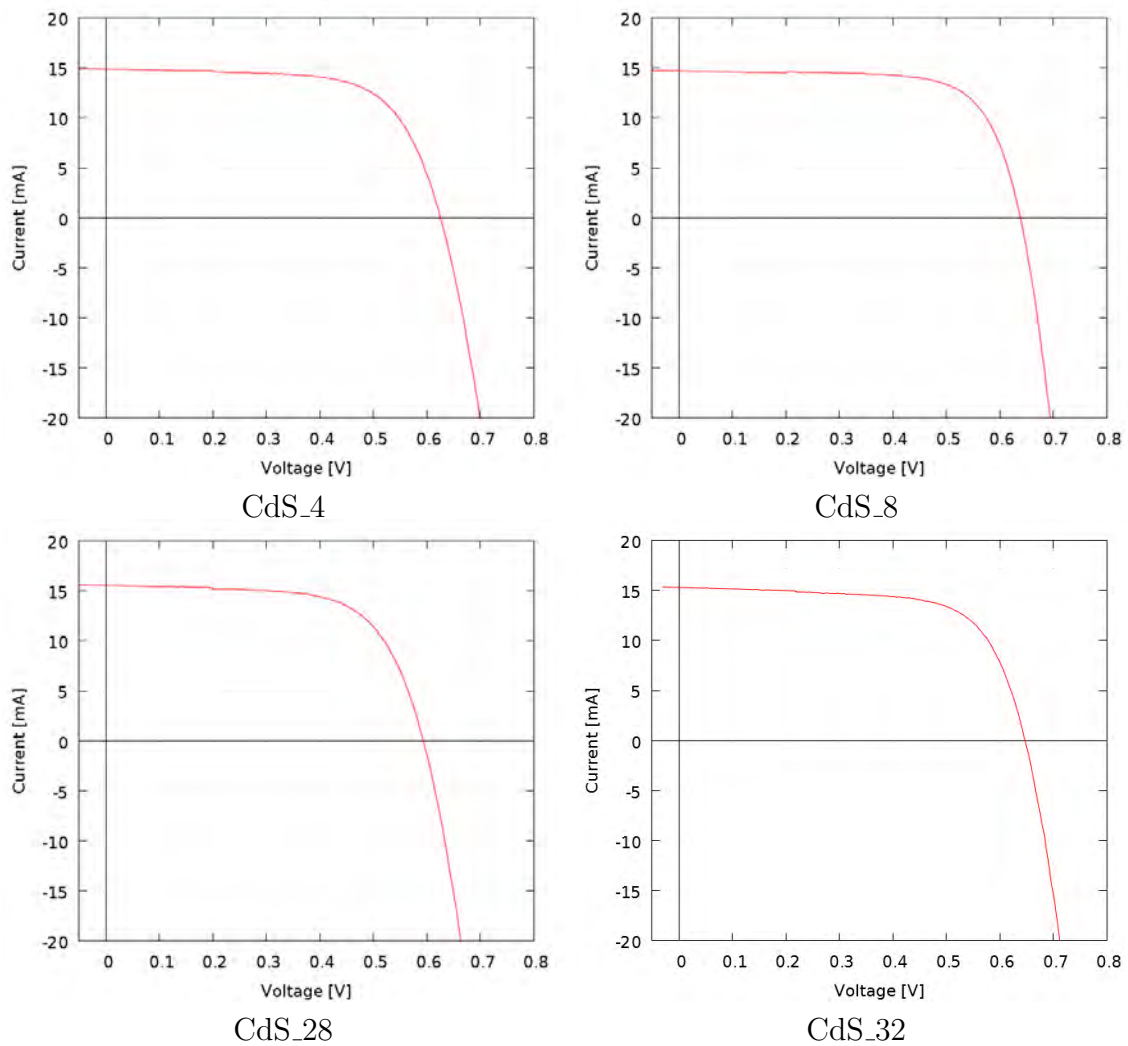


Figure 4.1: IV-measurement curves of the CIGS solar cells with CdS buffer layer.

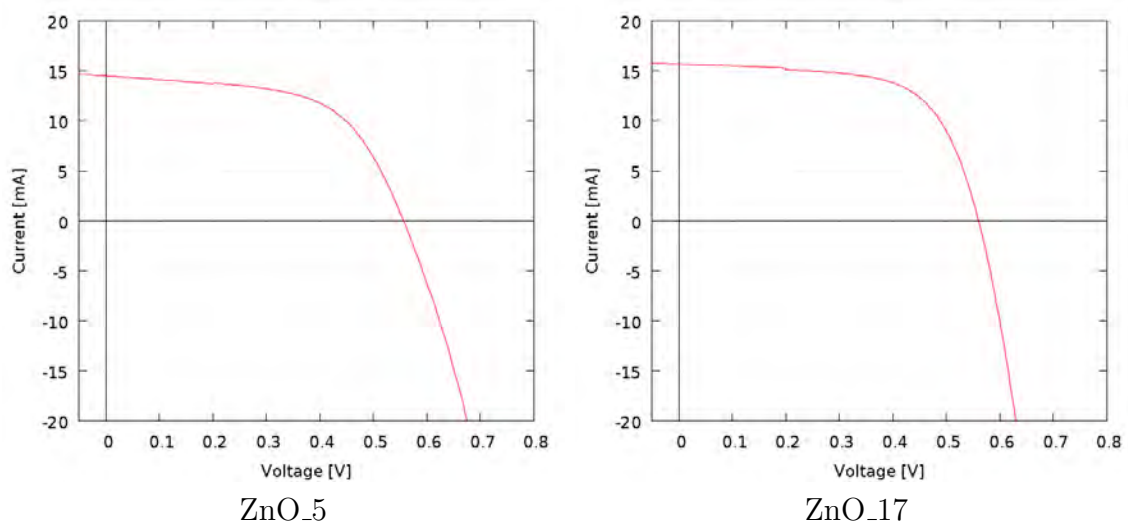


Figure 4.2: IV-curves of the CIGS solar cells with CdS buffer layer.

For both buffer layer types, one cell with high  $V_{OC}$  and FF and one with low  $V_{OC}$  and FF were chosen. Additionally, two CdS buffer layer cells were chosen. One with high  $P_{MPP}$  but low  $I_{SC}$  and one with high  $I_{SC}$  but all other parameters low. The cells will be referred to as “buffer layer” - “cell number”, e.g. CdS\_8.

## 4.2 Overview of the Light Soaking Results

An overview of the measured light soaking curves of the three main cells with CdS-buffer can be seen in figure 4.3. The results of the cell with high  $I_{SC}$  but low  $V_{OC}$  are compared with the cell CdS\_8 in figure 4.4. The results of the cells with ZnO buffer can be seen in figure 4.5. All results are summarized in table 4.2, table 4.3 and table 4.4. ‘/’ stands for steady increase, ‘\’ for steady decrease and ‘-’ for a stable development. ‘U’ indicates an initial decrease followed by an increase, ‘∩’ indicates an initial increase followed by a decrease.

		white	blue	green	yellow	red	IR
CdS_4	Dev.	/	/	/	/	/	/
	Fin.	+5.19	+4.65	+3.83	+4.59	+6.80	+1.61
CdS_8	Dev.	∩	∩	∩	∩	/	/
	Fin.	-2.06	-0.65	+0.66	+3.38	+9.76	+10.43
CdS_28	Dev.	U	U	/	\	/	U
	Fin.	+1.43	-2.19	+2.53	-1.52	+7.74	-4.74
CdS_32	Dev.	\	\	∩	∩	/	/
	Fin.	-5.75	-4.14	+2.22	+11.49	+22.68	+4.59
ZnO_5	Dev.	/	/	∩	∩	/	-
	Fin.	+5.04	+4.76	+3.44	+6.15	+10.25	+0.02
ZnO_17	Dev.	/	U	∩		/	U
	Fin.	-0.73	+2.17	+0.01		+12.95	+7.00

Table 4.2: Development (Dev.) and value of final change (Fin.) in % of the  $V_{OC}$  collected from the light soaking measurements of the measured cells. An explanation of the signs can be found in the text.

		white	blue	green	yellow	red	IR
CdS_4	Dev.	\	\	-	-	/	U
	Fin.	-2.50	-1.65	-0.09	+0.82	+3.12	-0.41
CdS_8	Dev.	\	\	U	/	U	U
	Fin.	-0.88	-1.26	-0.45	+6.62	+9.43	+7.04
CdS_28	Dev.	/	/	/	/	/	-
	Fin.	+2.22	+0.93	+7.35	+2.51	+22.13	+0.01
CdS_32	Dev.	\	\	\	\	∩	\
	Fin.	-7.34	-6.64	-6.86	-7.67	-0.84	-4.88
ZnO_5	Dev.	\	∩	-	-	-	/
	Fin.	-1.43	+0.22	+0.30	-0.35	-0.51	+1.88
ZnO_17	Dev.	U	\	/		\	∩
	Fin.	+0.41	-5.44	+1.06		-8.28	-1.55

Table 4.3: Development (Dev.) and value of final change (Fin.) in % of the FF collected from the light soaking measurements of the measured cells. An explanation of the signs can be found in the text.

		white	blue	green	yellow	red	IR
CdS_4	Dev.	/	U	U	/	U	U
	Fin.	+2.76	+3.10	+3.57	+6.56	+10.67	+1.64
CdS_8	Dev.	∩	\	∩	∩	U	/
	Fin.	-3.31	-2.44	+0.61	+14.45	+19.28	+19.00
CdS_28	Dev.	U	U	/	U	/	U
	Fin.	+3.41	-1.91	+12.93	+0.48	+33.53	-5.19
CdS_32	Dev.	\	\	\	∩	∩	U
	Fin.	-13.18	-10.47	-4.41	+4.84	+21.73	-0.26
ZnO_5	Dev.	/	/	∩	∩	/	∩
	Fin.	+3.57	+4.62	+4.07	+6.21	+9.09	+6.63
ZnO_17	Dev.	/	\	∩		/	U
	Fin.	-1.64	-4.05	+1.12		+2.88	+5.32

Table 4.4: Development (Dev.) and value of final change (Fin.) in % of the  $P_{MPP}$  collected from the light soaking measurements of the measured cells. An explanation of the signs can be found in the text.

### 4.2.1 Light Soaking of CdS Buffer Layer Cells

Four cells with a CdS buffer layer have been investigated. The cell CdS\_4, CdS\_8 and CdS\_32 have increasing  $V_{OC}$  and  $P_{MPP}$  with high FF. Cell CdS\_28 has one of the lowest  $V_{OC}$  and  $P_{MPP}$  of the CdS buffer layer sample but one of the highest  $I_{SC}$ .

#### CdS\_32

The CdS buffer layer cell with the best performance shows very interesting effects under light soaking as can be seen in figure 4.3. Under white light with low irradiance, all

the parameters except the  $I_{SC}$  decrease logarithmically over time after ten seconds, indicated by almost linear declining lines in the diagrams with logarithmic time axis. The FF and the  $V_{OC}$  decline by about 7%, the  $P_{MPP}$  by 14%. The same effect occurs under blue light but with the relative decrease is less (4% in  $V_{OC}$ , 6% in FF and 10% in  $P_{MPP}$ ).

In green light the FF develops quite similar, decreasing by 7%. The  $V_{OC}$  however initially increases during the first few minutes and then remains leveled until it decreases again after half an hour. The plateau is at around 4% and the final value of  $V_{OC}$  remains 2% above the initial value. The  $P_{MPP}$  is stable for the first six minutes and then decreases at the same rate as under blue light.

Under yellow light the FF still shows similar behavior and also a decrease by around 7%. The  $V_{OC}$  initially increases as under green light but with a higher plateau of 14%. Again, after half an hour the  $V_{OC}$  decreases again with a final value 11% higher than the initial one. As a result of the  $V_{OC}$  development, the  $P_{MPP}$  also increases until reaching a plateau after one minute at 11% and decreases back to plus 5% during the last one and a half hours.

## 4.2 Overview of the Light Soaking Results

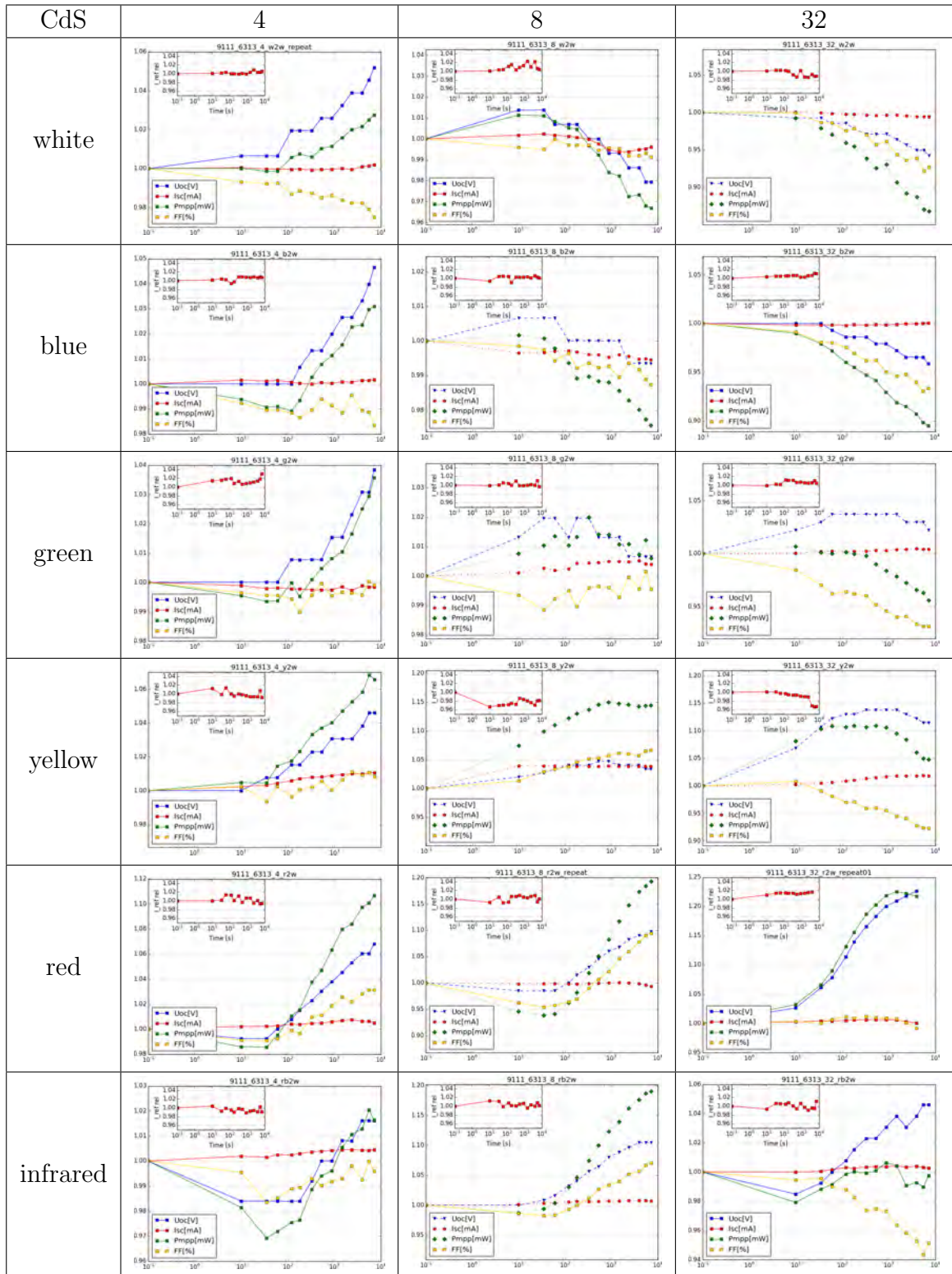


Figure 4.3: Results of the Light Soaking experiments of CIGS solar cells with CdS buffer layer. The x-axes show the logarithmic time of the measurement in seconds after starting the light soaking and the y-axes show the relative change of the parameters. The lines are for the guidance of the eye.

Under red light the FF no longer decreases but instead remains quite stable with changes of less than 2%. The  $V_{OC}$  increases even further than under yellow light. It's increase has a steeper phase for the first fifteen minutes and a flatter phase after that, but never reaches a plateau until it's final value of plus 23%. The  $P_{MPP}$  increases slightly steeper than the  $V_{OC}$  and reaches a maximum at plus 23% after one hour. It then slightly decreases due to a decrease in FF. The extremely high increase of  $V_{OC}$  might be caused by a decrease of the cell's series resistance, as will be discussed in section 4.3.

Under infrared light the FF develops as under blue light, decreasing by 7%. The  $V_{OC}$  initially decreases but this might also be due to a measurement error in the first measurement. It then increases steadily in a logarithmic way over time and finally reaches plus 5%. The  $P_{MPP}$  initially decreases due to the drop of  $V_{OC}$  but remains rather stable within  $\pm 2\%$ . This means that the decrease in FF and the increase in  $V_{OC}$  compensate each other.

As the white light includes all other colors but solely shows the effect of the blue light, it is quite probable, that the blue light effect is dominant for this cell.

While the FF development is the same for every light with the exception of red, the development of  $V_{OC}$  drastically changes with the color of incident light. It "bends upwards" with decreasing photon energy. The fact that it increases before increasing indicates that two different physical effects are working in parallel, serial, both having different time dependencies. This "bending" effect collapses under infrared light, probably because the photons don't have enough energy anymore to excite certain states of the energy band structure.

## CdS\_8

The CdS buffer layer cell with the medium performance also has a stable  $I_{SC}$  during any light soaking treatment. Under white light the FF slightly decreases by 1%. The  $V_{OC}$  and the  $P_{MPP}$  initially increase by 1%. The  $V_{OC}$  then decreases to a final value of minus 2% and the  $P_{MPP}$  to a final minus of 3%. Under blue light the development for all four parameters is very similar, with the main differences being the  $P_{MPP}$  not rising significantly but rather staying constant during the first minute and the final  $V_{OC}$  only being 1% lower than the initial value.

Under green light the initial increase of  $V_{OC}$  and  $P_{MPP}$  is larger than under blue light, just like it was for the cell CdS\_32. The  $V_{OC}$  increases by 2% and has a plateau starting after 30 seconds and lasting for around five minutes. then it decreases again until it reaches the initial value after two hours of light soaking. The FF shows a very small decrease at the beginning and then slowly returns to the initial value as well. The  $P_{MPP}$  initially increases a little slower than the  $V_{OC}$  (due to the initial decrease in FF). After 6 minutes the  $P_{MPP}$  reaches its maximum of +2%.

Under yellow light the  $I_{SC}$  abruptly increases by 4% after from the first to the second measurement. Having in mind that the  $I_{SC}$  stays stable in almost all other experiments, it is rather likely that this jump is a measurement error and the development should be compared to the second measurement. From there, the FF steadily increases by 5%. The  $V_{OC}$  increases by 3% until it reaches a plateau after around 8 minutes and then decreases again by 1%, leading to an overall increase of 2%. The  $P_{MPP}$  shows a very logarithmic increase for the first 9 minutes reaching a plateau at plus 7%.

## 4.2 Overview of the Light Soaking Results

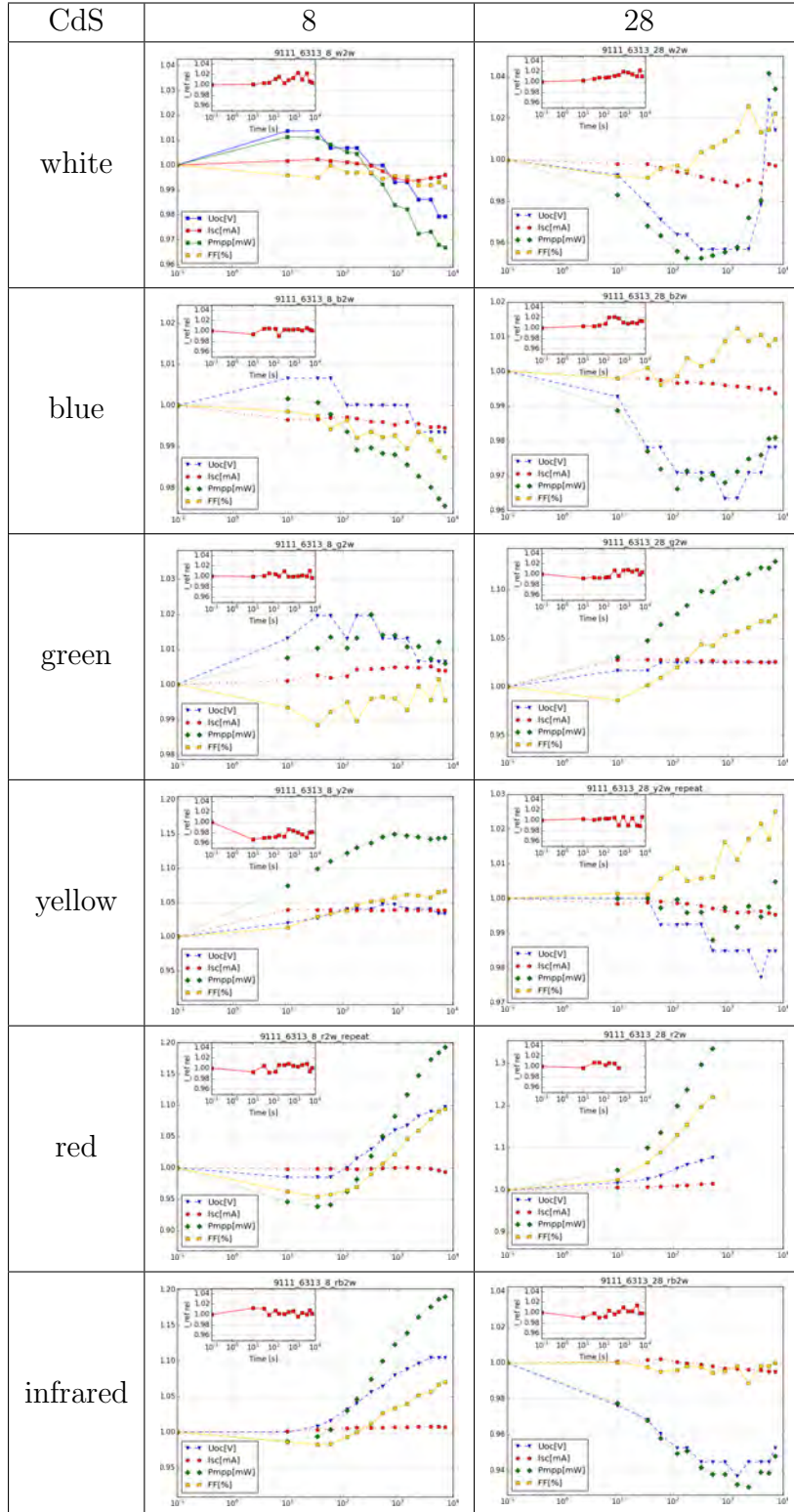


Figure 4.4: Results of the Light Soaking experiments of a CIGS solar cells with CdS buffer layer and relatively high  $I_{SC}$  but low  $V_{OC}$ . The CdS.8 cell from before is shown as comparison. The x-axes show the logarithmic time of the measurement in seconds after starting the light soaking and the y-axes show the relative change of the parameters. The lines are for the guidance of the eye.



Under red light the FF initially drops to minus 5% and then starts to steeply increase logarithmically to a total increase of 10% after 1 minute. The  $V_{OC}$  shows a similar development but turns around at minus 1%. The  $P_{MPP}$  initially decreases to minus 6% and after 1 minute increases logarithmically until it reaches plus 20%.

The parameter's development under infrared light is very similar to the one under red light. The minimum of FF and  $P_{MPP}$  are only 2% and the  $V_{OC}$  rather stalls initially than decreases before increasing. The final relative increase of  $V_{OC}$  and  $P_{MPP}$  are the same as under red light, the final relative increase of FF is only 7%.

As for the cell CdS\_32, the cell CdS\_8 shows the same development under blue light as under white light, meaning that the blue light effect again is dominant. It also shows the "bending" of the  $V_{OC}$ , it already starts under blue light consisting of photons with approximately 2.8 eV. Overall, the increase of  $V_{OC}$  stays smaller than in the CdS\_32 cell, but the development of the FF of the CdS\_8 cell also "bends upwards" with decreasing photon energy, leading to similarly high increases in  $P_{MPP}$ . Furthermore these effects remain under infrared light.

#### CdS\_4

The cell CdS\_4 with the poor performance shows very different behavior under white and blue light. There is no more total decrease in  $V_{OC}$  and  $P_{MPP}$  but instead the initial increase from CdS\_8 continues logarithmically until the  $V_{OC}$  reaches a final increase of plus 5% and the  $P_{MPP}$  a final increase of 3%. The FF decreases by slightly more than 2%, under blue light quicker than under red light, leading to an initial decrease of  $P_{MPP}$  by 1% under blue light. All developments are logarithmic over time.

Under green light the FF of the CdS\_4 cell slightly decreases by 1% before returning to its initial value again. The  $V_{OC}$  remains stable for around one minute before increasing by a total of 4%. The  $P_{MPP}$  slightly decreases at first and finally reaches a total increase of 4%.

Under yellow light the  $I_{SC}$  increases by around 1%, again probably due to measurement errors rather than representing a real physical effect. The FF also increases by 1%. The  $V_{OC}$  increases by 5%, this time without an initial plateau. The  $P_{MPP}$  increases by slightly more than 6%.

Under red light the FF and the  $V_{OC}$  show a slight initial decrease of around 1% and then increase to final values of plus 3% (FF) and 7% ( $V_{OC}$ ). As a result, the  $P_{MPP}$  initially decreases by 2% and reaches a final overall increase of 12%.

Under infrared light the CdS\_4 cell shows a decrease in FF and  $V_{OC}$  by 2%. The FF then increases to its initial value and the  $V_{OC}$  increases to 2%. The  $P_{MPP}$  initially decreases by 2% and then increases to 2%.

#### CdS\_28

The parameters of cell CdS\_28 under STC are very different from the other CdS cells. CdS\_28 has high  $I_{SC}$  and the lowest  $V_{OC}$ , FF and  $P_{MPP}$ . It also shows very different behavior under light soaking.

Under low irradiation white light the  $V_{OC}$  initially decreases rapidly, reaching a minimum of -4% after 6 minutes, whereas the biggest  $V_{OC}$  decrease amongst the other CdS cells is 4% after two hours. After 45 minutes the  $V_{OC}$  of the CdS\_28 cell increases



to reach a final overall increase of 2%. The FF increases to plus 2% after a decrease of around 1%. The  $P_{MPP}$  initially decreases by 5% and then increases with the  $V_{OC}$  to finally reach +4%.

Under blue light the FF increases by 1%. The  $V_{OC}$  and the  $P_{MPP}$  initially decrease by 4% and then increase to a final total decrease of 2%.

Under green light there is a jump in the measurement indicated by the sudden change of  $I_{SC}$  to the second measurement. From there the FF increases by 7%, while the  $V_{OC}$  increases by 2%. The  $P_{MPP}$  increases by 10% after the second measurement. The developments under green light are logarithmic with time.

Under yellow light the FF increases logarithmically by 2% and the  $V_{OC}$  decreases logarithmically by 2%. The  $P_{MPP}$  stays constant.

The red light experiment shows a relatively big increase in  $V_{OC}$  (9%), FF (22%) and  $P_{MPP}$  (33%) after nine minutes.

Under infrared light the FF remains constant. The  $V_{OC}$  and the  $P_{MPP}$  decrease logarithmically by 6% within the first thirty minutes before increasing to a total of minus 5%.

## 4.2.2 Light Soaking of ZnO Buffer Layer Cells

### ZnO\_5

The cell ZnO\_5 is a cell with buffer layer and has an overall relatively poor quality. Under white light soaking, its  $V_{OC}$  and  $P_{MPP}$  increase by 5% and 4% respectively. The FF on the other hand decreases by 1%. The  $I_{SC}$  remains constant as for all light soaking measurements of this cell.

Under blue light, the  $V_{OC}$  increases by 5% and the FF increases by 1% after several seconds and then remains relatively constant. The  $P_{MPP}$  increases by 5%.

Under green light, the  $V_{OC}$  increases by 3% after several seconds and then remains constant. The FF oscillates between +1% and -1%. The  $P_{MPP}$  increases by almost 5% after six minutes and then remains between 4 and 5%.

Under yellow light the FF remains constant. The  $V_{OC}$  reaches a plateau at +6% after 6 minutes. The  $P_{MPP}$  reaches a peak of +8% after 6 minutes and then decreases to a total increase of 6%.

Under red light the FF remains constant as well. The  $V_{OC}$  as well as the  $P_{MPP}$  logarithmically increase to a final +10%. Some spikes as explained in section 3.3.8 occurred in this light soaking experiment at measurements number 3, 11 and 12.

Under infrared light a jump of  $I_{SC}$  and  $P_{MPP}$  occurred after the first measurement and therefore the development of the parameters is compared to the second measurement rather than the first one. The  $V_{OC}$  and the  $I_{SC}$  remain constant. The FF and the  $P_{MPP}$  increase by 2%.

## 4.2 Overview of the Light Soaking Results

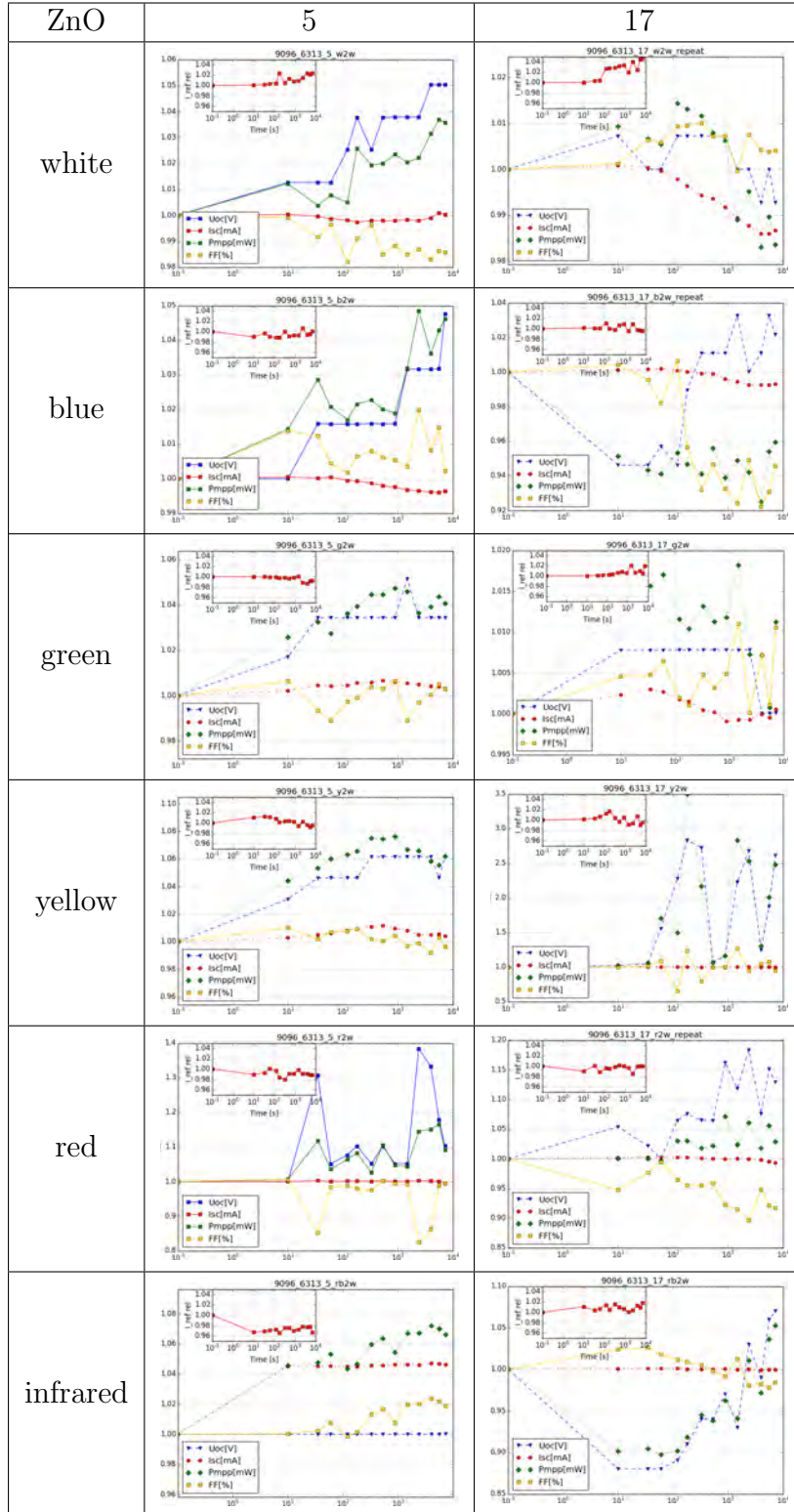


Figure 4.5: Results of the Light Soaking experiments of CIGS solar cells with ZnO buffer layer. The x-axes show the logarithmic time of the measurement in seconds after starting the light soaking and the y-axes show the relative change of the parameters. The lines are for the guidance of the eye.

## ZnO\_17

The cell ZnO\_17 is a good quality cell with a ZnO buffer layer. During all light soaking measurements on this cell contact problems occurred, leading to a lot of spikes as described in section 3.3.8.

Under white light soaking the FF, the  $V_{OC}$  and the  $P_{MPP}$  initially increase by 1%. After three minutes they all start to decrease. The FF reaches a final +0.4%, the  $V_{OC}$  a final -0.7% and the  $P_{MPP}$  a final -1.6%. The  $I_{SC}$  starts to decrease after one minute and reaches a final -1.3%.

Under blue light the  $V_{OC}$  and the  $P_{MPP}$  decrease by 6% after twenty seconds. While the  $P_{MPP}$  remains at that level for the rest of the experiment, the  $V_{OC}$  quickly increases to +2% after two minutes where it stabilizes. The FF remains constant for the first two minutes and then rapidly decreases by 7% within four minutes and remains at that value.

Under red light the FF decreases by 8%. The development is logarithmically but with some fluctuations as is the development of the  $V_{OC}$ . The  $V_{OC}$  increases by 12% and the  $P_{MPP}$  increases by 4%.

Under infrared light the FF increases by 3% after half a minute and then decreases logarithmically to a total decrease of -2%. The  $V_{OC}$  and  $P_{MPP}$  decrease by 10% after ten seconds, stay leveled for one minute and then increase logarithmically to a total increase of +5%.

## 4.3 Discussion

### 4.3.1 Open Circuit Voltage of CdS\_32 under Red Light

The high quality cell CdS\_32 shows an exceptionally high increase in  $V_{OC}$  under red light. As can be seen in figure 4.6, the initial  $V_{OC}$  is small due to a “cross over” (see section 2.4.1,[17]). Over time, the cross over effect is reduced, leading to the great increase in  $V_{OC}$ .

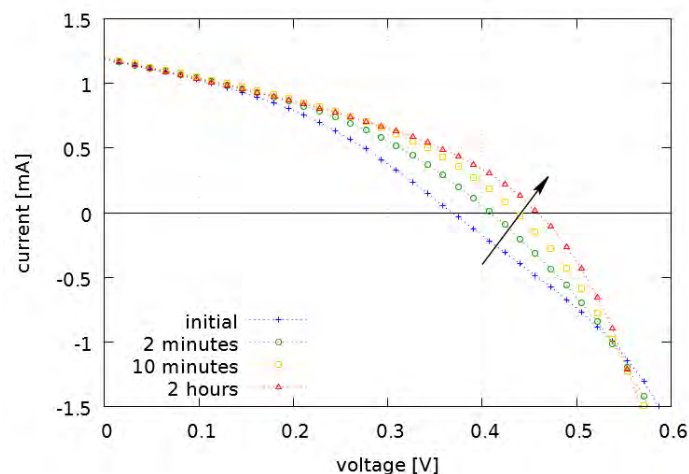


Figure 4.6: Change of the IV-curve of the CdS\_32 cell under red light illumination

At currents of -1.5 mA and below, the IV-curve of the CdS<sub>32</sub> cell under red light illumination develops the opposite way. Under blue light, the development below -1.5 mA is the same, but no cross over around  $V_{OC}$  can be seen. This makes it very plausible, that two different mechanisms are activated by red and blue light respectively. It is possible, that also under red light, the  $V_{OC}$  would start to decrease again after the initial increase, as it does under yellow and green light. This hypothesis is supported by the facts that under red light the FF decreases after 5 minutes and that the  $V_{OC}$  increase slows down after 5 minutes. To observe an inversion of the  $V_{OC}$  development, the light soaking experiment would most likely have to be prolonged by two hours.

### 4.3.2 Effect of Metastable Charge Carriers on Voc

As explained in section 2.4.1, CIGS cells contain  $(V_{Se} - V_{Cu})$  vacancy complexes that have metastable charge configurations [5]. The configuration transitions can be photon-induced as well as bias induced. The stability of each configuration depends on the exact composition of the material and varies from the deep absorber to the absorber/buffer interface. When a metastable configuration is generated, it locally binds an electric charge and thereby changes the electric charge density of the crystal. This behavior is very similar to that of a dopant. In the experiments performed in this work the main changes of parameters were observed in  $V_{OC}$  and FF (and  $P_{MPP}$  as a consequence) whereas  $I_{SC}$  remained stable. In the following a correlation between  $V_{OC}$  and doping concentration is discussed in order to find possible correlations between the metastable vacancy complexes and the measured changes in  $V_{OC}$ . A similar correlation between the effects and the FF could be done but would go beyond the scope of this master thesis.

As described in section 2.1.2 one possible way to create an internal electric field in a semiconductive material is by doping [16]. Though the basic internal electric field in CIGS cells is created by different material properties of the absorber, the buffer layer and the window layer, it is also effected by doping as it is in silicon solar cells. N-typing is adding an atom (or any combination of atoms) with an additional positive charge (e.g. adding Phosphorous to a silicon crystal). The added atoms are called donors. This is the same as generating a metastable  $(V_{Se} - V_{Cu})$  vacancy complex with higher positive charge than the original vacancy complex in this region of the crystal. A higher doping concentration increases the internal field and thereby also the  $V_{OC}$ . When adding the n-type material with p-type dopants (e.g. Boron in a Phosphorous doped silicon crystal) the effect of the doping is reduced.

As mentioned in section 2.4.1 red light induces a  $(V_{Se} - V_{Cu})^+ \rightarrow (V_{Se} - V_{Cu})^-$  transition in the CIGS absorber, thereby “doping” with acceptors. Blue light induces a  $(V_{Se} - V_{Cu})^- \rightarrow (V_{Se} - V_{Cu})^+$  transition near the CIGS/buffer interface [17], thus “doping” with donors.

As discussed in section 2.4.1, acceptors in the p-type region or donors in the n-type region increase the internal electric field thus increasing the  $V_{OC}$ . Adding acceptors to the n-type region or donors to the p-type region has the opposite effect (see table 2.4).

### 4.3.3 CdS buffer layer

Under white as well as under blue light the high quality CdS<sub>32</sub> cell shows an initial decrease in  $V_{OC}$ . Under green and yellow light, there is an initial increase followed by a decrease and under red light, there is only an increase. This means that the initial increase gets stronger and stronger with increasing wavelength of the incident light. As explained in section 2.1.3, the blue light is absorbed close to the buffer layer and red light is absorbed throughout the whole CIGS bulk. Hence, the blue light effect is buffer determined and the red light effect is bulk determined. As the development of parameters under white light illumination very much resembles the development under blue light, it can be concluded that the CdS<sub>32</sub> cell's metastable effects are buffer determined.

The white and blue light development of parameters of the CdS<sub>8</sub> cell (medium quality) look very much alike the development of the CdS<sub>32</sub> cell under green light: An initial increase is followed by a decrease. Again, the initial increase gets stronger with increasing wavelength of the incident light as with the CdS<sub>32</sub> cell. However, the threshold wavelength for the first occurring initial increase lies lower for the CdS<sub>8</sub> cell (i.e. at blue light with  $\lambda \approx 450$  nm instead of green light with  $\lambda \approx 550$  nm). Again, the cell is buffer determined, as the white light causes the same metastable changes of parameters as the blue light.

The low quality CdS<sub>4</sub> cell shows no decrease in  $V_{OC}$  under any light color. This can be interpreted as having an even lower threshold wavelength for increasing  $V_{OC}$ , so the pure increase that is not reached before red light illumination for the CdS<sub>32</sub> cell is already reached under blue light for the CdS<sub>4</sub> cell. As the blue and red light effects are the same for the CdS<sub>4</sub> cell, it is impossible to say whether its metastable effects are buffer or bulk determined. However, as both CdS<sub>8</sub> and CdS<sub>32</sub> are buffer determined, it is very likely that CdS<sub>4</sub> is buffer determined as well. Another indicator for this is the development of the FF. While it increases under red light, it decreases under white and blue light.

In summary, cell CdS<sub>4</sub> shows the same increasing development for all measured light colors, cell CdS<sub>32</sub> shows a transition from pure decrease under blue light to pure increase under red light and cell CdS<sub>8</sub> is a transition between cell CdS<sub>4</sub> and CdS<sub>32</sub>. In the following, the decrease of  $V_{OC}$ , FF and  $P_{MPP}$  under blue light will be called "blue light effect". The increase of  $V_{OC}$  under red light will be called "red light effect". However, the blue light effect does not occur in the CdS<sub>4</sub> cell and is reduced in the CdS<sub>8</sub> cell. This can be explained by the following hypothesis, taking the position of the p-n junction into account.

As discussed in section 2.1.2 and [16] the efficiency of a cell depends on how many photons are collected in the solar cell, preferably on the absorber side of the junction. In CIGS cells (as well as in silicon based cells) the CIGS absorber is the p-type material and the buffer layer as well as the window layer are the n-type material. Ideally the p-n junction is located at the absorber/buffer interface. Due to material impurities and material diffusion after the production process the p-n junction can shift into the absorber [19], thus reducing the cells efficiency.

If such a shift is the cause for the reduced quality of cells CdS<sub>4</sub> and CdS<sub>8</sub> compared to CdS<sub>32</sub>, then the missing of the blue light effect for CdS<sub>4</sub> and CdS<sub>8</sub> can be explained as follows. When illuminated by blue light, the CIGS layer produces

$(V_{Se} - V_{Cu})^+$  complexes acting as acceptors. This only happens close to the absorber/buffer interface, because blue light is absorbed within the first 250 nm in CIGS as can be seen in figure 2.1. Assuming the absorber is completely on the p-type side of the p-n junction, the blue light absorption leads to a donor-doping of the p-type material resulting in a reduction of the internal electric field. This causes a decrease in  $V_{OC}$  as was observed in the blue light soaking of the CdS\_32 cell. When the p-n junction is shifted inside the absorber, as is assumed for CdS\_4 and CdS\_8, the blue light induces donors on the n-type side of the p-n junction, thus increasing the  $V_{OC}$ . This idea is visualized in figure 4.7.

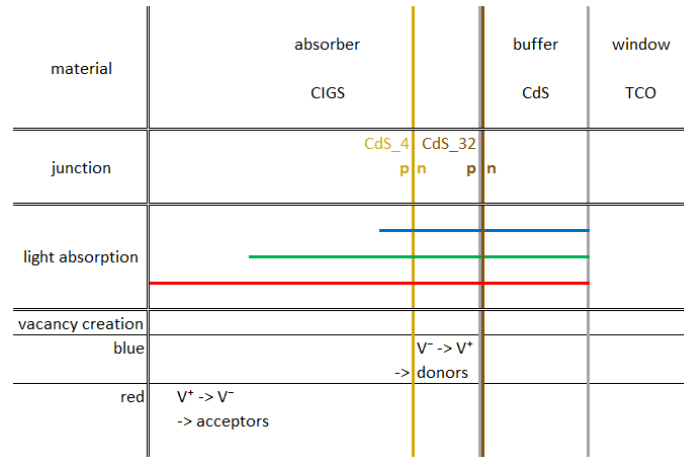


Figure 4.7: Localization of the absorber/buffer/window interfaces, the p-n junctions for cells CdS\_4 and CdS\_32, the position of color dependent light absorption and the type of vacancy creation from blue and red light. The x-axis represents the depth of the CIGS solar cell with the illuminated front being at the right hand side and the back contact at the left hand side. The shift of the p-n junction is caused by defects in the absorber close to the absorber/buffer interface.

The blue light effect seems to be dominant compared to the red light effect because the white light measurements show the same development as the blue light measurements for all three cells. However, the increase of  $V_{OC}$  caused by the red light effect can be seen in the initial phase of green and yellow light soaking of the CdS\_32 cell. This could indicate that the red light effect and the blue light effect develop differently over time.

A similar process could take place in the buffer layer but no literature on the metastable transitions in the CdS buffer layer could be found.

The cell CdS\_28 has very different properties than the other three CdS buffer layer cells. It has a high  $I_{SC}$ , but low  $V_{OC}$ , FF and  $P_{MPP}$ . As a result, the development of parameters under light soaking is very different to the others, regarding the  $V_{OC}$ . Cell CdS\_28 shows an initial decrease followed by a steep increase under white light as well as under blue light. Under red light, there is a constant increase. Despite this different development, some conceptual principles resemble the other three cells. First, the development under white light is the same as under blue light, therefore also the CdS\_28 cell is blue light determined. Furthermore the cell shows an inversion of the

initial blue light effect under red light, just like the other three cells. The development under green and yellow light could both be considered a transition when regarded separately. However, as the effect under green light is closer to the effect of the red light and the effect under yellow light is closer to the effect under blue light, green and yellow light soaking effects are not conclusive in the case of the CdS\_28 cell.

The different effects compared to the first three CdS cells could be caused by different defects and p-n junction characteristics that are also likely to be the reason for the relatively high  $I_{SC}$  but low  $V_{OC}$ , FF and  $P_{MPP}$ . To draw significant conclusions on the CdS\_28 cell, further measurements on cells with similar behavior would be necessary or a microscopic study on the exact defect structure should be done. This could be done with SEM-EDX, XRD or similar methods.

#### 4.3.4 ZnO buffer layer

The general picture of the light soaking measurements of the ZnO buffer layer cells is not as conclusive as for the CdS buffer layer cells. Cell ZnO\_5, being the ZnO buffer layer cell of poor quality, shows an increase of  $V_{OC}$  throughout all light colors. The  $P_{MPP}$  development is always similar to the  $V_{OC}$  and the FF only shows slight changes of under  $\pm 2\%$ . All IV-curves of the ZnO\_5 cell show roll overs that are not reduced by light soaking. Under red light, the ZnO\_5 light soaking measurements show several spikes. In general, there were far more spikes at the measurements of the ZnO buffer layer cells. Additionally to the causes mentioned in section 3.3.8, reasons for such spikes could be the fact that the IV-curves of some ZnO measurements are very flat-angled at the point of  $V_{OC}$  (see figure 4.8. This means that small errors of the current measurement by the Keithley Sourcemeter can cause great changes in the parameters.

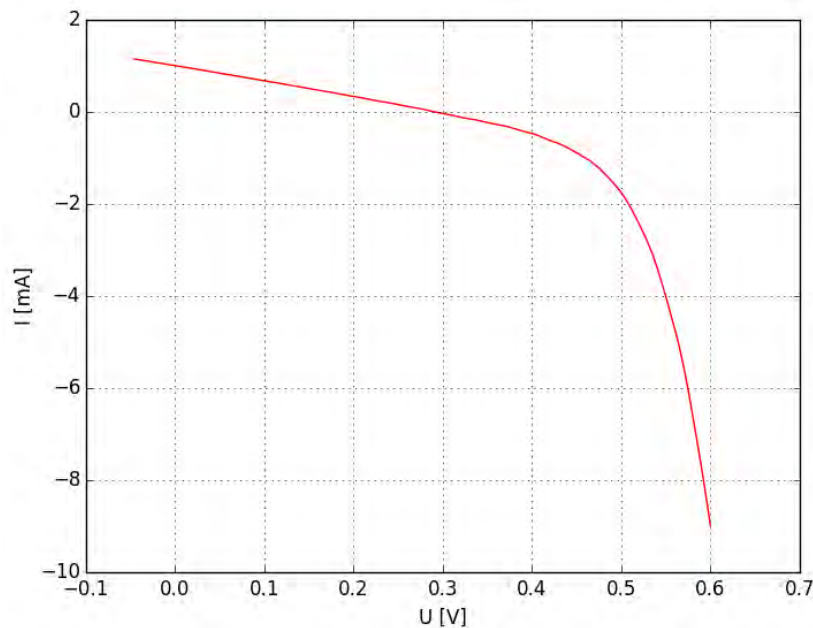


Figure 4.8: IV-curve of the ZnO\_17 cell under blue light, showing the flat angled IV-curve at the  $V_{OC}$ -point. This can lead to great changes of the parameters due to small errors in the measuring of the current.

Under white light the good quality ZnO buffer layer cell ZnO\_17 shows an initial increase of  $FF$ ,  $V_{OC}$  and  $P_{MPP}$  followed by a decrease. Under blue light, an initial decrease of  $V_{OC}$  and  $P_{MPP}$  is followed by an increase. They both are very sudden and a closer look at the  $I_v$ -curves indicate, that those jumps are very likely to be from measurement errors rather than physical properties of the cell. The yellow light measurement shows very high spikes, most likely caused by pick up signals. The whole light soaking measurement under yellow light is dominated by pick up signals in the  $I_v$ -curve measurements and can therefore not be considered relevant for interpretation. The infrared light measurements show a sudden decrease of  $V_{OC}$  and  $P_{MPP}$  after the initial  $I_v$ -curve. Because this decrease is not supported by another measurement but rather a steady increase in all following measurements can be observed, it is very likely that the initial decrease is caused by a measurement error of the initial  $I_v$ -curve.

### 4.3.5 Comparison of CdS and ZnO buffer layer

When comparing the CdS and ZnO buffer layer cells, the most obvious aspect is the similarity between the developments under white light of the cells CdS\_4 and ZnO\_5 as well as CdS\_8 and ZnO\_17. This would link the poor quality cells of both buffer layer types as well as the medium quality CdS buffer layer cell with the high quality ZnO buffer layer cell. For both there are further similarities that support the connection.

As for the low quality cells, both buffer layer types show an increase of  $V_{OC}$  and  $P_{MPP}$  under all light colors. Also the amplitude of their final values does not change a lot. However, under high wavelength light the CdS\_4 cell shows an increase of  $P_{MPP}$  accompanied by an increase in  $FF$  which was not observed for the ZnO\_5 cell. Another dissimilarity is the plateau of  $V_{OC}$  and  $P_{MPP}$  of the ZnO\_5 cell under green and yellow light which can not be observed for the CdS\_4 cell. Nonetheless, the general trends of the cells CdS\_4 and ZnO\_5 are similar.

As mentioned before, the cells CdS\_8 and ZnO\_17 show very similar behavior under white light. Under blue light, the ZnO\_17 measurement is probably not representative, as indicated by the sudden changes of  $V_{OC}$  caused by measurement errors as discussed before. Under green light however, both buffer layer types show an initial increase in  $V_{OC}$  and  $P_{MPP}$  followed by a decrease to a value close to the initial ones. Under red light, both buffer layer types show no more decrease but rather an increase in  $V_{OC}$  and  $P_{MPP}$ . This is also true for infrared light, considering the correction of the ZnO\_17 infrared measurement as discussed above.

The fact that the good quality ZnO buffer layer cell behaves similar to the medium quality CdS buffer layer cell supports the fact, that the CIGS cells with ZnO buffer layer are not yet as far and well developed as CdS buffer layer CIGS cells. This is also affirmed by the fact that all  $I_v$ -curves of the poor quality cell ZnO\_5 show cross overs, generally a sign for an undesirable limitation of the photocurrent [17].

The general similarities between the behavior of the cells with different buffer layers under light soaking suggest that metastable light soaking effects of CIGS cells are rather determined by the cells relative quality than the buffer layer material. The cells relative quality again is determined by defects and the matching of the band gaps [17].



### 4.3.6 Power Rating

In order to outline the relation between the change of  $V_{OC}$  under colored light soaking, the maximum power output under STC ( $P_{MPP}$ ) of all measured cells was divided by the maximum  $P_{MPP}$  (cell CdS\_32) and plotted together with the final change of  $V_{OC}$  (see figure 4.9). The linear trend lines were calculated for guidance of the eyes. However, the value of the ZnO.17 measurement under yellow light was not considered for the trend line calculations and is also not shown in figure 4.9 due to reasons explained above.

Two trends can be seen in figure 4.9: First, the final values (and therefore the trend lines) shift upwards with increasing wavelength of the incident light. Under blue light it reaches negative changes of  $V_{OC}$  for high ratios of  $P_{MPP}/P_{MPP,max}$ . Secondly, the slope of the trend lines is negative for blue light and then increases with increasing wavelength of incident light. For red and yellow light it is positive.

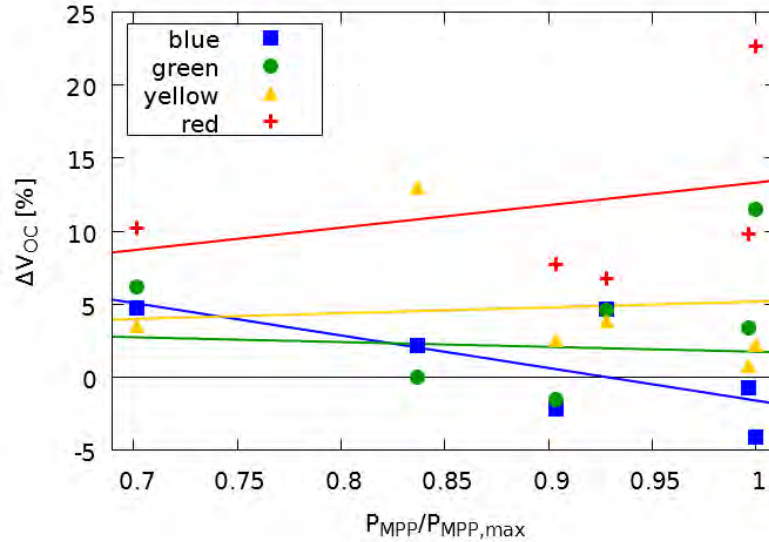


Figure 4.9: Power Rating:  $\Delta V_{OC}$  from  $P_{MPP}/P_{MPP,max}$  and linear trend lines.

Such shifting of metastable effects depending on cell quality has already been investigated for changes in buffer layer thickness [49], annealed and not-annealed a-Si PV modules [50] and cadmium telluride solar cells of different degradation [51].

# 5 Conclusion and Outlook

## 5.1 Conclusion

The goal of this thesis was to track the metastable behavior of CIGS cells with different buffer layer materials under low light irradiance of different colors. This was realized in a two hours measurement procedure under  $100 \text{ W/m}^2$  irradiance of white, blue, green, yellow, red and infrared light for two buffer layer materials, namely CdS and ZnO. For both buffer layer materials, cells of high quality (high  $V_{OC}$ , FF and  $P_{MPP}$ ) and low quality (low  $V_{OC}$ , FF and  $P_{MPP}$ ) were measured. For the CdS buffer layer, one cell of medium quality and one with low quality but high  $I_{SC}$  were measured as well.

The low quality cells of both buffer layer materials show an increase of  $V_{OC}$  and  $P_{MPP}$  under all light colors. With increasing quality the  $V_{OC}$  and the  $P_{MPP}$  start to decrease under white light. The medium quality CdS buffer layer cell and the high quality ZnO buffer layer cell show a similar behavior of  $V_{OC}$ , FF and  $P_{MPP}$  under white light. Before the decrease, a short increase was examined. Under red light both these cells as well as the high quality CdS buffer layer cell show an increase of  $V_{OC}$ , FF and  $P_{MPP}$ .

The similarities of the metastable effects between the low quality cells as well as the high quality ZnO and medium quality CdS buffer layer cells indicate that the metastable effects are rather quality dependent than buffer layer material dependent. The cell quality is determined by crystal defects and band gap matching.

Except for the high  $I_{SC}$  cell, the CdS buffer layer cells show continuous transitions between the different incident light colors for each quality as well as continuous transitions between the different qualities for each incident light color. Such transitions are also indicated for the high  $I_{SC}$  CdS buffer layer cell as well as both ZnO buffer layer cells.

For the CdS buffer layer cells, a hypothesis based on metastable defects, the location of the p-n junction and the penetration depth of colored light was developed which can explain the different metastable behavior under different light colors for different cell qualities.

## 5.2 Outlook

The light soaking experiments performed in this thesis have given insights into the behavior of metastable effects in CIGS cells. Some possible further experiments that might lead to a deeper understanding of the metastable processes will be outlined in the following.

In order to improve the accuracy of the measurements, colored filters without an infrared transmission should be used because as the experiments with infrared light

only showed, that infrared light has an effect on the cell's behavior. This effect could interfere with the effect caused by the colors alone. Also the bandwidths of the filters could be narrower in order to further isolate the wavelength dependent effects.

The hypothesis postulated in section 4.3.3 should be verified by measuring further CdS buffer layer cells. Further experiments on CdS buffer layer cells with high  $I_{SC}$  but low  $P_{MPP}$  like CdS\_28 could lead to an understanding of its different light soaking behavior.

By measuring good quality ZnO buffer layer cells the hypothesis could be tested on different buffer layers.

Another interesting series of experiments would be to perform light soaking experiments with different incident irradiation. As indicated by the STC light soaking measurement of the ZnO\_5 cell, the metastable effects don't linearly scale with the irradiance but show completely different effects. Whether there is a continuous transition or a sudden change at a threshold irradiance could give insights on the physical mechanisms inside the cell.

As can be seen in the green, yellow and red light measurement of the CdS\_32 cell, the  $V_{OC}$  initially increases and then decreases again. By prolonging the duration of the light soaking experiment it could be determined whether the  $V_{OC}$  stabilizes at a certain value or continuously decreases after the initial increase like under blue light.

In order to understand the interaction of the metastabilities caused by light of different colors, light soaking experiments with different colors could be performed in direct succession without letting the cell relax in the dark. In this manner the effect of certain present metastable states on others could be investigated. To do so it would also be important to know the relaxation process of certain metastable states which could be determined by dark soaking measurements. They could be performed with a flasher device that would measure the IV-curve of a cell stored in the dark with as little radiant energy as possible, thus minimizing the light soaking effect of the measurement.

Further experiments could help to localize the metastable centers and the defect structure. Methods suitable would be admittance measurements for measuring the charge carrier densities, HRXRD for revealing the crystalline quality of the layers, SEM-EDX or XPS measurements for analyzing the electron levels and chemical composition of the layers and interfaces.

# Bibliography

- [1] Michael Gostein and Lawrence Dunn. Light Soaking Effects on PV Modules: Overview and Literature Review. Technical report, NREL PV Module Reliability Workshop, 2011.
- [2] S. Novalin et al. Electrical metastabilities in chalcogenide photovoltaic devices. *Thin Solid Films*, 1(535):261–264, 2013.
- [3] S. Novalin, M. Rennhofer, J. Summhammer, R. Leidl, and S. Zamini. Metastabilities in thin-film modules due to pre-treatment. *26th European Photovoltaic Solar Energy Conference and Exhibition*, pages 3473 – 3475, 2011.
- [4] Michael Gostein and Lawrence Dunn. Light soaking effects on photovoltaic modules: Overview and literature review. *IEEE*, pages 003126–003131, 2011.
- [5] S. Lany and A. Zunger. Light- and bias-induced metastabilities in Cu(In,Ga)Se<sub>2</sub> based solar cells caused by the (V(Se)-V(Cu)) vacancy complex. *Journal of Applied Physics*, 100(11):113725, 2006.
- [6] Photovoltaics Wikipedia, The Free Encyclopedia. <https://en.wikipedia.org/wiki/Photovoltaics>, 2015. [Online; accessed 11-august-2015].
- [7] NREL National Center for Photovoltaics. <http://www.nrel.gov/ncpv/>, 2015. [Online; accessed 14-May-2015].
- [8] European Climate Foundation. Roadmap 2050. <http://www.roadmap2050.eu/project/roadmap-2050>. [Online; accessed 4-September-2015].
- [9] Wikipedia. Electricity generation — Wikipedia, the free encyclopedia. [http://en.wikipedia.org/wiki/Electricity\\_generation](http://en.wikipedia.org/wiki/Electricity_generation). [Online; accessed 14-June-2015].
- [10] Energy level Wikipedia, The Free Encyclopedia. [https://en.wikipedia.org/wiki/Energy\\_level](https://en.wikipedia.org/wiki/Energy_level), 2015. [Online; accessed 20-July-2015].
- [11] Demtröder Wolfgang. *Experimentalphysik 3 - Atome, Moleküle und Festkörper*. Springer-Verlag Berlin Heidelberg, 4th edition, 2010.
- [12] Semiconductor Detector Wikipedia, The Free Encyclopedia. [https://en.wikipedia.org/wiki/Semiconductor\\_detector](https://en.wikipedia.org/wiki/Semiconductor_detector), 2015. [Online; accessed 29-July-2015].
- [13] Mertens Konrad. *Photovoltaik: Lehrbuch zu Grundlagen, Technologie und Praxis*. Carl Hanser Verlag München, 1st edition, 2011.

- 
- [14] Direct and indirect band gaps Wikipedia, The Free Encyclopedia. [https://en.wikipedia.org/wiki/Direct\\_and\\_indirect\\_band\\_gaps](https://en.wikipedia.org/wiki/Direct_and_indirect_band_gaps), 2015. [Online; accessed 20-July-2015].
- [15] Volker Quaschnig. *Regenerative Energiesysteme*. Hanser Verlag München, 7th edition, 2011.
- [16] Nelson Jenny. *The Physics of Solar Cells*. Imperial College Press, 1st edition, 2010.
- [17] Roland Scheer and Hans-Werner Schock. *Chalcogenide Photovoltaics*. Weinheim : Wiley-VCH Verlag, 2011.
- [18] Wikipedia. Solar cell — Wikipedia, the free encyclopedia. [https://en.wikipedia.org/wiki/Solar\\_cell#History](https://en.wikipedia.org/wiki/Solar_cell#History). [Online; accessed 14-June-2015].
- [19] Conibeer Gavin J. and Willoughby Arthur. *Solar Cell Materials: Developing Technologies*. John Wiley & Sons, Ltd, 1st edition, 2014.
- [20] pvxchange. Preisindex pv module. <http://www.pvxchange.com/priceindex/Default.aspx?langTag=de-DE>. [Online; accessed 15-June-2015].
- [21] pro physik. Cigs erreicht erstmals Wirkungsgrad von multikristallinen Modulen. [http://www.pro-physik.de/details/news/2568801/CIGS\\_erreicht\\_erstmals\\_Wirkungsgrad\\_von\\_multikristallinen\\_Modulen.html](http://www.pro-physik.de/details/news/2568801/CIGS_erreicht_erstmals_Wirkungsgrad_von_multikristallinen_Modulen.html). [Online; accessed 15-June-2015].
- [22] PVEducation. Silicon solar cell parameters — pveducation. <http://www.pveducation.org/pvcdrom/design/solar-cell-parameters>. [Online; accessed 12-June-2015].
- [23] National Renewable Energy Laboratory. Miasolé achieves 15.7film solar modules. [http://www.miasole.com/sites/default/files/MiaSole\\_release\\_Dec\\_02\\_2010.pdf](http://www.miasole.com/sites/default/files/MiaSole_release_Dec_02_2010.pdf), 2010. [Online; accessed 27-August-2015].
- [24] Zweibel K. *The Terawatt Challenge for Thin Film Solar Cells, in Thin Film Solar Cells (ed. J. Poortmans)*. John Wiley & Sons, Ltd., 1st edition, 2007.
- [25] Jonathan J. Scragg. *Copper Zinc Tin Sulfide Thin Films for Photovoltaics*. Springer-Verlag Berlin Heidelberg, 1st edition, 2011.
- [26] Christoph Brabec, Vladimir Dyakonov, and Ullrich Scherf. *Organic Photovoltaics*. WILEY-VCH Verlag GmbH & Co.KGaA, 1st edition, 2009.
- [27] PV education. Solar cell operation - ideality factor. <http://www.pveducation.org/pvcdrom/characterisation/electroluminescence>, 2015. [Online; accessed 21-June-2015].
- [28] Wikipedia. Thermography — Wikipedia, the free encyclopedia. <https://en.wikipedia.org/wiki/Thermography>, 2015. [Online; accessed 21-June-2015].

- 
- [29] Sugimoto H. et al. Impact of Cu(InGa)(SeS)<sub>2</sub> absorber quality and circuit uniformity on improved efficiency; application of photoluminescence and electroluminescence. *Proceedings of the 24th European Photovoltaic Solar Energy Conference*, page 2465, 2009.
- [30] Mitchell K. et al. High efficiency thin film tandem PV modules. *Proceedings of the 19th IEEE Photovoltaic Specialist Conference*, page 13, 1987.
- [31] Kushiya K. et al. Interface control to enhance the fill factor over 0.70 in a large-area CIS-based thin-film PV technology. *Thin Solid Films*, 517:2108–2110, 2009.
- [32] Hariskos D., Spiering S., and Powalla M. Buffer layers in Cu(In,Ga)Se<sub>2</sub> solar cells and modules. *Thin Solid Films*, 480-481:99–109, 2005.
- [33] Virtuani A., Pavanello D., and Friesen G. Overview of temperature coefficients of different thin film photovoltaic technologies. *25th European Photovoltaic Solar Energy Conference and Exhibition*, pages 4248–4252, 2010.
- [34] Four terminal sensing Wikipedia, The Free Encyclopedia. [https://en.wikipedia.org/wiki/Four-terminal\\_sensing](https://en.wikipedia.org/wiki/Four-terminal_sensing), 2015. [Online; accessed 23-July-2015].
- [35] PVEducation. Quantum efficiency — pveducation. <http://www.pveducation.org/pvcdrom/solar-cell-operation/quantum-efficiency>. [Online; accessed 02-June-2015].
- [36] Wikipedia. Monochromator — Wikipedia, the free encyclopedia. <http://en.wikipedia.org/wiki/Monochromator>. [Online; accessed 02-June-2015].
- [37] original by DrBob FeuRenard Own work. Czerny-turner monochromator. [https://en.wikipedia.org/wiki/Monochromator#/media/File:Czerny-Turner\\_Monochromator.svg](https://en.wikipedia.org/wiki/Monochromator#/media/File:Czerny-Turner_Monochromator.svg), 2015. [Czerny-Turner Monochromator by FeuRenard - Own work, original by DrBob].
- [38] Ruberto Mark N. and Rothwarf Allen. Time-dependent Open-Circuit Voltage in CuInSe<sub>2</sub>/CdS solar cells: Theory and experiment. *Journal of Applied Physics*, 61:4662–4669, 1987.
- [39] R. A. Sasala and J. R. Sites. Time dependent voltage in cuinse<sub>2</sub> and cdte solar cells. *IEEE*, pages 543–548, 1993.
- [40] Robert P. Kenny, Miglena Nikolaeva-Dimitrova, and Ewan D. Dunlop. Performance measurements of cis modules: Outdoor and pulsed simulator comparison for power and energy rating. *IEEE*, pages 2058–2061, 2006.
- [41] A.Abelennda et al. Anomalous persistent photoconductivity in Cu<sub>2</sub>ZnSnS<sub>4</sub> thin films and solar cells. *Elsevier Solar Energy Materials and Solar Cells*, 137:164–168, 2015.

- 
- [42] Th. Meyer, F. Engelhardt, J. Parisi, and U. Rau. Spectral Dependence and Hall Effect of Persistent Photoconductivity in Polycrystalline Cu(In,Ga)Se<sub>2</sub> Thin Films. *Journal of Applied Physics*, 91, 2002.
- [43] Th. Meyer, F. Engelhardt, J. Parisi, and U. Rau. A Model for the Open Circuit Voltage Relaxation in Cu(In,Ga)Se<sub>2</sub> Heterojunction Solar Cells. *Eur. Phys. J. Appl. Phys.*, 8(1):43 – 52, 1999.
- [44] I.L Eisgruber and others. Blue-Photon Modification of Nonstandard Diode Barrier in CuInSe<sub>2</sub> Solar Cells. *Elsevier Solar Energy Materials and Solar Cells*, 53:367 – 377, 1998.
- [45] P. Zabierowski, U. Rau, and M. Igalson. Classification of Metastabilities in the Electrical Characteristics of ZnO/CdS/Cu(In,Ga)Se<sub>2</sub> Solar Cells. *Elsevier Thin Solid Films*, 387:147 – 150, 2001.
- [46] Ezenewa I.A. Synthesis and optical characterization of zinc oxide thin film. *Research Journal of Chemical Sciences*, 2(3):26 – 30, 2012.
- [47] Selma M. H. Al-Jawad, Ali M. Mousa, and Wessal Aead Taha. Investigation of Optical Properties of Cadmium Sulfide (CdS) Thin Films by Chemical Bath Deposition. *Um-Salama Science Journal*, 6(1):150 – 162, 2009.
- [48] Autoignition temperature Wikipedia, The Free Encyclopedia. [https://en.wikipedia.org/wiki/Autoignition\\_temperature](https://en.wikipedia.org/wiki/Autoignition_temperature), 2015. [Online; accessed 23-July-2015].
- [49] Sabrina Novalin, Marcus Rennhofer, and Johann Summhammer. Modelling the pre-treatment of chalcogenide solar cells. to be published.
- [50] Ankit Mittal, Marcus Rennhofer, Angelika Dangel, Bogdan Duman, and Victor Schlosser. Power change in amorphous silicon technology by low temperature annealing. *EPJ Photovoltaics*, 6(65304), 2015.
- [51] Ankit Mittal, Marcus Rennhofer, et al. Degradation Mechanism in Cadmium Telluride Modules With Correlation to its Metastabilities. in press.

# List of Figures

1.1	Development of world primary energy consumption . . . . .	9
1.2	Earth's energy reserves . . . . .	9
1.3	Solar cell working principle . . . . .	12
1.4	Homojunction and heterojunction . . . . .	12
1.5	Best Cell Efficiencies . . . . .	13
1.6	Global market share of Photovoltaics . . . . .	17
1.7	Electroluminescence and Photoluminescence . . . . .	18
1.8	Thermography of PV-devices . . . . .	19
1.9	IV- and power-curve . . . . .	20
1.10	CIGS cell architecture . . . . .	21
2.1	Light beam absorption . . . . .	27
2.2	IV-curve of a CIGS cell under standard testing conditions . . . . .	29
2.3	Principle of the four-point measuring method . . . . .	30
2.4	The quantum efficiency of a solar cell . . . . .	34
2.5	QE Comparison . . . . .	34
2.6	Scheme of a Czerny-Turner Monochromator . . . . .	36
2.7	Example of light soaking curves . . . . .	37
2.8	Initial anomalies of IV-curves of CIGS solar cells . . . . .	38
2.9	Solar Spectrum AM1.5 . . . . .	42
2.10	Colors and wavelengths of the visible light. . . . .	42
2.11	Transmittance of a green filter in the visible light range. . . . .	43
3.1	Sun simulator lamp . . . . .	45
3.2	Setup of the IV-curve measurement . . . . .	45
3.3	$I_{SC}$ from the reference cell during one IV-curve measurement . . . . .	47
3.4	IV-curve current correction . . . . .	48
3.5	Temperature development in the sun simulator . . . . .	49
3.6	Structure of the measured CIGS cells . . . . .	50
3.7	Light Soaking measurement under STC. . . . .	50
3.8	An example of the measured IV-curves. . . . .	51
3.9	Setup of the EQE measurement . . . . .	52
3.10	EQE contacting . . . . .	53
3.11	Repetition of the EQE measurement . . . . .	54
3.12	QE example and the GUI of the used spectral correction program . . . . .	54
3.13	EQE-measurement curves of the CIGS solar cells with CdS buffer layer . . . . .	56
3.14	EQE-measurement curves of the CIGS solar cells with ZnO buffer layer . . . . .	56
3.15	Light soaking with linear and logarithmic time scale. . . . .	58
3.16	Temperature development under $1000 \text{ W/m}^2$ illumination . . . . .	60
3.17	Spectral Irradiance of the colored illumination configurations . . . . .	61



3.18 Transmittance of the color filters . . . . .	63
3.19 Uniformity of the measuring plane with installed filters . . . . .	64
3.20 Coordinate system on the drawer to measure the uniformity. . . . .	65
3.21 Development of temperature during a light soaking experiment . . . . .	67
3.22 Correction of light soaking curves . . . . .	69
3.23 IV-curves of a measurement with bad electric contact . . . . .	70
3.24 Discrete values of $V_{OC}$ . . . . .	71
4.1 IV-measurement curves of the CIGS solar cells with CdS buffer layer . .	73
4.2 IV-curves of the CIGS solar cells with ZnO buffer layer . . . . .	73
4.3 Results of the Light Soaking experiments of CdS buffer layer cells . . .	77
4.4 Results of the Light Soaking experiments of CdS buffer layer cells . . .	79
4.5 Results of the Light Soaking experiments of ZnO buffer layer cells . . .	82
4.6 Change of the IV-curve of the CdS_32 cell under red light illumination .	83
4.7 Scheme of hypothesis explaining light soaking effects . . . . .	86
4.8 IV-curve of the ZnO_17 cell under blue light . . . . .	87
4.9 Power Rating: $\Delta V_{OC}$ from $P_{MPP}/P_{MPP,max}$ . . . . .	89

# List of Tables

1.1	Table of material's/technologies' efficiencies . . . . .	13
1.2	III-V-compound efficiencies . . . . .	15
1.3	Defect transition energy for CuInSe <sub>2</sub> . . . . .	20
2.1	Table of technologies' temperature coefficients . . . . .	29
2.2	IEC 60904 solar spectrum intervals . . . . .	31
2.3	Definition of solar simulator classifications according to IEC norm 60904. . . . .	32
2.4	Qualitative change in $V_{OC}$ depending on $n_p$ and $p_n$ . . . . .	40
2.5	Some wavelengths of light and the corresponding energy. . . . .	41
3.1	Diffuse light measurements of sun simulator irradiation . . . . .	46
3.2	Differences in QE measurements after recontacting the cell . . . . .	53
3.3	$I_{SC}$ comparison . . . . .	55
3.4	Time intervals of the light soaking experiments . . . . .	59
3.5	Irradiance measurement for the filter setup . . . . .	59
3.6	Measured irradiance of low irradiance configurations . . . . .	61
3.7	Bandwidths of the color filters . . . . .	62
4.1	IV-curve measurement results . . . . .	72
4.2	Development and value of final change of the $V_{OC}$ . . . . .	74
4.3	Development and value of final change of the FF . . . . .	75
4.4	Development and value of final change of the $P_{MPP}$ . . . . .	75